UNIVERSIDAD
NACIONAL
DE COLOMBIA

Determination of the relationship between magnetocaloric effect and electrical properties in polycrystalline samples of $La_{0.7}Ca_{0.3}Mn_{1-x}Ni_xO_3$ (x = 0, 0.02, 0.07, 0.1)

Adrián Augusto Gómez Zapata

Universidad Nacional de Colombia

Facultad de Minas, Departamento de Materiales y Minerales

Medellín, Colombia

2019

Determination of the relationship between magnetocaloric effect and electrical properties in polycrystalline samples of $La_{0.7}Ca_{0.3}Mn_{1-x}Ni_xO_3$ (x = 0, 0.02, 0.07, 0.1)

Adrián Augusto Gómez Zapata

Tesis de investigación presentada como requisito parcial para optar al título de:

Doctor en Ingeniería – Ciencia y Tecnología de Materiales

Director:

Dr. rer. nat. Jesús Oswaldo Morán Campaña

Co-director:

Dr. Ing. Néstor Ricardo Rojas Reyes

Líneas de Investigación:

Materiales magnetocalóricos, energías alternativas, nuevos materiales nanoestructurados

Grupo de Investigación:

Óxidos Avanzados – Materiales Cerámicos y Vítreos

Universidad Nacional de Colombia

Facultad de Minas, Departamento de Materiales y Minerales

Medellín, Colombia

2019

A Diana Sucerquia Jaramillo por su paciencia, comprensión, amor, apoyo incondicional y sacrificio.

A Milvia Jaramillo Gómez, por sus ánimos, confianza en mí y apoyo durante la realización de este estudio.

Acknowledgments

Dr. Jesús Oswaldo Morán Campaña, Profesor Titular Facultad de Ciencias, Universidad Nacional de Colombia, Sede Medellín, Director de la tesis de investigación por haber confiado en mí, por sus conocimientos y aportes durante todo este tiempo.

Dr. Néstor Ricardo Rojas Reyes, Profesor Asociado Facultad de Minas, Universidad Nacional de Colombia, Sede Medellín, Co-Director de la tesis de investigación por sus consejos, amistad y todo el apoyo durante todo el estudio.

Dra. Claudia Patricia García García, Profesora Titular Facultad de Ciencias, Universidad Nacional de Colombia, Sede Medellín, Directora Grupo de Investigación y del Laboratorio de Materiales Cerámicos y Vítreos por la colaboración con la síntesis de todos los materiales analizados en la tesis.

Dr. Jorge Luis Izquierdo Núñez, Profesor Asistente, Facultad de Ingeniería, Institución Universitaria Pascual Bravo, por el apoyo, amistad y por haber facilitado el uso de la infraestructura de dicha institución.

Dr. Edgar Andrés Chavarriaga Miranda, Profesor Investigador, por su apoyo, amistad y por hacerme propuesto y explicado el proceso de síntesis por auto-combustión para las manganitas como método alternativo y económico para su fabricación.

Dr. Carlos Arturo Parra Vargas, Profesor Asistente, Ms. Iván Supelano García, Investigador, Facultad de Ciencias, Universidad Pedagógica y Tecnológica de Colombia, por su apoyo con la caracterización magnética de los materiales utilizados en la tesis por medio de la técnica de Magnetometría de Muestra Vibrante (VSM).

Dr. Alejandro Conde Amiano, Profesor Emérito; Dr. Javier Sebastián Blázquez Gámez, Profesor Catedrático de Universidad; Dr. Victorino Franco García, Catedrático de Universidad; Dr. Jhon Jairo Ipus Bados, Profesor Ayudante Doctor; del Departamento de Física de la Materia Condensada, Universidad de Sevilla por su acogida en el grupo de investigación y por haberme facilitado la realización de la pasantía para el logro de los objetivos de la tesis.

Dr. Federico Mompeán García, Científico Titular, Dr. Jesús Prado Gonjal, Científico Contratado, Instituto de Ciencia de Materiales de Madrid, por su colaboración, amabilidad y prontitud para la realización de las pruebas de magnetoresistencia.

Dr. Francisco Manuel Varela Feria, Técnico Superior Apoyo Docencia e Investigación Microscopía Electrónica, Centro de Investigación, Tecnología e Innovación, Universidad de Sevilla (CITIUS), por su apoyo para la adquisición de imágenes TEM.

Dr. Carlos Salazar, Gerente empresa CECOLTEC S. A. S. por su amabilidad, disposición y apoyo con la adquisición de imágenes SEM.

Srta. Gloria Elena Ruíz Giraldo y Srta. Martha Cecilia Salazar Gómez, por su amistad, insistencia y gran apoyo para la culminación de este estudio.

Sra. Luz Mery Arrubla Montoya, por su amistad y disponibilidad para la colaboración con muchos aspectos experimentales de este proyecto.

A Claudia Rojas y familia, por su amable recibimiento y acogida durante el tiempo que estuve en la ciudad de Tunja.

A todas aquellas personas que directa o indirectamente; y que se me escapa mencionar aquí; estuvieron presentes y pendientes durante este proceso de formación.

PUBLICATIONS and CONFERENCES

O. Morán, A. Gómez, I. Supelano, C.A. Parra, J.L. Izquierdo. Assessment of the critical behavior near the FM to PM phase transition in nano-crystalline $La_{0.7}Ca_{0.3}Mn_{1-x}Ni_xO_3$ (x=0, 0.02, 0.07, 0.1) samples synthesized by auto-combustion. *Journal of Magnetism and Magnetic Materials 477 (2019) 22–26.*

A. Gómez, J.L. Izquierdo, O. Morán, I. Supelano, C.A. Parra, E. Chavarriaga. Ferromagnetic long-range ordering in nano-crystalline $La_{0.7}Ca_{0.3}Mn_{1-x}Ni_xO_3$ (x=0, 0.02) manganites. *Journal of Magnetism and Magnetic Materials 475 (2019) 524–532.*

A. Gómez, E. Chavarriaga, J.L. Izquierdo, J. Prado-Gonjal, F. Mompean, N. Rojas, O. Morán. Assessment of the relationship between magnetotransport and magnetocaloric properties in nano-sized $La_{0.7}Ca_{0.3}Mn_{1-x}Ni_xO_3$ manganites. *Journal of Magnetism and Magnetic Materials 469 (2019) 558–569.*

Adrián Gómez, Edgar Chavarriaga, Iván Supelano, Carlos Arturo Parra, and Oswaldo Morán. Evaluation of the magnetocaloric response of nano-sized $La_{0.7}Ca_{0.3}Mn_{1-x}Ni_xO_3$ manganites synthesized by auto-combustion method. *AIP Advances 8, 056430 (2018).*

A. Gómez, E. Chavarriaga, I. Supelano, C.A. Parra, O. Morán. Tuning the magnetocaloric properties of $La_{0.7}Ca_{0.3}Mn_{1-x}Ni_xO_3$ manganites through Ni-doping. *Physics Letters A 382 (2018) 911–919.*

A. Muñoz-Mizuno, A. Gómez-Zapata, O. Morán, N. Rojas-Reyes, H.A. Estupiñan. Efecto del níquel en la respuesta electroquímica de materiales magnetocalóricos sintetizados por reacción en estado sólido y autocombustión. Póster en *X Congreso Internacional de Materiales (CIM)*. Bucaramanga, Colombia, October 2019.

A. Muñoz-Mizuno, A. Gómez-Zapata, O. Morán, N. Rojas-Reyes, J.S. Blázquez, J.J. Ipus, J.L. Izquierdo, H.A. Estupiñan. Electrochemical impedance measurements on $La_{0.7}Ca_{0.3}Mn_{1-x}Ni_xO_3$ (x=0, 0.07) manganites synthesized by mechanical alloying and auto-combustion routes. Poster in *XXVIII International Materials Research Congress (IMRC)*. Cancun, Mexico, August 2019.

Morán-Oswaldo, Gómez-Adrián, Chavarriaga-Edgar, Supelano-Iván, Parra-Carlos, Izquierdo-Jorge. Assessment of the critical behavior near the FM to PM phase transition in nano-crystalline $La_{0.7}Ca_{0.3}Mn_{1-x}Ni_xO_3$ (x=0, 0.02, 0.07, 0.1) samples synthesized by auto-combustion. Poster in *9th Joint European Magnetic Symposia (JEMS) Conference 2018.* Mainz, Germany, September 2018.

A. Gómez, O. Morán, J.S. Blázquez, A. Conde, J.J. Ipus, V. Franco, N. Rojas, J.L. Izquierdo. Evolution of the magnetocaloric effect in polycrystalline $La_{0.7}Ca_{0.3}Mn_{1-x}Ni_xO_3$ (x=0, 0.02, 0.07, 0.1) samples synthesized by ball milling process. Poster in *25th International Symposium on Metastable, Amorphous and Nanostructured Materials (ISMANAM)*. Rome, Italy, July 2018.

A. Gómez, O. Morán, E. Chavarriaga, N.R. Rojas, J.S. Blázquez, A. Conde, J.L. Izquierdo, C. Parra, I. Supelano. Magnetocaloric effect and demagnetizing factor in $La_{0.7}Ca_{0.3}Mn_{1-x}Ni_xO_3$ (x=0, 0.02, 0.07, 0.1). Poster in *23rd Soft Magnetic Materials Conference*. Seville, Spain, September 2017.

Resumen

Se reporta el efecto de la substitución del Ni^{2+} sobre las propiedades de magneto-transporte y su relación con la función magnetocalórica en muestras policristalinas de tamaño nanométrico de la manganita tipo perovskita $La_{0.3}Ca_{0.7}Mn_{1-x}Ni_xO_3$ (x = 0, 0.02, 0.07, 0.1) sintetizadas por medio de los procesos de auto-combustión y reacción en estado sólido estándar. El objetivo de estudiar estas manganitas fue explorar la posibilidad de aumentar el rango de la temperatura de operación para el efecto magnetocalórico a través del ajuste de la temperatura de la transición magnética. Los estudios y análisis de difracción de rayos-X confirmaron la pureza de la fase de las muestras obtenidas. También se verificó por medio de esta técnica la substitución de iones Mn^{3+} por iones Ni^{2+} en la red del compuesto $La_{0.3}Ca_{0.7}MnO_3$. Los análisis por medio del método de Rietveld indicaron que el volumen de la celda unitaria aumenta a medida que el contenido de Ni^{2+} también aumenta. Las curvas de magnetización en enfriamiento a cero campo y con campo, revelaron que todas las muestras presentan una transición de fase paramagnética a ferromagnética, la cual es simultánea con una transición metal-aislante. Se observó una pequeña desviación entre las curvas de magnetización en enfriamiento cuando éstas van desde cero hasta un campo de 1000 Oe. La temperatura de Curie disminuye sistemáticamente desde 264 (268) K para x = 0 hasta 174 (185) K para x = 0.1 en las muestras sintetizadas por medio de los procesos de combustión en solución y reacción en estado sólido; entre paréntesis, respectivamente. Probablemente, el dopaje en el sitio del Mn^{3+} con iones de Ni^{2+} en la red del compuesto $La_{0.3}Ca_{0.7}MnO_3$ debilita la interacción de doble intercambio Mn^{3+}–O–Mn^{4+}, lo cual conlleva a una disminución en la temperatura de transición. De manera interesante, un notable aumento en el valor del cambio de entropía magnética se observa a partir de niveles de dopaje con Ni^{2+} tan bajos como el 2 %. El máximo cambio de entropía magnética observado en los compuestos x = 0, 0.02, 0.07 y 0.1 a un campo magnético de 1.5 T fue de 0.86 (1.73), 0.77 (1.55), 0.63 (1.14) y 0.60 (1.15) J/kgK en las muestras sintetizadas por medio de los procesos de combustión en solución y reacción en estado sólido; entre paréntesis, respectivamente. Se observó un aumento sistemático en el valor de la capacidad relativa

de refrigeración (RCP, por sus siglas en inglés) a medida que se aumenta el campo magnético desde 0 hasta 1.5 T. El valor más alto para este parámetro fue de ~ 60 (~48) J/kg para un nivel de dopaje de 2 (7) % alrededor de 225 (202) K en las muestras sintetizadas por medio de los procesos de combustión en solución y reacción en estado sólido; entre paréntesis, respectivamente. Las gráficas de Arrot revelaron una transición de fase magnética de segundo orden para todas las muestras, lo cual fue confirmado por la teoría de Landau y las curvas universales. El carácter de segundo orden de la transición de fase magnética observado en la muestra $La_{0.3}Ca_{0.7}MnO_3$ pura puede ser atribuido a los efectos de disminución del tamaño de partícula. Se encontró que el mejor modelo para establecer el valor de los exponentes críticos relacionados con el comportamiento de las manganitas de $La_{0.3}Ca_{0.7}MnO_3$ fue el modelo de la Teoría del Campo Medio (MFT, por sus siglas en inglés). El valor del exponente crítico β fue de 0.465 (0.495), 0.448 (0.472), 0.511 (0.508) y 0.509 (0.545) y el de γ fue de 1.157 (1.037), 1.226 (1.130), 0.972 (0.984) y 0.978 (0.835) para x = 0, 0.02, 0.07 y 0.1 en las muestras sintetizadas por combustión en solución y reacción en estado sólido; entre paréntesis, respectivamente. La transición metal-aislante también se desplaza hacia bajas temperaturas luego de la substitución con el Ni^{2+} mientras el valor de la resistividad aumenta. Se encontraron diferentes mecanismos de conducción en diferentes regiones de temperatura. Se obtuvieron importantes parámetros físicos tales como la energía de activación de los polarones a partir del ajuste de los modelos a los datos experimentales. El gran cambio en la magnetoresistencia cercano a la temperatura de transición magnética sugiere una estrecha relación entre el efecto magnetocalórico y las propiedades de magneto-transporte en las manganitas de $La_{0.3}Ca_{0.7}MnO_3$. Este comportamiento puede ser atribuido a la característica de orden/desorden del espín que juega un papel crucial en ambos efectos. Por otro lado, el valor de la magnetoresistencia de la muestra $La_{0.3}Ca_{0.7}MnO_3$ pura se aumenta a medida que se aumenta el nivel de dopaje con Ni^{2+}, lo cual probablemente, también puede estar relacionado con la disminución del tamaño de partícula.

Palabras clave: Efecto magnetocalórico, propiedades de magneto-transporte, manganitas, mecanismos de conducción**.**

Abstract

The effect of Ni^{2+} substitution on the magneto-transport properties and the concomitant relationship with the magnetocaloric function of nano-sized $La_{0.3}Ca_{0.7}Mn_{1-x}Ni_xO_3$ (x = 0, 0.02, 0.07, 0.1) perovskite manganite polycrystalline samples are reported. All the samples were synthesized using auto-combustion and standard solid state reaction methods. The aim of studying Ni^{2+}-substituted $La_{0.3}Ca_{0.7}Mn_{1-x}Ni_xO_3$ (x = 0, 0.02, 0.07, 0.1) manganites was to explore the possibility of increasing the operation temperature range for the magnetocaloric effect through tuning of the magnetic transition temperature. X-ray diffraction analysis studies confirm the phase purity of the synthesized samples. The substitution of Mn^{3+} ions by Ni^{2+} ions in the $La_{0.3}Ca_{0.7}MnO_3$ lattice is also verified by this technique. Rietveld analysis indicates that the volume of the unit cell increases with increasing Ni^{2+} content. Zero-field cooled and field-cooled magnetization shows that all samples undergo a paramagnetic-ferromagnetic-phase transition, which is concomitant with a metal-insulator transition. A small deviation between the zero-field cooled magnetization curves is observed when the measurements are carried out in a field of 1000 Oe. The Curie temperature decrease systematically from 264 (268) K for x = 0 to 174 (185) K for x = 0.1 in samples synthesized by means of combustion solution and solid state reaction process; in brackets, respectively. Probably, the doping at the Mn^{3+}-site with Ni^{2+} ions in the $La_{0.3}Ca_{0.7}MnO_3$ lattice weakens the Mn^{3+}–O–Mn^{4+} double exchange interaction, which leads to a decrease in the transition temperature. Interestingly, a notable increase in the value of the magnetic entropy change is observed at Ni^{2+}-doping levels as low as 2 %. The analysis of the magnetization results show that the maximum entropy changes observed for x = 0, 0.02, 0.07 and 0.1 compositions are 0.86 (1.73), 0.77 (1.55), 0.63 (1.14) and 0.60 (1.15) J/kgK in samples synthesized by means of combustion solution and solid state reaction process; in brackets, respectively. A systematical increase of the Relative Cooling Power (RCP) value was observed with an increasing magnetic field from 0 to 1.5 T. The highest value for this parameter was ~ 60

(~48) J/kg for a doping level of 2 (7) % around 225 (202) K in samples synthesized by means of combustion solution and solid state reaction process; in brackets, respectively. Arrot´s plots reveal a second order nature of magnetic transition for all the samples, which is also confirmed by Landau´s theory and universal curves. The second-order character of the magnetic phase transition observed in the pristine $La_{0.3}Ca_{0.7}MnO_3$ sample may be attributed to effects of downsizing of the particle. It is found that the superior model for stablishing the critical exponent values was the Mean Field Theory (MFT). The value for the β critical exponent was 0.465 (0.495), 0.448 (0.472), 0.511 (0.508) and 0.509 (0.545) and for the γ critical exponent was 1.157 (1.037), 1.226 (1.130), 0.972 (0.984) y 0.978 (0.835) for x = 0, 0.02, 0.07 and 0.1 in samples synthesized by means of combustion solution and solid state reaction process; in brackets, respectively. The metal-insulator transition also shifts to lower temperatures upon Ni^{2+} substitution and the value of the resistivity increases. Different conduction mechanisms are found in different temperature regions. Important physical parameters such as the polaron activation energy are obtained from the fitting of the models to the experimental data. The magnetoresistance undergoes a great change near the magnetic transition temperature suggesting a close relationship between the magnetocaloric effect and magneto-transport properties in $La_{0.3}Ca_{0.7}MnO_3$ manganites. Such behavior can be attributed to the spin order/disorder feature that plays a crucial role in both effects. On the other hand, the value of the magnetoresistance of the pristine $La_{0.3}Ca_{0.7}MnO_3$ sample is increased upon Ni^{2+}-doping, which, probably, is related to the downsizing of the particle.

Keywords: Magnetocaloric effect, magneto-transport properties, manganites, conduction mechanisms.

Content

List of figures

Pág.

List of tables

Pág.

Introduction

Manganite materials with the composition $R_{1-x}A_xMnO_3$ (R= rare earth elements such as La, Nd, Pr, and Sm, and A = divalent alkaline elements such as Ca, Ba, and Sr) have received increasing attention due to their special properties, such as colossal Magnetoresistance (CMR), metal–insulator (MI) transition, and the magnetocaloric effect (MCE) [1,2]. In particular, magnetic refrigeration, based on MCE, is considered to be an alternative to the well-established compression-evaporation cycle for room-temperature applications [3]. Apart from the manganites, a variety of materials that exhibit a large MCE have been studied, and the relevant results have been summarized in several review articles [4–6]. To mention just a few examples, Gd is among the pure lanthanide elements exhibiting MCE, the only pure metal with T_C close to room temperature [4]. Interestingly, room temperature MCE has been studied for other Gd-M binary compounds such as $Gd_{0.85}Y_{0.15}$, $Gd_{0.85}Tb_{0.15}$ [7], and $Gd_{0.75}Zn_{0.25}$ [8] systems. Composites of $Gd_{1-x}Ho_x$ alloys (x= 0, 0.09, 0.20) have recently been considered for optimizing the MCE response within the temperature range 265–293 K, which is desirable for the Ericsson refrigeration cycle [9]. Other interesting MCE materials are the AB_2 intermetallic compounds known as Laves phases [10]. In the AB_2 stoichiometry, A represents a rare-earth metal (including Sc and Y) and B mainly a transition metal. The transition temperatures of most of the Laves phases, which are attractive for MCE, lie below 100 K. Laves phases with transition temperatures above 100 K generally contain Co as a transition metal [11].

Other MCE materials that have recently been investigated are $La(Fe_{1-x}Si_x)_{13}$ alloys and their hydrides $La(Fe_{1-x}Si_x)_{13}Hy$, $MnFeP_xAs_{1-x}$ alloys, and $Ni_{2-x}Mn_{1-x}Ga$ Heusler alloys [12–15]. Although synthesis of these systems requires very controlled conditions, the achieved results show that they are potentially interesting for practical applications in magnetic refrigeration. Nevertheless, several disadvantages, such as large thermal and/or field hysteresis and high production costs, hamper the use of these materials in actual magnetic refrigerant applications. In this regard, perovskite-type manganites not only

exhibit a large MCE but also high refrigeration efficiency, low-cost production, chemical stability, and a broad working temperature [16]. In addition, the manganites are environmentally friendly and nontoxic, and they do not cause atmospheric pollution. These characteristics make them attractive for further research in refrigeration technology not based on gas compression.

Generally speaking, the large magnetic entropy change (ΔS_M) observed in perovskite manganites is mainly linked to the variation of the double exchange (DE) interaction of the Mn^{3+} and Mn^{4+} ions [17]. It has also been suggested that the strong spin-lattice coupling in the magnetic ordering process could also play an important role in the large magnetic entropy change in perovskite manganites [18]. The considerable lattice changes that accompany the magnetic transition in perovskite manganites indicate that there is a strong coupling between spin and lattice in this kind of material [19]. Concretely, the lattice structural change in the Mn–O bond distance and in the ⟨Mn–O–Mn⟩ bond angle would favor spin ordering. As a consequence, a more abrupt variation of the magnetization near T_C will happen, leading to a large ΔS_M and therefore to a large MCE.

When the particle size is reduced to a few tens of nanometers, the properties of perovskite manganites are quite different from those at the microscale [20, 21]. For instance, low saturation magnetization and low-field magnetoresistance (MR) are some special effects observed in nanometric manganites [22–25]. Recent reports have shown that the reduction of the particle size plays an important role in the determination of the change in magnetic entropy [26].

In recent years, the issue of replacing the Mn site with non-magnetic and magnetic ions has received special attention [27, 28]. This is because Mn-site doping allows one to explore more information about the structural, magnetic, and transport properties of these complex materials. It has been argued that the study of doping effects at the Mn site by other elements with different electronic configurations and ionic radii, such as Fe, Co, Cr, and Ni, deserves particular emphasis because of the decisive role of Mn ions in the colossal magnetoresistance materials [29]. In particular, the substitution of Mn^{3+} with Ni^{2+} ions in the pristine LCMO lattice directly influences its magnetic and electrical properties [30]. Concretely, the replacement of Mn^{3+} with Ni^{2+} modifies the ratio of Mn^{3+}–O_2–Mn^{4+}

bonds, which leads to a weakening of the DE interaction. Consequently, the transition temperature T_C is reduced and the resistivity increased. Likewise, the competition between FM and AFM exchange interactions is reinforced [31]. Indeed, Ni^{2+} substitution for Mn^{3+} increases the number of Mn^{4+} [32]. This in turn leads to an increase in the AFM interaction pairs such as Mn^{4+}–Mn^{4+}, Ni^{2+}–Mn^{3+}, and Ni^{2+}–Ni^{2+} [33]. Thus the magnetic interactions in the Ni^{2+}-doped LCMO samples are different from those of the undoped ones.

The influence of Ni^{2+} doping at the Mn site on the structural, magnetic, and MCE properties of CMR manganites has been reported in several papers [33–35]. Nevertheless, the greatest part of the results reported in these references was achieved on samples synthesized by conventional solid-state reaction, which produces grain sizes in the micrometer range. As previously stated, particle size plays an obvious role in the determination of the change in magnetic entropy and the magnetotransport properties of manganites [26]. In this connection, it´s already known that there are other methods based on wet chemistry to produce perovskite-type materials in the nanometric order; these methods have potential advantages, such as better homogeneities, lower processing temperatures, short annealing times and without intermediate decomposition steps [36].

In the present investigation, the solid state reaction and auto-combustion methods were successfully used to produce high-quality, micrometric and nanometric polycrystalline samples of $La_{0.7}Ca_{0.3}Mn_{1-x}Ni_xO_3$ (x= 0, 0.02, 0.07, 0.1), in which the main aim was to determine the relationship between MCE and electrical properties in these materials. To reach this goal, a series of studies have been development, which results; only for auto-combustion process; were reported through different publications.

The results of the firs study were published in the paper, “Tuning the magnetocaloric properties of $La_{0.7}Ca_{0.3}MnO_3$ manganites through Ni-doping”, the aim of studying Ni^{2+}-substituted $La_{0.7}Ca_{0.3}Mn_{1-x}Ni_xO_3$ (x= 0, 0.02, 0.07, 0.1) manganites was to explore the possibility of increasing the operation temperature range for the magnetocaloric effect through tuning of the magnetic transition temperature. X-ray diffraction analysis confirmed the phase purity of the synthesized samples. The dependence of the magnetization on

the temperature reveals a systematic decrease in the values of the Curie temperature upon Ni^{2+} doping [AGZ].

Results of a second study were published in the paper, “Evaluation of the magnetocaloric response of nano-sized $La_{0.7}Ca_{0.3}Mn_{1-x}Ni_xO_3$ manganites synthesized by auto-combustion method”. A systematic study of the dependence of the magnetization on the magnetic field around the ferromagnetic–paramagnetic phase transition temperature is carried out on these samples. Banerjee´s criteria, Arrott plots, and the scaling hypothesis were used to analyze the experimental data. It is verified that the Ni-doping increases the operating temperature range for magnetocaloric effect through tuning of the magnetic transition temperature. The analysis of the magnetization results show that the maximum magnetic entropy changes observed for x = 0, 0.02, 0.07, and 0.1 compositions were 0.85, 0.77, 0.63, and 0.59 J/kg K, respectively, under a magnetic field of 1.5 T.

A third study was carried out and the results were published in the paper “Assessment of the relationship between magnetotransport and magnetocaloric properties in nano-sized $La_{0.7}Ca_{0.3}Mn_{1-x}Ni_xO_3$ manganites”, which reports the effect of Ni^{2+} substitution on the magneto-transport properties and the concomitant relationship with the magnetocaloric function of nano-sized $La_{0.7}Ca_{0.3}Mn_{1-x}Ni_xO_3$ (x = 0, 0.02, 0.07, and 0.10) perovskite manganites. Zero-field-cooled and field-cooled magnetization showed that all samples underwent a paramagnetic-ferromagnetic phase transition, which was concomitant with a metal-insulator transition. The metal-insulator transition also shifted to lower temperatures upon Ni^{2+} substitution, and the value of the resistivity increased. Different conduction mechanisms were found in different temperature regions. Important physical parameters such as the polaron activation energy were obtained from the fit of the models to the experimental data. The magnetoresistance underwent a great change near the magnetic transition temperature, suggesting a close relationship between the magnetocaloric effect and magnetotransport properties in $La_{0.7}Ca_{0.3}MnO_3$ manganites.

Finally, a fourth study was accomplished, which results were published in the paper “Assessment of the critical behavior near the FM to PM phase transition in nano-crystallyne $La_{0.7}Ca_{0.3}Mn_{1-x}Ni_xO_3$ (x = 0, 0.02, 0.07, and 0.10) samples synthesized by auto-combustion”. Various techniques such as modified Arrott plots, Kouvel-Fisher

method and critical isotherm were used to analyze the magnetic-field dependence of magnetization. Although the critical exponents beta (β), gamma (γ) and delta (δ) were analyzed with various theoretical models such as 3D-Ising model and 3D-Heisenberg model, the estimated critical exponents, obtained for different values of x, seemed to be consistent with those predicted by the mean-field theory. The critical exponents were further confirmed using the single scaling equation $M(H,\varepsilon)=\varepsilon^{\beta}f \pm (H/\varepsilon^{\gamma+\beta})$. The achieved results indicated that the obtained values of the critical exponents were reliable and reasonably accurate.

1. Background and framework

In the following item is presented only a brief description of some of the main topics related with the thesis such as perovskite structures and the Goldschmidt tolerance factor; then, the manganites and its phase diagrams, the Jahn–Teller Effect, Colossal Magnetoresistance and Magnetocaloric Effect in $La_{0.7}Ca_{0.3}MnO_3$ manganite samples; and finally, the thermodynamics and first principle models that describe the magnetocaloric effect in solid magnetocaloric material.

1.1 Perovskites

Perovskites can be described by the general formula ABO_3, *A* and *B* being two cations and *O* being an oxygen anion. These isomorphic solids are highly versatile due to the flexibility in the chemical composition of perovskites with a large number of cations that can fit into both the *A* and *B* positions within the same crystalline structure (i.e., practically all the metals are stable in the perovskite lattice). Another key feature is the availability of multi-components perovskite, which can be synthesized by partial substitution of cations at either *A* or *B* sites (Nitin Labhasetwar, et al., 2015).

In the perovskite structure, the A cation can be a lanthanide, alkaline, or alkaline-earth cation while the B cation is a metallic element from the *3d*, *4d*, or *5d* configuration. Considering the possible valences of the cations and the electroneutrality of the structure, different charge distributions can be encountered in the structure, i.e., $A^{I}B^{IV}O_3$, $A^{II}B^{IV}O_3$, or $A^{III}B^{III}O_3$. The ideal crystalline unit cell of perovskite is described as cubic from the *Pm3m* space group, where the *A* cation is in the center of the cube, formed by the *B* cations, and the oxygen ions are located in the middle of the edges. The *B* cation is in octahedral coordination toward oxygen, while the *A* cation is in dodecahedral coordination (Tejuca L. G., et al., 1993).

Figure. Ideal perovskite type structure ABO_3. Reference: Kun Zhang et al., 2011.

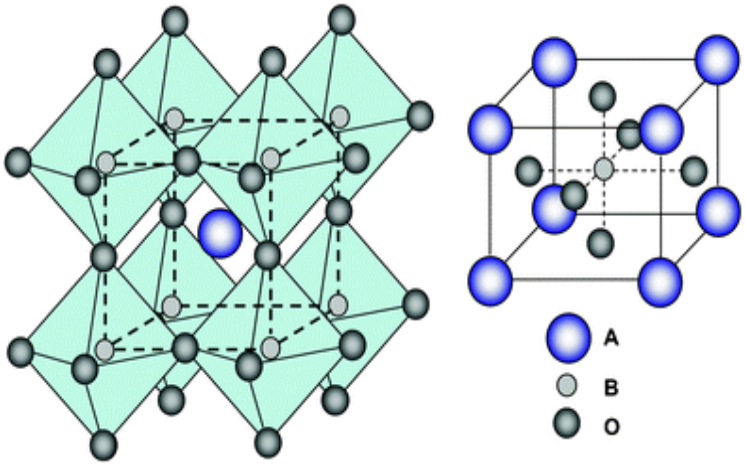

Perovskite-type oxides ideally have a cubical structure, wherein cations with a large ionic radius have 12-fold coordination with oxygen atoms, occupying *A* sites, and cations with a smaller ionic radius have 6-fold coordination, occupying *B* sites. *A* and *O* form cubic closets packing, and *B* is in the octahedral voids in the packing. In an ideal structure, where the atoms are simply bonding to one another, the *B–O* distance is equal to *a*/2 (*a*= length of unit cell), whereas the *A–O* distance is equal to $a/\sqrt{2}$ and the following relation between ionic radii holds:

$$(r_A + r_O) = \sqrt{2}(r_B + r_O) \qquad \text{Eq. 1.}$$

It has been found, however, that the cubic structure of perovskites can be still retained in an ABO_3 structure even though this equation is not strictly obeyed. As a measure of this deviation from ideal cubical structure, Goldschmidt (Goldschmidt V. M., 1926) introduced a *tolerance factor* (*t*), which is used to define the range of the ionic radii of *A* and *B* defined by the following equation, which is applicable at room temperature:

$$t = \frac{r_A + r_O}{\sqrt{2}(r_B + r_O)} \qquad \text{Eq. 2.}$$

For an ideal perovskite, *t* is unity; however, the perovskite structure is also found for lower values of *t* in the range 0.75 to 1. In such cases, the cubical structure can be distorted into tetragonal, rhombohedral, or other lower symmetries (Goldschimidt V. M., 1926). It should

be noted that perovskites with values of *t* greater than 1 having a hexagonal structure are also reported due to the larger ionic radii of the *A* ions or the smaller ionic radii of the *B* ions. $BaNiO_3$ is a well-known example of hexagonal perovskite structure where the value of *t* is 1.13 (Johnsson M. et al., 2006; Nagai T. et al., 2007).

1.2 Manganites

Manganite materials with the composition $R_{1-x}A_xMnO_3$ (R = rare earth elements such as La, Nd, Pr, and Sm, and *A* = divalent alkaline elements such as Ca, Ba, and Sr) have received increasing attention due to their special properties, such as colossal magnetoresistance (CMR), metal-insulator (MI) transition, and the magnetocaloric effect (MCE) (R. Von Helmolt, et al., 1993; G. Tang et al., 2008).

The parent $LaMnO_3$ compounds behave like paramagnetic (PM) insulators at higher temperatures and antiferromagnetic (AFM) insulator at lower temperatures (J. Hemberger et al., 2004). When the trivalent La is replaced by divalent Ca, Sr or Ba (hole doped) in the range $0.2 \leq x \leq 0.4$, the material becomes a metallic ferromagnet below the Curie transition temperature (T_C) (P. Lampen et al., 2013; I. Hussain et al., 2016). At $T < T_C$, the hole doped manganites are mixed valent system with a disordered distribution of Mn^{3+} and Mn^{4+} ions (L. W. Zhang et al., 2000). Here the Mn^{3+}- Mn^{4+} ferromagnetic (FM) interactions are dominant, along with AFM interactions associated with Mn^{3+}- Mn^{3+} and Mn^{4+}- Mn^{4+} pairs (T-Long Phan, et al., 2014). Electronically, the Hund coupled t_{2g} electrons may be considered as a single localized spin with $S = 3/2$, while the e_g electrons are strongly hybridized with oxygen 2*p* state (B. Chen et al., 1996). Through divalent doping, the corresponding number of Mn ions is converted into quadrivalent Mn^{4+} (t_{2g}^3) (S. Raj et al., 2001). This means that the divalent dopants introduce holes into the e_g - 2*p* band near the Fermi energy.

Among hole-doped manganites, $La_{0.7}Ca_{0.3}MnO_3$ (LCMO) has received particular attention because of its colossal magnetoresistance (CMR) and magnetocaloric effect (MCE) occurring around the T_C, which has promising application in magnetic refrigeration technology (D. N. H. Nam et al., 2008).

Although a large number of papers on MCE in perovskite-type manganese oxides have been published, recent reports show that some materials of this type can have larger magnetic entropy changes at the T_C, which are comparable to those reported for undoped Gd metal (M. H. Phan et al., 2007). Gd shows a large MCE at temperatures close the room temperature (A. M. Tishin et al., 2003), but it is an expensive element and tends to be subject to oxidation. Doping at the Mn site with other transition metals is of great importance in modifying the double exchange (DE) interaction strength between Mn^{3+} and Mn^{4+} *via* oxygen atoms. This alters the magnetic and magnetocaloric behavior of these doped oxides (L. W. Zhang et al., 2000). The partial substitution of Mn^{3+} by Ni^{2+} ions in manganites has been previously studied in connection with their magnetoresistive behavior (S. Liu et al., 2013; A. M. Ahmed et al., 2015).

1.2.1 Phase Diagram

As we have seen previously, superexchange and double exchange are both driven the magnetisms of $La_{1-x}A'_xMnO_3$ materials. The interplay between the two is some of the key interactions at the heart of the rich phase diagram of $La_{1-x}Ca_xMnO_3$, which is presented in Figure 1-1, starting from the undoped parent compound $LaMnO_3$ with a canted antiferromagnetic (CAF) insulating ground state. For doping level close to 10 %, the ground state is a charge order (CO) insulating and give place to a FM insulating states for higher temperature. This is seen up to a doping level of about 20 % where after that point up to 50 % the ferromagnetic interactions suppress the antiferromagnetic coupling and a ferromagnetic metal ground state dominated by double exchange is observed. This is the domain where colossal magnetoresistance is observed. Higher doping levels are not studied in this thesis. The figure is adapted from Kim et al., 2004.

Figure 1-1. Magnetic phase diagram of $La_{1-x}Ca_xMnO_3$ compound.

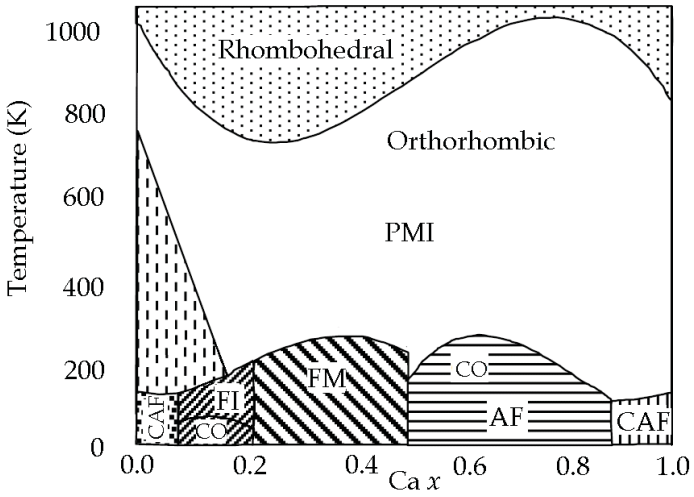

1.2.2 The Jahn-Teller Effect

In $La_{1-x}Ca_xMnO_3$, the Mn^{3+} has a high-spin configuration (S = 2) with all electrons being aligned (Hund´s coupling), with three of them sitting in the low t_{2g} orbitals and one in the high e_g. Jahn and Teller (1937) stated that the degeneracy of the e_g orbital will be removed by a distortion of the structure following the direction of two orbitals. In the case of $La_{1-x}Ca_xMnO_3$, we see an expansion of the *z* axis and a contraction of the *x* and *y* axes as shown in Figure 1-2. It is worth noting that this deformation may be a static or dynamic (Kiryukhin, et al., 2004).

Figure 1-2. Schematic of the splitting of *3d* orbitals of metallic ions inside an octahedral crystal field under a Jahn-Teller distortion. The figure uses octahedral from Lopes dos Santos et al., 2005.

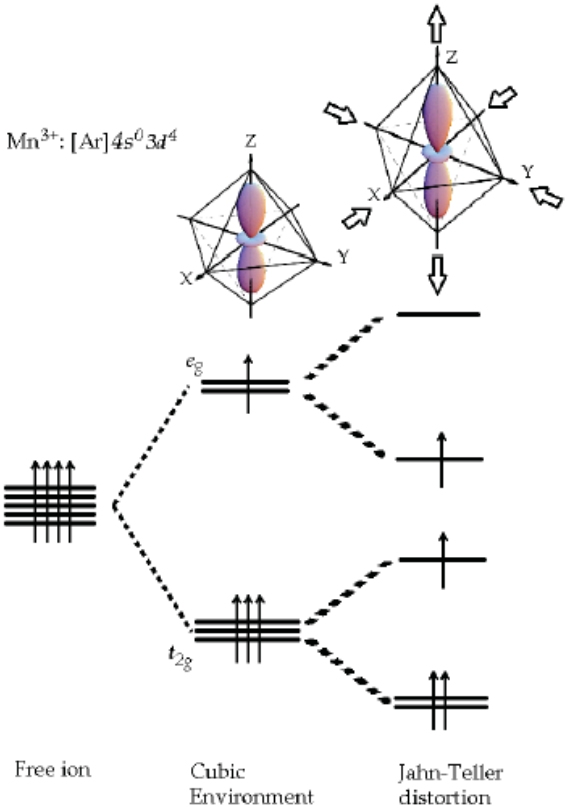

The effect of the Jahn-Teller (JT) distortion is making the material more stable, localizing the e_g electrons, *i.e.,* more insulating. However, there are some studies that shown that the comparative JT distortion in $La_{1-x}Ca_xMnO_3$, coming from the delocalization of the e_g electron, thus driving a long range ordering. It is often known as a *coherent* JT distortion (Radealli et al., 1997), who defines a JT parameter to quantify this distortion, σ_{JT}:

$$\sigma_{JT} = \sqrt{\frac{1}{3}\sum_{i=1}^{3}[(Mn-O)_i - \langle Mn-O\rangle]^2} \qquad \text{Eq. 3.}$$

σ_{JT} is actually the standard deviation of the three $(Mn-O)_i$ bond lengths from the average value $\langle Mn-O\rangle$.

Radaelli et al., 1997 showed a sharp reduction of the *coherent* JT distortion, σ_{JT}, at T_C, in $La_{0.75}Ca_{0.25}MnO_3$ which is consistent with the delocalization of the e_g electron, thus increasing the conductivity.

1.2.3 Colossal Magnetoresistance in Manganites

Under the application of a magnetic field, some materials experienced a drop of resistivity called magnetoresistance (MR), which is usually giving by the equation Eq. 4.:

$$MR(\%) = \frac{\rho_0 - \rho_H}{\rho_0} * 100\ \% \qquad \text{Eq. 4.}$$

In equation Eq. 4., ρ_0 and ρ_H are, respectively, the resistivity measured without and with application of magnetic field. The sign of MR can be positive of negative depending on the increase or drop in the resistivity when a magnetic field is applied.

It was advanced in the sixties that the double-exchange mechanism was the source of magnetic coupling in manganites (Zener, 1951; de Gennes, 1960). Localized Mn t_{2g} spins are being mediated by itinerant e_g spins hopping through oxygen atoms *via* metallic bonds. The more hopping of spins is bringing the system closer to the metallicity regime which consequently corresponds to the ferromagnetic regime. Additional effect as electron phonon interaction arising from the JT splitting of Mn *d* levels have been added to these theories later to explain the drastic change of bandwidth at the transition (Millis et al., 1995).

Figure 1-3. corresponds to phase diagram for the conduction mechanism in the $La_{1-x}Ca_xMnO_3$ materials as a function of the x dopant content, which was published by Lynn et al., 2007 American Physical Society.

Figure 1-3. Conduction mechanism phase diagram for $La_{1-x}Ca_xMnO_3$ manganites.

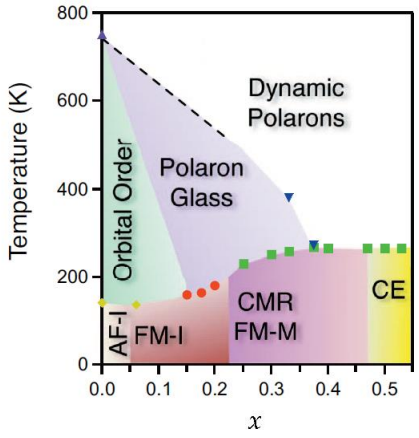

Further studies on the subject concluded that these local distortions revealed by an anomalous thermal expansion between the Curie-Weiss transition temperature T_C and a higher temperature T^*, are pointing towards the presence of ferromagnetic clusters or polarons being responsible for the electrical conduction (De Teresa el al., 1996, 1997; Ibarra et al., 1997). These clusters are said to be present only in a large type below the metal-insulator temperature transition, and in small and large types above the same transition (Lanzara et al., 1998). An important feature is that polaron formation revealed by neutron scattering and metal-insulator cross-over occurs at temperatures very close from one another (Adams et al., 2000). In addition Kiryukhin et al., 2004, first showed using neutron scattering that correlated nanoscale lattice distortion are present only in orthorhombic structures, and not in rhombohedral ones. Then Lynn et al., 2007, pursuing the study of the nature of the polaron order and dynamics in $La_{0.7}Ca_{0.3}MnO_3$, demonstrated that a polaron glass phase, characterized by short-range polaron correlation, is present between T_C and a higher temperature T^* above which the correlations are purely dynamic.

Another approach to explain the CMR in manganites and the presence of clusters in the paramagnetic region have been to associate this behavior with one observed in Griffiths phases. Griffiths (1969) showed in his paper that a continuation on the first-order transition is represented for temperatures below T_C when only a percentage of lattice sites are occupied by interacting Ising spins, in a random Ising ferromagnet.

1.2.4 Magnetocaloric Effect in Manganites

Manganites are nowadays being put under the spotlight once again for their use in magnetic refrigeration at room temperature (Phan et al., 2003; Phan and Yu, 2007; Zhang et al., 2012), even though their isothermal entropy change and adiabatic temperature change are rather low. Figure 1-4. shows a Ashby map of magnetic refrigerants.

Figure 1-4. Ashby map of magnetic refrigerants: ΔT_{ad}^{Max} vs ΔS_{Iso}^{Max} under a 2 T magnetic field change. Sandeman, 2012.

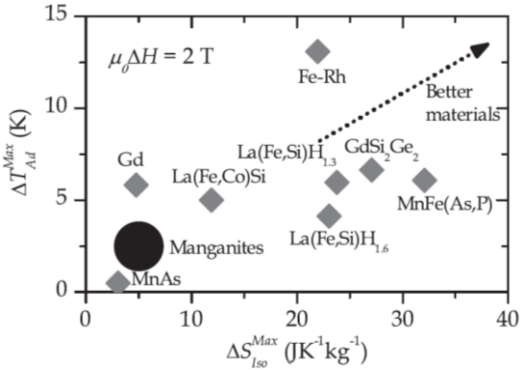

What makes the manganites so attractive them is that they are inexpensive, *i.e.,* cheaper than Gd which has been the reference in the magnetic refrigeration so far. In addition, manganites are non-toxic and very importantly, they are easy to process and to shape.

Among manganites, $La_{1-x}(Ca, Sr)_xMnO_3$ have attracted most of the attention for having high magnetocaloric effect close to room temperature (Gschneidner et al., 2005; Dinesen et al., 2005). Around x = 0.3 where the MCE is highest, Ca based samples exhibit first order transition from a paramagnetic insulator to a ferromagnetic metal at around 240 – 260 K depending of the oxygenation state, particle size (Markovic et al.) and crystallinity (Debnath et al., 2012; Im et al., 2007). Mira et al., 2002 closely studied x = 0.33 compounds and found out a key condition of having a large isothermal entropy change and consequently a large MCE, was the necessity for the material to exhibit a first order behavior of the transition which was associated with the materials having an orthorhombic *Pnma* structure (tolerance factor $t < 0.92$) and not a rhombohedral *R-3C* structure ($t > 0.92$). A sharp volume change at T_C was observed for the first class and not the second one.

1.3 Models of the magnetocaloric effect

To find new magnetocaloric materials it is necessary to understand the mechanism of large MCE (or even small MCE) reported in already known alloys and compounds. The models developed for their magnetothermal responses can facilitate the discovery of modifications, which would even further enhance their performance. In addition, models developed for a known material can be useful for predicting its response under different excitation conditions. If the model properly developed, the time hassle in validation

experiments can be minimized as only select excitation conditions should be measured; subsequently, the performance of a device could be predicted by using the model.

The classification of models used in this field of research can be made between thermodynamic models and first principle models. Thermodynamic models are less capable for the identification of new materials but are extremely useful to evaluate the response of known materials (and some computational variations) under multitude of excitation conditions. Therefore, they are also suitable to be introduced in models of the performance of magnetic refrigerators. First principle models are generally more suitable to predict the behavior of unknown alloys and compounds, streamlining the search for new compositions but that require a detailed knowledge of the possible phases that will be present in the material. The main characteristics of the most representative cases of both families will outline in this section (V. Franco et al., 2018).

1.3.1 Thermodynamic models

These models use macroscopic variables to describe the change of the magnetization with field and temperature. In many cases, this is made via equations of state (EOS), which link the magnitudes *M, H,* and *T*, and variables that describe the material under study are identified by fitting the experimental measurements to those EOS. Alternatively, precise models have been developed to reproduce the hysteretic behavior of first order phase transition (FOPT) (Basso V, et al., 2005).

For second order phase transition (SOPT), the EOS can be obtained from a power expansion of the thermodynamic potential following the formalism of Landau (Kuz´min, 2008). Depending on the number of the terms that we kept in the power expansion, the description can be almost accurate including corrections to the firs order mean field approximation. Other alternative is to use a heuristic approach to tailor a known EOS to the material by including additional features known to be fulfilled in it. An example of this type of EOS is that of Arrot-Noakes (Arrot A. et al., 1967), wherein the critical behavior with exponents different from those of the mean field ones was incorporated:

$$H^{\frac{1}{\gamma}} = a(T - T_C)M^{\frac{1}{\gamma}} + bM^{\frac{1}{\beta}+\frac{1}{\gamma}} \quad \text{Eq. 5.}$$

Where *a* and *b* are characteristic parameters of the material under study, β and γ are the critical exponents. In this way, is possible to control the universality class to which the material belongs. This EOS has been extensively used for the study of SOPT magnetocaloric materials (Franco V. et al., 2006; Franco V. et al., 2008; Fan J. Y. et al., 2011; Zhang L. et al., 2011) and was the initial basis on which the scaling of magnetocaloric response and its universal curves was founded (Franco V. et al., 2006; Franco V. et al., 2010). The phenomenological construction of the universal curve, which was also extended to ΔT_{ad} (Franco V. et al., 2009) has been used to predict the behavior of samples in experimental conditions that were not available in the laboratory (*i.e.,* larger magnetic fields or temperatures not within the experimental limits of the device).

The Bean and Rodbell (Bean C. and Rodbell D., 1962) model was initially developed to study the FOPT in MnAs compound. Based on experimental results, the phenomenological dependence of the exchange interaction on the inter-atomic spacing was considered and was introduced into dependence of critical temperature on the volume change. With a control parameter η, the order of the transition from SOPT ($0 \leq \eta \leq 1$) to FOPT ($\eta > 1$) can be modified. Recently, it has been shown that the case $\eta = 1$ corresponds to the tricritical point, *i.e.,* to the separation of first and second order phase transition, and the critical exponents coincide with those associated to that special point (Romero-Muniz C. et al., 2017).

1.3.2 First principle models

The use of first principles calculations of exchange coupling energies and magnetic moments of magnetocaloric materials has become a usual procedure in the study of first order phase transition materials (Harmon B. N. et al., 2002; Mihalik M. et al., 2004; Paudyal D. et al., 2006; Buchelnikov V. D. et al., 2010; Entel P. et al., 2013; Korotana R. et al., 2016; Li G. J. et al., 2016).

In most of cases, modeling is performed with a two-stage approach (Paudyal D. et al., 2006; Korotana R. K. et al., 2016). Firstly, first principle calculations, using Density Functional Theory (DFT) are used to predict the zero temperature properties of the material; subsequently, the obtained magnitudes are used as inputs in thermomagnetic models, such as the Bean-Rodbell model (Bean C. and Rodbell D., 1962), to extract

information about the values of magnetization at finite temperatures, magnetic entropy, magnetostructural transition temperatures, and MCE.

In general, a good agreement is found between the experimental results and the outcome of the models. However, it has to be considered that such models require a fair amount of details of the studied material, which somehow limits the predictive power to materials relatively similar to those previously analyzed (V. Franco et al., 2018).

2. Experimental details

In this chapter the experimental details related with the sample preparation by means of the standard solid state reaction and combustion solution processes for $La_{0.7}Ca_{0.3}Mn_{1-x}Ni_xO_3$ (x=0, 0.02, 0.07, 0.1) polycrystalline samples are described. Also the characterization techniques used to identify, quantify or qualify the samples in accordance with their structural, morphological, magnetic, magnetocaloric and electrical properties are briefly introduced.

2.1 Sample preparation

2.1.1 Standard solid state reaction

Polycrystalline samples of the $La_{0.7}Ca_{0.3}Mn_{1-x}Ni_xO_3$ (x = 0, 0.02, 0.07, 0.1) manganites were synthesized by means of this physical process, in which; as was mentioned in the previous section; the process consist on to mix the reactants in powder form in an appropriate stoichiometric ratio. The used raw materials were La_2O_3 (lanthanum (III) oxide) REacton 99.9% (REO) Powder Alfa Aesar, $CaCO_3$ (Calcium carbonate) 99% Carlo Erba Powder, MnO_2 (Manganese (V) Oxide), 99.9% (Metal Basis) -325 Mesh Powder. Alfa Aesar, and NiO (Nickel (II) Oxide), 99% (Metal Basis) -325 Mesh Powder Alfa Aesar. Prior to weighing, the reagents were dried in a furnace to eliminate the moisture. Then the reactants were weighed in an appropriate stoichiometric ratio to obtain 1 g of every composition. The weigh measurements were carried out by means of an analytical balance with 0.01 mg resolution. Next all weighed powders were mixed for 30 min in agate mortar to homogenize the powder mixture. Finally a calcination process in a tubular furnace from room temperature to 1200 °C at 3 °C/min for 42 h in air atmosphere was carried out. The samples were cooling down in the inner of the furnace. The synthesized powders were then grinded in agate mortar for 15 min to disaggregate the obtained powders and to obtain samples with a more homogeneous grain sizes distribution.

The chemical reaction that describes the standard solid state reaction process for these compounds can be expressed as Eq. 2.1:

$$\frac{7}{20}La_2O_3 + \frac{1}{3}CaCO_3 + (1-x)MnO_2 + xNiO \rightarrow La_{0.7}Ca_{0.3}Mn_{1-x}Ni_xO_3 + \frac{1}{3}CO_2 + \frac{69}{100}O_2 \quad (2.1)$$

All stages of this preparation process were carrying out in the laboratory of metallography, Facultad de Ingeniería, Institución Universitaria Pascual Bravo, Medellín, Colombia.

2.1.2 Combustion solution method

The synthesis of polycrystalline $La_{0.7}Ca_{0.3}Mn_{1-x}Ni_xO_3$ (x = 0, 0.02, 0.07, 0.1) manganite samples has been reported in a previous paper [2-72, 2-73] as a part of the development of this thesis. In this method, glycine ($C_2H_5NO_2$) ACS reagent ≥ 98.5% Sigma-Aldrich was used as a fuel. Lanthanum (III) nitrate hexahydrate ($La(NO_3)_3.6H_2O$) 99.99% trace metals basis Aldrich, calcium nitrate tetrahydrate ($Ca(NO_3)_2.4H_2O$) ≥ 99% Sigma-Aldrich, nickel (II) nitrate hexahydrate ($Ni(NO_3)_3.6H_2O$) 98% Alfa Aesar, and manganese (II) acetate tetrahydrate ($Mn(C_2H_3O_2)_2.4H_2O$) ≥ 99% Aldrich, were used as starting materials. All the reactants were of analytical grade. After complete dilution of the starting materials and the fuel in distiller water, based on the stoichiometric quantities, the solution was heated (under magnetic stirring) on a hot plate at around 100 °C until water evaporation and a gel formation took place. After that, the mixture was continuously heated at around 450 °C until ignition of the glycine started. Once ignited, the gel underwent a combustion process and yielded voluminous $La_{0.7}Ca_{0.3}Mn_{1-x}Ni_xO_3$ powders. The obtained powders were then calcined in air at 700 °C for 3 h in order to remove the unreacted carbon compounds and the organic material. The obtained powders were then grinded in agate mortar for 5 min to disaggregate the obtained powders and to obtain samples with a more homogeneous grain sizes distribution.

The chemical combustion reaction can be expressed as Eq. 2.2:

$$\frac{7}{10}\,La(NO_3)_3 + \frac{1}{3}Ca(NO_3)_2 + (1-x)Mn(C_2H_3O_2)_2 + xNi(NO_3)_2 + yC_2H_5NO_2 \rightarrow$$
$$La_{0.7}Ca_{0.3}Mn_{1-x}Ni_xO_3 + aCO_2 + bN_2 + cH_2O \qquad (2.2)$$

All stages of this preparation process were carrying out in the Ceramic and Glass Materials laboratory, Facultad de Ciencias, Universidad Nacional de Colombia, campus Medellín, Colombia.

2.2 Characterization techniques

2.2.1 Structural properties

Phase identification, crystalline structure, lattice parameters, crystalline size, unit cell volume, among others, of final $La_{0.7}Ca_{0.3}Mn_{1-x}Ni_xO_3$ (x=0, 0.02, 0.07, 0.1) manganites powders obtained by means of standard solid state reaction and combustion solution processes was carried out using X-ray diffraction (XRD) technique on a PANalytical Empyream high resolution diffractometer in the Bragg-Brentano reflection geometry with Cu $K\alpha$ radiation source (λ = 1.5406 Å). The data were collected at fixed scanning 0.01° steps over a 2θ axis range from 20° to 80°. The diffraction patterns of these collected data were plot and then analyzed by means of the specialized software GSAS [3-1] by using the utility for Rietveld refinement method.

The used diffractometer equipment is placed on the Facultad de Química, Universidad de Antioquia, Medellín, Colombia

XRD is non-destructive and provide information, among others, about unit cell parameter dimensions. Its principle is based on the diffraction by crystallographic lattice of collimated X-rays. By applying a voltage across electrodes in a X-ray vacuum tube, electrons are drawn toward a metal target (the anode). At the point of impact, X-rays are produced and radiate. The fact that a lattice diffracts X-rays is due to the angstrom scale of the electromagnetic radiation wavelength of the X-rays. Usually a cooper target is used since it produces a characteristic polychromatic radiation made of sharp components. After filtering it can be tuned to quasi monochromatic with to very close radiations $K\alpha_1$ and $K\alpha_2$ at a de Broglie wavelength comparable to typical distance between to atoms, *i.e.,* 1.5

angstroms. If an incident X-ray beam encounters a crystal lattice, which is made of parallel planes of atoms called Miller planes and described by indices *hkl* corresponding to their interception with the *x, y* and *z* axes, then each electron cloud diffracts a spherical wave. Although the spherical waves cancel one another in most directions (destructive interference), there is, for each set of planes, a direction that forms an angle θ_{hkl} with the planes, along which the interferences are constructive. The incident angle θ_{hkl} is giving by Bragg´s Law. Eq. (2.3):

$$2d_{hkl}sin\theta_{hkl} = n\lambda \qquad (2.3)$$

where d_{hkl} correspond to the distance between two parallel planes, λ is the X-ray wavelength, and the integer *n* is the order of the reflection which is fixed to 1 by convention in X-ray diffraction analysis. High order reflections can always by described by the first order reflections being due to set of different crystallographic planes with indices that are multiples on *n*.

2.2.2 Morphology

The surface morphologies and the particle sizes of the final $La_{0.7}Ca_{0.3}Mn_{1-x}Ni_xO_3$ (x=0, 0.02, 0.07, 0.1) powders obtained from the two used synthesis processes, were examined using field emission scanning electron microscopy (FE-SEM) and transmission electron microscopy (TEM) techniques. In accordance with the kind of equipment used several operational conditions as: operation voltage, work distances, spot sizes, secondary electron or backscattered mode operation, were adjusted to acquire images at different magnification scales.

Two kind of equipment SEM were used to acquire the images of the present thesis. The first one was a JEOL JSM 7100F model FE-SEM, built-in the Laboratorio de Microscopía Electrónica de Barrido, Parque-i, Institución Universitaria Instituto Tecnológico Metropolitano (I.U.I.T.M), Medellín, Colombia. The second one was a Hitachi S-5200 model HR-FESEM (High Resolution), it which is located in Centro de Investigación,

Tecnología e Innovación, Consejo Superior de Investigaciones Científicas (CITIUS–CSIC), Campus Avenida de Reina Mercedes, Sevilla, España.

SEM is a reflective type of electron microscope capable of producing high-resolution images of a sample surface by shooting electrons at it and by collecting the resulting emission with a detector. The beam of electrons is produced by an electron gun. The beam is then focused toward the sample by travelling through electromagnetic fields and lenses. When hitting the surface of the sample, different types of emission made of either secondary electrons, backscattered electrons or X-ray are produced due to the interaction of the primary electron beam with the atoms of the sample. The majority of electrons released by the surface are coming from a few nanometers deep in the surface and are made of secondary electrons which energies are low enough, *i.e.* about 50 eV, to be deflected by a low bias voltage and easily collected. These types of electrons provide localized information of the surface topography.

Compared with conventional SEM, FE–SEM produce clearer, less electrostatically distorted images with spatial resolution down to 1 ½ nanometers – three to six times better, it which allow a this technique to acquires topographical information at magnifications of 10X to 300000X with virtually unlimited depth of field.

Another advanced technique to observe the particles morphology and sizes of the obtained powder samples, was the TEM. A FEI Talos F200S for Materials Science model TEM, it which is placed on Centro de Investigación, Tecnología e Innovación, Consejo Superior de Investigaciones Científicas (CITIUS–CSIC), Campus Avenida de Reina Mercedes, Sevilla, España.

There are four main components to a transmission electron microscope (TEM): an electron optical column, a vacuum system, the necessary electronics (lens supplies for focusing and deflecting the beam and the high voltage generator for the electron source), and control software. A modern TEM typically comprises and operating console surmounted by a vertical column and containing the vacuum system, and control panels conveniently placed for the operator. The microscope may be fully enclosed to reduce interference from environmental sources, and operated remotely. The electron column includes elements analogous to those of a light microscope. The light source of the light

microscope is replaced by electromagnetic lenses. Unlike glass lenses, the power (focal length) of magnetic lenses can be changed by changing the current through the lens coil. The eyepiece or ocular is replaced by a fluorescent screen and/or digital camera. The electron beam emerges from the electron gun, and passes through a thin specimen, transmitting electrons which are collected, focused, and projected onto the viewing device at the bottom of the column. The entire electron path from gun to camera must be under vacuum.

The most important differences between a TEM and a SEM are: – Rather than the broad static beam used in TEM, The SEM beam is focused to a fine point and scans line by over the sample surface in a rectangular raster pattern. – The accelerating voltage is much higher than in SEM because it is longer necessary to penetrate the specimen. – The specimen need be thin.

The interactions between the beam electrons and sample atoms are similar to those described for a SEM: – The specimen itself emits secondary electrons. – Some of the primary electrons are reflected backscattered electrons (BSE). These backscattered electrons can also cause the emission of secondary electrons as they travel through the sample and exit the sample surface. All these phenomena are interrelated and all of them depend to some extent on the topography, the atomic number, and the chemical state or the specimen.

2.2.3 Magnetic properties

The final powders of $La_{0.7}Ca_{0.3}Mn_{1-x}Ni_xO_3$ (x=0, 0.02, 0.07, 0.1) manganites obtained by means of standard solid state reaction and combustion solution processes were examined for the change in their magnetic properties taken into account intrinsic and extrinsic factors. The intrinsic factors are represented by a change in magnetic interaction mechanisms such as the ferromagnetic DE (Mn^{3+}–O–Mn^{4+}), while the extrinsic factors can arise, *e.g.,* from a change in the grain size. To study the magnetic behavior, several curves such as magnetization versus temperature at different magnetic field strength (*M(H) vs T*) and magnetization versus magnetic field strength at different temperatures

(*M(T) vs H*) were recorded at smalls discrete fields and temperature intervals ΔT = 5 K, using a Vibrating Sample Magnetometer VSM Quantum Design VersaLab 3T model, it which is located in the Facultad de Física, Universidad Tecnológica y Pedagógica de Colombia, Tunja, Colombia. The obtained data were processed in software to data analysis such as Origin, Excel and Matlab. Parameters as the Curie temperature (T_C), the Curie constant (C), The Weiss temperature (θ_P) and the experimental $\left(\mu_{eff}^{exp}\right)$ and theoretical effective paramagnetic moment $\left(\mu_{eff}^{theo}\right)$ were extracted from the measurements.

The vibrating sample magnetometry is a fast and sensitive technique to determine a sample´s magnetic dipole moment. The moment arises from material´s magnetization density which is a fundamental thermodynamic quantity. This tool can be used to study phenomena such as superconductivity, ferromagnetism, superparamagnetism among other. Basically the measure principle of the VSM is the Faraday´s law of induction, that is, changes in the magnetic flux will produce a measurable voltage.

Figure 2-1: Schematic of sample holder and VSM mechanism invented by Simon Foner at MIT in 1959 [3-2].

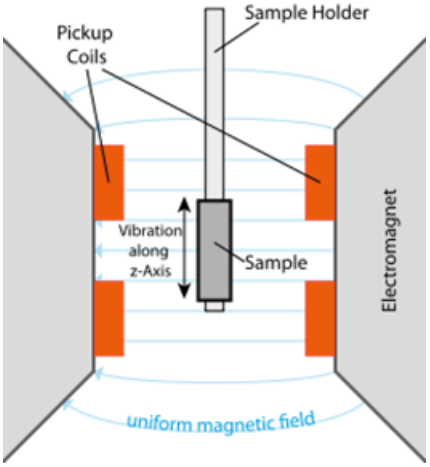

A sample to be studied is placed inside the uniform magnetic field and then vibrated sinusoidally using vibrator made of linear actuators or modified audio speaker. The induced voltage in the pickup coil is proportional to the sample's magnetic moment, but does not depend on the strength of the applied magnetic field. In a typical setup,

the induced voltage is measured through the lock-in amplifier using the piezoelectric signal as its reference signal. Lock-in principle of measurement allows the measurement of signal weaker than the noise. By measuring in the field of an external electromagnet, it is possible to obtain the hysteresis curve of a material. VSM measures the magnetization of a small sample of magnetic material placed in an external magnetization field by converting the dipole field of the sample into an AC electrical signal.

The basic principle with sinusoidal motion is giving as Eq. 2.4

$$V = -\frac{d\Phi}{dt} = CmA\omega \sin(wt) \qquad (2.4)$$

where, Φ is the magnetic flux, *C* is a coupling constant, *A* is the vibration amplitude, ω is the frequency and *m* is the magnetic moment of the sample

2.2.4 Magnetocaloric effect (MCE)

The magnetocaloric effect (MCE) for the obtained powder compounds was estimated in terms of isothermal magnetic entropy change ($-\Delta S_M$) using the magnetization data and employing the Maxwell relation $\Delta S_M = \mu_0 \int_0^{H_{max}} \left(\frac{\partial M}{\partial T}\right) dH$, where $\mu_0 H$ is the external magnetic field. For the magnetization measurement made discrete field and temperature intervals, $\Delta S_M(T, H)$ was approximately calculated by the following expression. Eq. 2.5:

$$\Delta S_M(T,H) = \sum_i \frac{M_{i+1}(T_{i+1},H) - M_i(T_i,H)}{T_{i+1} - T_i} \Delta H \qquad (2.5)$$

The nature of the magnetic phase transition in the samples was determined by plotting the Arrot plots *H/M* versus M^2 curves. In accordance with the Banerjee criteria, the sign of the slope of theses curves were indicating the phase transformation order. The relative cooling power (RCP) values of the obtained sample compounds can be determined by means of the relation $RCP = -\int_{T_1}^{T_2} \Delta S_M(T) dT$, where T_1 y T_2 are defined as the temperature at cold and hot ends, respectively, of and ideal thermodynamic cycle. For practical purposes, the RCP values were evaluated using the equivalent relation RCP =

$|\Delta S_{M,max}| x \delta T_{FWHM}$. Here δT_{FWHM} represents the full-width at half maximum of the magnetic entropy change curve. Critical exponents related with the MCE were calculated with base in the Arrot and Kouvel–Fisher assessment methods. The critical exponents calculated were adjusted in accordance to the Rushbrooke and Widom fitting laws. The relation between MCE and electrical transport properties were studied with base on the phenomenological model described as Eq. 1.23, it which was previously described in the earlier chapter of this thesis. Eq. 2.6:

$$\Delta S_M(T,H) = -\alpha \int_0^H \left[\frac{\partial \ln(\rho)}{\partial T}\right]_H dH \qquad (2.6)$$

2.2.5 Electrical properties

The electrical measurements were carried out on pellets (sintered at 1200 °C for 24 h) of $La_{0.7}Ca_{0.3}Mn_{1-x}Ni_xO_3$ (x = 0, 0.02, 0.07, 0.1) manganites synthesized by standard solid state reaction and combustion solution processes. The technique used to measure their electrical properties was the standard four point Van Der Pauw integrated into a physical properties measurement system (PPMS) in the temperature range of 5–300 K and magnetic fields varying between 0 and 5 T. A Wimbush press contact assembly was used to mount the pellets in the equipment sample holder. Curves of resistivity versus temperature at various magnetic field strengths ($\rho(H)$ vs T) and resistivity versus magnetic field at various temperatures ($\rho(T)$ vs H) were plotted. From these data was possible to draw the magnetoresistance (MR) as a function of temperature and magnetic field strength. The magnetocaloric effect – electrical transport properties relationship was analyzed taken into account the relation described by Eq. 2.6. Also the electrical transport mechanism as the electron – electron scattering and electron magnon scattering, as well as the conduction process (small polaron hopping, among others) was possible to evaluate from these measurements.

The measurements of these properties were carried out in a physical properties measurement system (PPMS) Quantum Design 9T model placed on the Instituto de Ciencia de Materiales de Madrid, Consejo Superior de Investigaciones Científicas (ICMM – CSIC), Madrid, España.

The PPMS is an automated low-temperature and magnetic system for the measurement of material properties like specific heat, magnetic AC and DC susceptibility and both electrical and thermal transport properties (like Hall Effect, thermoelectric figure of merit and Seebeck Effect). The temperature can be varied continuously between 1.9 K and 400 K, while a magnetic field of up to +/- 16 Tesla can be applied. The base unit of the PPMS consists of a cryostat with a superconducting magnet coil. The different measurement options result from the use of different measurement inserts or sample holders and activating the according software mode.

In typical resistivity measurements, 4 electrical leads are attached to a rectangular sample along a straight line [Fig. 2-2 (a)]. A current is fed from contact A to contact B, and the voltage is measured across contacts C and D, which must be far away from the current contacts in order for the lines of current flow to be uniform and parallel between C and D.

The resistivity of the sample can be derived from the voltage drop across contacts C and D, the applied current, and the geometry of the sample. Frequently the sample does not have a geometry that is favorable for the above style measurement, leading to an unknown current distribution. Also, it is often difficult to determine accurately the geometry of the sample, limiting the accuracy of the calculated resistivity. In such a case, one often uses the technique of Van Der Pauw to determine the resistivity of the sample. A common geometry for such a measurement has 4 electrical contacts at the 4 corners of a roughly square sample [Fig. 2.2 (b)]. However, the Van Der Pauw technique is applicable for an arbitrary shaped sample as long as the thickness of the sample is known and is uniform, the contact areas are small, and the contacts are all on the perimeter of the sample. In this case Van Der Pauw showed that: $exp(-\pi R_{AB,CD}d/\rho) + exp(-\pi R_{BC,DA}d/\rho) = 1$ where d is the thickness of the sample, ρ is the resistivity, $R_{AB,CD}$ is the resistance determined by dividing the potential difference $V_D - V_C$ by the current going from A to B, and $R_{BC,DA}$ is defined similarly. After measurement of the thickness of the sample and the two resistance values, the resistivity is determined simply inverting Van Der Pauw's relation.

Figure 2-2: (a) Conventional resistivity measurement. (b) Typical Van Der Pauw measurement.

(a)

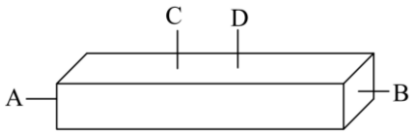

(b)

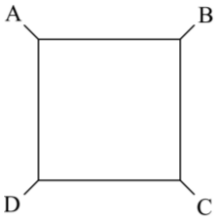

3. Results and discussion

The obtained images, curves, values, tables, models, fitting laws and so on resulting from the different kind of characterization techniques or behavior analysis are reported in this section. Also a discussion about findings in this study is given. The section 3.1 is related to the results about the structural properties, morphology, magnetic properties, and magnetocaloric effect (MCE) of the $La_{0.7}Ca_{0.3}Mn_{1-x}Ni_xO_3$ (x = 0, 0.02, 0.07, 0.1) polycrystalline samples synthesized by combustion solution and standard solid state reaction processes. In the same way, the 3.2 section is related to the electrical transport properties results and the correlation between these properties with the MCE for the $La_{0.7}Ca_{0.3}Mn_{1-x}Ni_xO_3$ (x = 0, 0.02, 0.07, 0.1) manganites synthesized by means of the two mentioned synthesis routes.

3.1 Properties characterization

3.1.1 Structural

Figure 3-1 (a) and (b) shows the full profile fittings; using GSAS program [4-4]; for the XRD patterns of $La_{0.7}Ca_{0.3}Mn_{1-x}Ni_xO_3$ (x = 0, 0.02, 0.07, 0.1) samples recorded at room temperature and synthesized by means of combustion solution and conventional solid state reaction process, respectively. A very good fitting of the experimental and the calculated data was obtained. No additional diffraction peaks stemming from impurities or secondary phases are observed. Additional diffraction peaks have been reported for other Ni^{2+}-doped manganites such as $La_{0.7}Sr_{0.3}Mn_{1-x}Ni_xO_3$ (x = 0, 0.025, 0.050, 0.075, 0.1) prepared with the conventional solid-state reaction method [4-1]. The additional peaks disappeared with doping, which was attributed to enhancement of the reaction between elements due to the larger ionic size of Ni^{2+} compared with Mn^{3+} [4-2]. The Ni^{2+} element is

an interesting transition metal for Mn-site substitution, where the combination of Ni^{2+} with Mn^{4+} is favorable [4-3]. As a result of the Rietveld refinement of the XRD patterns, the crystalline structure was indexed in the orthorhombic system with the *Pnma* space group for the samples synthesized by means of combustion solution and conventional route. An enlarged scale of the most intense peak (*2 0 0* Bragg reflection) of the XRD patterns shows a shift to lower 2θ values for the samples synthesized by combustion solution process [Fig. 3-1 (c)] indicating that the cell parameters (and thus the unit cell volume) increases with increasing Ni^{2+} content and consequently the average grain size should decrease. A contrary behavior is observed in Fig. 3-1 (d) for the same peak of samples synthesized by conventional route, in which a shift to higher 2θ values is presented, by giving as result a decrease in the unit cell volume and then a decrease in the same value as a consequence of the increasing Ni^{2+}-doping level such as was observed by P. Zhang et al. [a] for $La_{0.7}Ca_{0.3}Mn_{1-x}Ni_xO_3$ (x = 0, 0.05, 0.1) samples synthesized by means of the same process. Similar behavior, first increase and then decrease; or to the contrary; is shown in the a and $b/\sqrt{2}$ lattice constant, respectively. The changes in the lattice constants are attributed to the various valences of the Ni ions with different radius (Ni^{2+}, 0.69 Å, Ni^{3+}, 0.56 Å, Ni^{4+}, 0.58 Å). Zhang et al. [16] has found the presence of Ni^{2+} ions in $La_{0.7}Sr_{0.3}Mn_{1-x}Ni_xO_3$, where the lattice constants increase with increasing Ni-doping. Krishnamoorthi et al. [25] has also reported the same phenomenon in $La_{0.5}Ca_{0.5}Mn_{1-x}Ni_xO_3$. However, Phan [26] has reported the existence of Ni^{3+} ions in $La_{0.7}Sr_{0.3}Mn_{0.98}Ni_{0.02}O_3$. From the above studies, it is may deduce that there are different valences of manganite in $La_{0.7}Ca_{0.3}Mn_{1-x}Ni_xO_3$. It this case, for x = 0.02, the valence of the majority of Ni ions are bivalent; however for x = 0.1, the contents of Ni^{3+} ions may increase. Hence, the lattice parameters first increase due to the presence of Ni^{2+}, then decrease due to the increased content of Ni^{3+}. For x = 0.07 and x = 0.1, the (2 0 0) Bragg reflection shows a shift to higher 2θ values, which means that lattice distortion exists in $La_{0.7}Ca_{0.3}Mn_{1-x}Ni_xO_3$ manganites at these doping levels synthesized by means of solid state reaction. The decrease in the lattice constant and cell volume may cause a decrease in the Mn–O–Mn bond angle and increase the Mn–O bond distance, which are important factors to the Curie temperature [27]. The results of the Rietveld refinement are summarized in Table 3-1 and Table 3-2 for combustion solution and solid state reaction synthesized samples, respectively. The variation of the lattice parameter *a, b/√2, c,* and the unit cell volume *V* with respect to the

Ni^{2+} doping are shown in Fig. 3-2 (a) and (b) for $La_{0.7}Ca_{0.3}Mn_{1-x}Ni_xO_3$ (x = 0, 0.02, 0.07, 0.1) samples synthesized by combustion solution and solid state reaction, respectively.

Figure 3-1: (a) and (b) X-ray diffraction patterns recorded at 300 K for $La_{0.7}Ca_{0.3}Mn_{1-x}Ni_xO_3$ (x = 0, 0.02, 0.07, 0.1) samples synthesized via the combustion solution and standard solid state reaction process, respectively. The refined profiles as well as the difference profile are shown at the bottom. (c) and (d) (2 0 0) Bragg reflection plotted on enlarged scale for $La_{0.7}Ca_{0.3}Mn_{1-x}Ni_xO_3$ (x = 0, 0.02, 0.07, 0.1) samples synthesized by means of auto combustion and conventional solid state process, respectively.

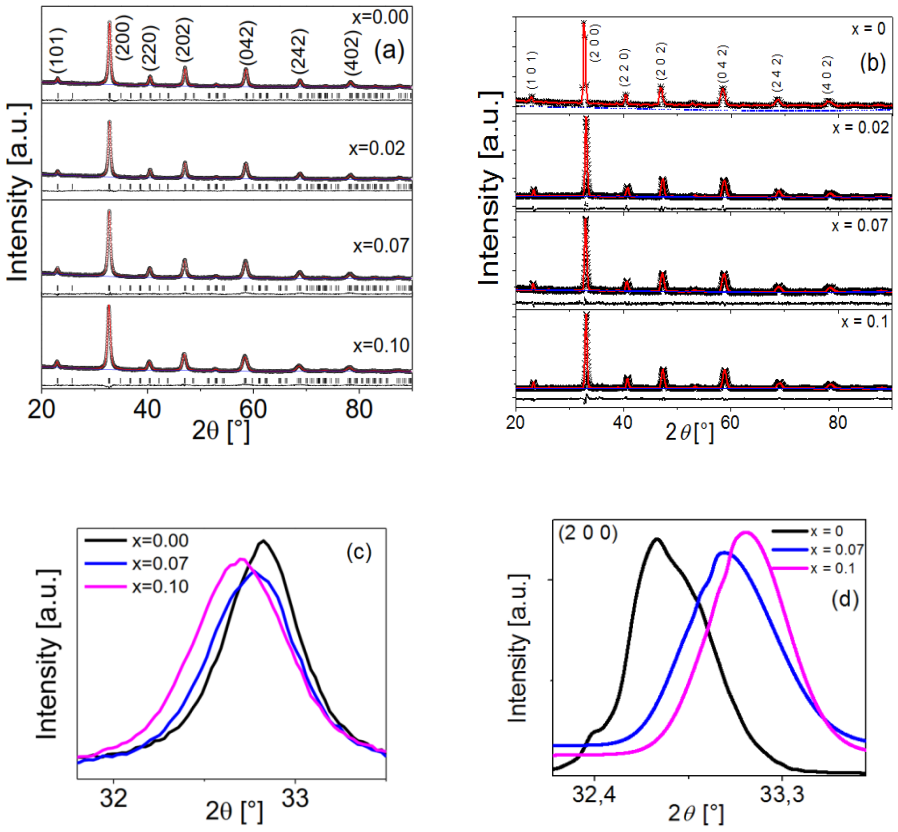

Figure 3-3 (a) shows the variation of the average crystallite size calculated from the Rietveld refinement as a function of the Ni^{2+} content for the samples synthesized by means of the processes: combustion solution and standard solid state reaction. A systematic decrease in the grain size upon Ni^{2+} doping is clearly in evidence for combustion solution synthesized samples, while an increase for samples up to 7 % of Ni^{2+} content and then an abrupt decline for $La_{0.7}Ca_{0.3}Mn_{0.9}Ni_{0.1}O_3$ sample is observed for

conventional process synthesized samples. In Fig. 3-3 (b) a comparison in the volume variation as a function of the Ni^{2+}doping for samples synthesized by means of the two used processes can be observed.

Figure 3-2: Variation of the cell parameters (*a, b/√2, c*) and unit cell volume for $La_{0.7}Ca_{0.3}Mn_{1-x}Ni_xO_3$ (x = 0, 0.02, 0.07, 0.1) samples as a function of Ni^{2+} content synthesized (a) via the combustion solution and (b) standard solid state reaction process.

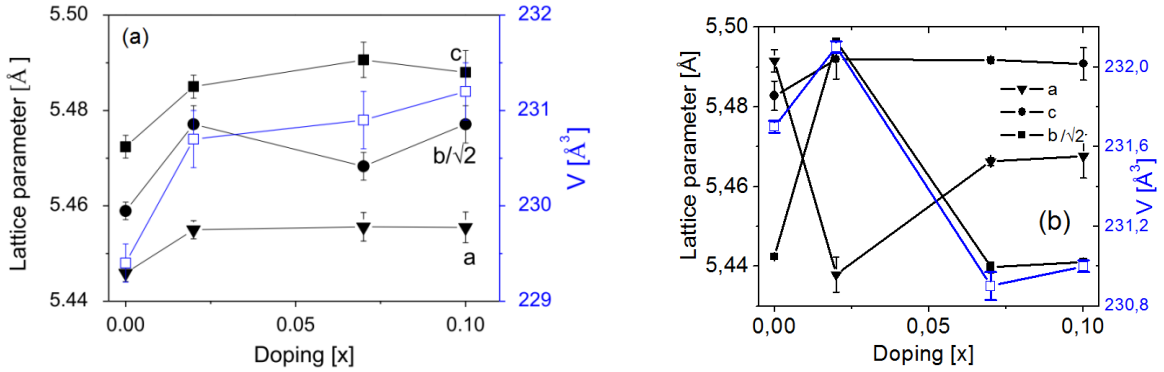

Figure 3-3: (a) variation of the average crystallite size calculated from the Rietveld refinement as a function of the Ni^{2+} content for the samples synthesized by means of the processes: combustion solution and standard solid state reaction. (b) Volume variation as a function of the Ni^{2+}doping for samples synthesized by means of the two used processes.

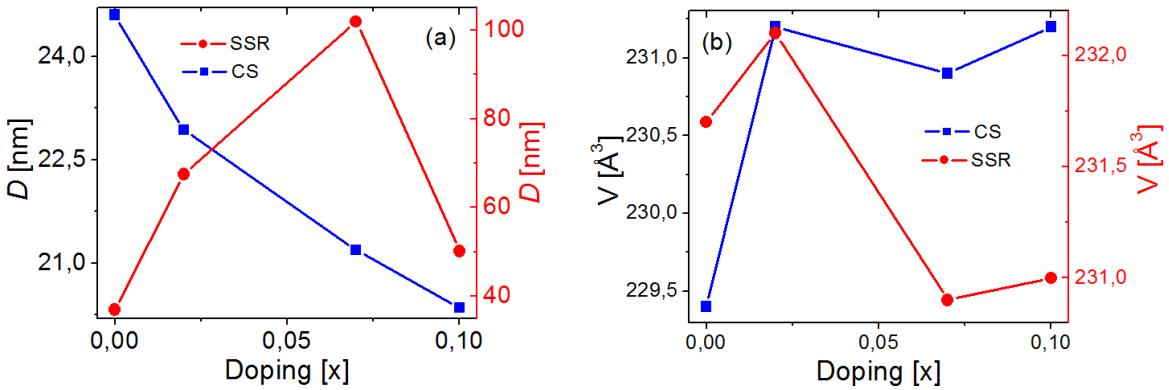

Table 3-1: Lattice parameters, atomic positions, Mn–O bond angle, crystallite size and agreement parameters for $La_{0.7}Ca_{0.3}Mn_{1-x}Ni_xO_3$ (x = 0, 0.02, 0.07, 0.1) samples synthesized by means of auto combustion process resulting from Rietveld refinement of XRD data recorded at room temperature.

$La_{0.7}Ca_{0.3}Mn_{1-x}Ni_xO_3$				
x	**0.00**	**0.02**	**0.07**	**0.10**
a	5.4459	5.4555	5.4556	5.4555
b	7.6971	7.7227	7.7103	7.7227
c	5.4724	5.4880	5.4906	5.4880
V **(A^3)**	229.4	231.2	230.9	231.2
R_F (%)	7.24	8.78	8.80	8.78
χ^2	1.038	1.182	1.399	1.182
Crystallite size (nm)	24.60	22.93	21.19	20.35

Table 3-2: Lattice parameters, atomic positions, Mn–O bond angle, crystallite size and agreement parameters for $La_{0.7}Ca_{0.3}Mn_{1-x}Ni_xO_3$ (x = 0, 0.02, 0.07, 0.1) samples synthesized by means of conventional solid state route resulting from Rietveld refinement of XRD data recorded at room temperature.

$La_{0.7}Ca_{0.3}Mn_{1-x}Ni_xO_3$				
x	**0.00**	**0.02**	**0.07**	**0.10**
a	5.4916	5.4379	5.4663	5.4676
b	7.6967	7.7730	7.6929	7.6948
c	5.4828	5.4919	5.4918	5.4908
V **(A^3)**	231.7	232.1	230.9	231.0
R_F (%)	0.2062	0.0913	0.2235	0.1195
χ^2	3.964	2.621	1.307	2.572
Crystallite size (nm)	36.89	67.48	101.93	50.11

3.1.2 Morphology

Figure 3-4 (Upper left) shows the microstructure obtained from FE-SEM equipment and (upper middle) and (upper right) obtained from TEM microscope of the parent $La_{0.7}Ca_{0.3}MnO_3$ (LCMO) sample synthesized by means of combustion solution method. The images show morphology consists of homogenous particles (rounded polyhedrons) with grain boundaries clearly visible. The particles are abundant and almost uniform in size. The average particle size of the sample observed in all micrograph varies between 20 and 30 nm and is in reasonable agreement with the crystallite size obtained from the XRD pattern. The variation in the grain size as well as the grain boundaries will result in variation of the bond angle, which affects the DE interactions. As a consequence, the orbital overlap and the hopping of electrons between Mn ions of different valences are reduced [4-6]. Fig. 3-4 (lower left) shows the microstructure of the parent LCMO sample obtained from FESEM microscope and synthesized by means of conventional solid state route in which it is observed particle agglomerations with different grain sizes. The eye line projection of the equipment for this magnification estimates 42.8 μm values for the average agglomerate size. Fig. 3-4 (lower middle and lower right) shows more defined particle morphologies obtained from HR-FESEM microscope. The morphology of the compound consists of homogenous grains (rounded polyhedrons) with boundaries clearly visible. The grains are abundant and almost in the order of hundredth of nanometer size and is in reasonable agreement with the crystallite size obtained from the XRD patterns.

Figure 3-4: (Upper left) FE-SEM image, (upper middle) and (upper right) TEM image of the pristine LCMO sample from combustion solution process. (Lower left) FESEM image, (lower middle) and (lower right) HR-FESEM image at different magnification scales of the pristine $La_{0.7}Ca_{0.3}Mn_{1-x}Ni_xO_3$ (x = 0) sample synthesized by standard solid state reaction method.

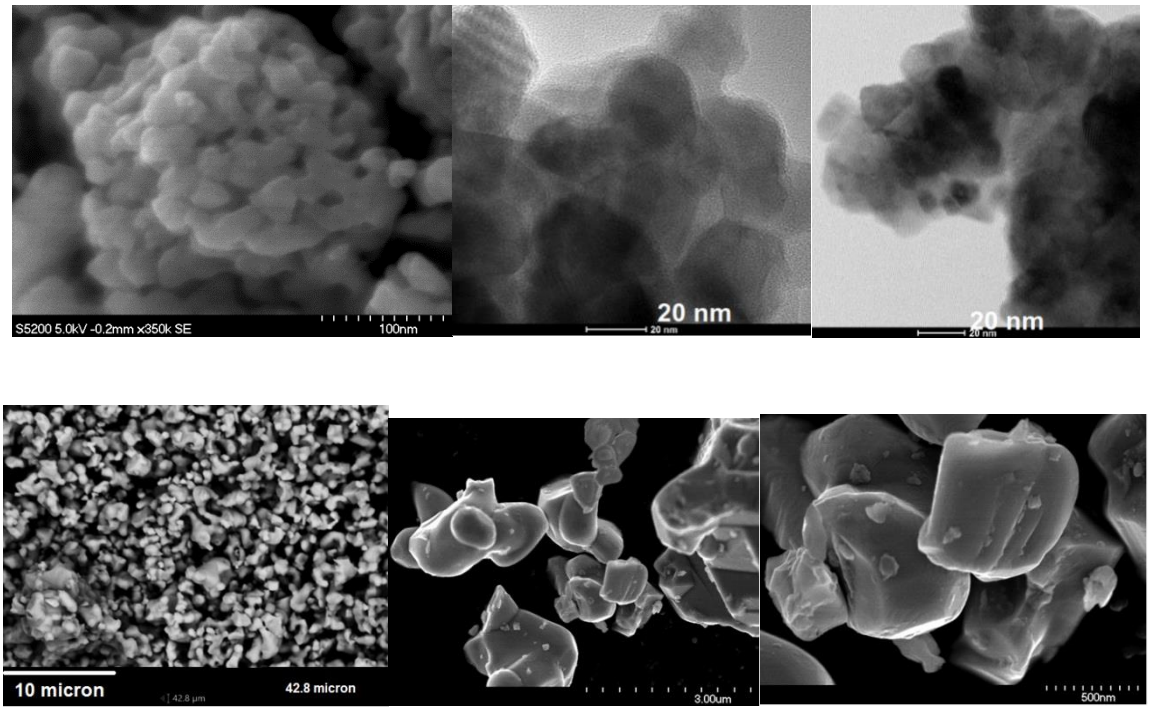

3.1.3 Magnetic properties

To study the magnetic behavior and the influence of the Ni^{2+}-doping on the magnetic and magnetocaloric properties of the $La_{0.7}Ca_{0.3}Mn_{1-x}Ni_xO_3$ samples, several curves such as magnetization versus temperature at different magnetic field strength (*M(H) vs T*) and magnetization versus magnetic field strength at different temperatures (*M(T) vs H*) were recorded at smalls discrete fields and temperature intervals ΔT = 5 K. The change in the magnetic properties of the $La_{0.7}Ca_{0.3}Mn_{1-x}Ni_xO_3$ system is discussed, taking into account factors represented by a change in magnetic interactions such as the ferromagnetic DE interactions (Mn^{3+}–O–Mn^{4+}) or a change in the internal structure [28]. Fig. 3-5 (a) shows the temperature dependence of the field-cooled (FC) magnetization, *M(T),* for $La_{0.7}Ca_{0.3}Mn_{1-x}Ni_xO_3$ (x = 0, 0.02, 0.07, 0.1) samples under 0.1 T applied field synthesized by means of two different processes: combustion solution (CS, reported in Ref. [21]) and solid state reaction (SSR). It can be seen in Fig. 3-5 (a) that all samples synthesized by CS show a smooth (broadening) magnetic transition from paramagnetic (PM) to ferromagnetic (FM) state as *T* decrease near to the Curie temperature (T_C), as well as, the T_C value is systematically reduced from 260 to 180 K for x = 0 and x = 0.1,

respectively, with increasing Ni^{2+}doping level, it which can be seen more in detail in Fig. 3-5 (b). In addition, it can be seen in Fig. 3-5 (a) that the samples synthesized by SSR show a more sharped PM–FM transition as *T* decrease near to the Curie temperature (T_C), as well as, the T_C value is systematically reduced from 268 to 186 K for x = 0 and x = 0.1, respectively, with increasing Ni^{2+}doping level. On the basis of the double exchange (DE) mechanism, the partial substitution on Mn^{3+} ions by Ni^{2+} disturbs the Mn^{3+}–O–Mn^{4+} chains, which leads to a change in the Mn^{3+}/Mn^{4+} ratio [4-9]. As a consequence of this variation, the DE is weakened, and therefore the T_C and the magnetic moment will decrease. In addition, the competition between FM and AFM exchange interactions is reinforced [4-10]. Particularly, the AFM interaction between different Mn–Mn, Mn–Ni, and Ni–Ni pairs is increased due to the increase in Mn^{4+} caused by the appearance of Ni^{2+} ions in the $La_{0.7}Ca_{0.3}MnO_3$ lattice [4-11]. More precisely, the substitution of Mn^{3+} by Ni^{2+} ions can reduce the number of available hopping sites and create cuts in the conduction path, which weakens the DE interaction. Here, primarily it should be taken into account that the FM Ni^{2+}–O–Mn^{4+} exchange interaction may increase the T_C value [4-12]. In turn, due to a parallel arrangement between the Ni and Mn ion spins, the AFM Ni^{2+} ($e_g^{2/3}$)–O–Mn^{3+} (e_g^1) superexchange interaction may enhance the exchange energy of the e_g^{g1} spin, which could impede an e_g electron from hopping to the Mn^{4+} sites surrounding the Ni^{2+} ion [4-13]. Thus the number of available hopping sites is reduced, and the Mn^{3+}–O–Mn^{4+} DE interaction is suppressed. So although the issue of determining the charge distribution and exchange interactions in the Ni-doped manganites is far from being trivial, it is apparent that Ni^{2+} suppresses DE because this ion does not participate in the DE mechanism. As state above, new AFM bonds such as Mn^{3+}–O–Ni^{2+}, Mn^{4+}–O–Mn^{4+}, and Ni^{2+}–O–Ni^{2+}, generated upon Ni^{2+} doping, are non-DE interactions and therefore promote AFM coupling [4-14]. The promotion of AFM coupling then weakens the DE and lowers the T_C [4-15, 4-16]. The AFM bonds may increase in number, with higher Ni^{2+} doping levels leading to a systematic decrease in T_C value, as can be seen in Fig. 3-5 (a) for samples synthesized by means of the two mentioned processes. In Fig. 3-5 (b) it can be seen that the T_C, estimated from the minima in the derivative of magnetization with temperature (*dM/dT vs. T*) curve, is systematically reduced for samples synthesized by means of both routes, but the broadening of the transition is decreased with increasing Ni^{2+}-doping levels for samples obtained by SSR.

Figure 3-5: (a) Temperature dependence of the field-cooled magnetization recorded at 0.1 T magnetic field for $La_{0.7}Ca_{0.3}Mn_{1-x}Ni_xO_3$ (x = 0, 0.02, 0.07, 0.1) samples by combustion solution and solid state reaction processes. (b) *dM/dT* versus *T* curves for the samples plotted in (a). (c) Variation of the highest magnetization (M_S) with the Ni^{2+}-concentration for $La_{0.7}Ca_{0.3}Mn_{1-x}Ni_xO_3$ (x = 0, 0.02, 0.07, 0.1) samples by two different synthesis routes and recorded at *T* = 50 K and *H* = 1.5 T.

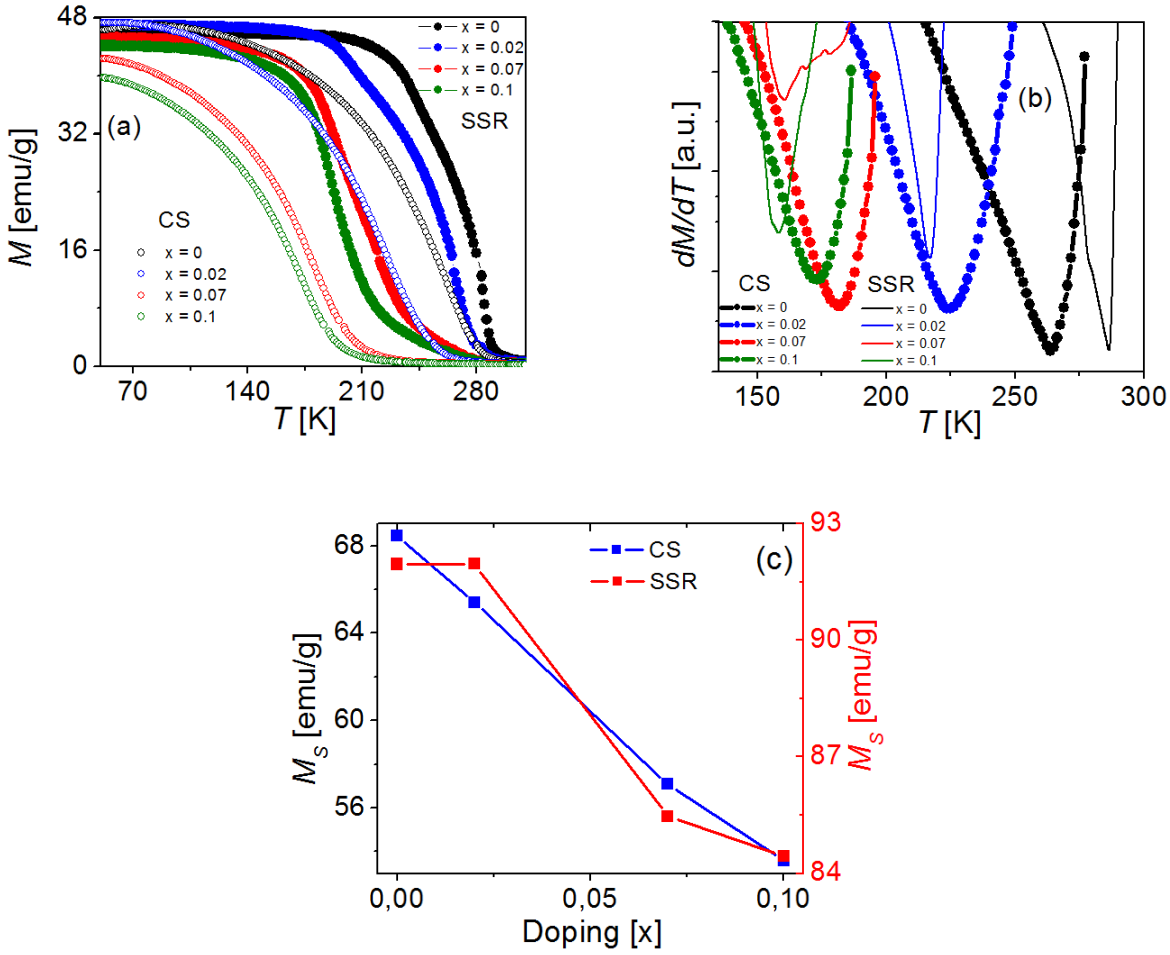

Fig. 3-5 (c) shows the variation in the saturation magnetization (M_S) values as a function of Ni^{2+} content for $La_{0.7}Ca_{0.3}Mn_{1-x}Ni_xO_3$ (x = 0, 0.02, 0.07, 0.1) samples obtained by auto combustion method and conventional route under 0.1 T applied magnetic field and recorded at 50 K. In this plot is observed that the magnitude of magnetization tends to have a more linear decrease with increasing Ni^{2+} content for the samples synthesized by

means of CS than the others one obtained by SSR. This decrease is due primarily to the thermal agitation, which disrupts the arrangement of the magnetic moments.

The role of the internal structure in the change of the magnetic properties of Ni-doped manganites can be visualized through the gradual increase in the orthorhombic distortion due to the Jahn-Teller effect, which stabilizes charge ordering in competition with ferromagnetism [34]. Indeed, doping at the Mn-site can induce a change in the angle (θ) of the Mn ions [35]. In short, deviation of 180° of the Mn–O–Mn angle increase the distortion and decreases the transfer integral $t = t_0 cos(\theta/2)$ (where t_0 is the maximum value of t), which in turn decrease the DE between Mn ions. Nevertheless, it should be pointed out that at low Ni-doping levels, the structural changes are small as suggested by the structural parameters summarized in Table 3-1 and Table 3-2.

Figure 3-6 (a) and (b) shows the dependence of the inverse DC magnetic susceptibility, [$\chi^{-1}(T)$], on the temperature under H = 0.1 T for the LCMO samples discussed in Fig. 3-5. The $\chi^{-1}(T)$ dependence of all samples varies linearly with T in the high-temperature range, indicating Curie-Weiss behavior [$\chi^{-1}(T) = (T - \theta_P)/C$]. No definite downturn in the magnetic susceptibility after the T_C can be observed, which would be an indication of the presence of a Griffiths phase [36]. A Griffiths phase implies the presence of short-range FM correlation well above the T_C. This phenomenon is due to the increase in the magnetic moment arising from the growth of FM spin clusters in the PM region in the temperature range $T_C < T < T_G$ [37]. The temperature T_G is defined as the point at which $\chi^{-1}(T)$ deviates from the Curie-Weiss law. By fitting the linear paramagnetic region of the data, the Curie-Weiss parameters C and θ_P were obtained (Table 3-3). The positive θ_P value confirms the presence of ferromagnetic interaction between spins. Moreover, the significant θ_P decrease upon an increase in the Ni^{2+} content points to a weakening of the DE interactions, which is associated with the decrease in the T_C value. The experimental effective moment μ_{eff}^{exp} can be evaluated using the following relation: $C = \frac{N_A}{3k_B}(\mu_{eff}^{exp})^2$. In turn, the theoretical effective paramagnetic moment μ_{eff}^{theo} is expressed as:

$\mu_{eff}^{theo} = \sqrt{0.7\mu_{eff}^2(Mn^{3+}) + (0.3 - x)\mu_{eff}^2(Mn^{4+})}$ [38], the results for μ_{eff}^{exp} and μ_{eff}^{theo} are listed in Table 3-3.

Figure 3-6: $\chi^{-1}(T)$ dependence for $La_{0.7}Ca_{0.3}Mn_{1-x}Ni_xO_3$ (x = 0, 0.02, 0.07, 0.1) samples at H = 0.1 T synthesized by means of (a) combustion solution and (b) standard solid state reaction process. The straight lines correspond to the Curie–Weiss law fit to the susceptibility data above T_C.

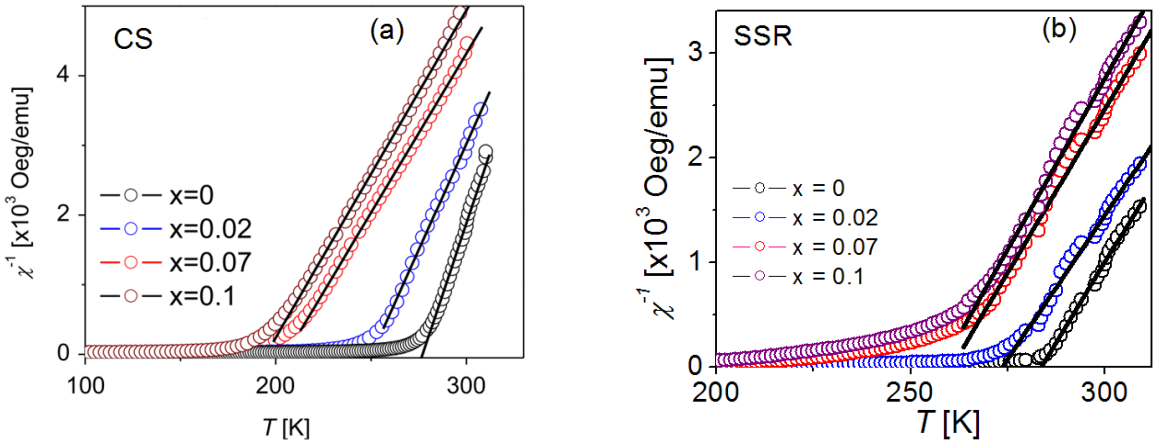

Table 3-3: Magnetic data for $La_{0.7}Ca_{0.3}Mn_{1-x}Ni_xO_3$ samples with x varying between 0 and 0.1. T_C, C, θ_P, μ_{eff}^{exp}, and μ_{eff}^{theo} refer to the Curie temperature, the Curie constant, the Weiss temperature, the experimental and theoretical effective paramagnetic moment, respectively.

x	0.00		0.02		0.07		0.10	
Process	**CS**	**SSR**	**CS**	**SSR**	**CS**	**SSR**	**CS**	**SSR**
T_C **[K]**	264	268	225	253	182	202	174	185
C [emuK/Oe g]	0.0122	0.0163	0.0164	0.0182	0.0218	0.0160	0.0216	0.0153
θ_p **[K]**	276	284	250	274	205	260	198	258
μ_{eff}^{exp} **[μ_B]**	4.51	5.26	5.23	5.56	6.03	5.25	6.01	5.10
μ_{eff}^{theo} **[μ_B]**	4.61		4.58		4.51		4.46	

It can be seen from the results summarized in Table 3-3 that μ_{eff}^{exp} increases upon Ni^{2+} doping for samples synthesized by means of auto combustion method. This unusual behavior is not in a manner consistent with the behavior of the T_C. Nevertheless, this behavior can be explained by invoking the difference in the limits of strength of the FM–DE interactions between Mn^{3+} y Mn^{4+} [39]. In this regard, it has been demonstrated that low Ni-doping levels at Mn sites can induce drastic changes in the physical properties of

manganites, due not only to the effect of the ratio of Mn^{3+}/Mn^{4+} but to the capability of Ni ions to form ferromagnetic regions in a non-FM insulating matrix [40, 41]. The unclear evidence of the presence of a Griffiths phase in the $\chi^{-1}(T)$ curves would suggest that this scenario is not suitable for interpreting the increased effective paramagnetic moment upon Ni^{2+} doping in the samples obtained by means of combustion solution process. In many papers, it has been demonstrated that the reduction in particle size has a direct consequence on the magnetic properties of novel oxides [34–37]. The existence of a surface layer, so-called magnetically dead layer, due to a non-collinear spin arrangement at the surface of crystallites was first postulated in Ref. [38]. The thickness of this surface layer increases when reducing the particle size and consequently the saturation magnetization M_S decreases [38] as observed in Fig. 3-5 (c). A discrimination core/surface was then suggested, where the magnetic coupling in surface is lower than that expected in the core. As a result, the transition is enlarged and the overall T_C reduced [34]. The reduction of magnetization and T_C upon an increase in the Ni^{2+} content is in good agreement with the reduction of the average grain size of the Ni^{2+}-doped LCMO samples synthesized by means of combustion solution route. Thus, it is apparent that the role of a nonmagnetic surface layer becomes more relevant as the average grain decreases [21]. Fig. 3-7 shows the increased effective paramagnetic moment upon Ni^{2+} doping for LCMO samples synthesized by CS and SSR processes and the decreasing crystallite size as a function of Ni^{2+} content for the samples obtained by means of CS method.

Figure 3-7: Variation of μ_{eff}^{exp} and crystallite size with the Ni^{2+}-doping for $La_{0.7}Ca_{0.3}Mn_{1-x}Ni_xO_3$ (x = 0, 0.02, 0.07, 0.1) samples synthesized by means of CS and SSR.

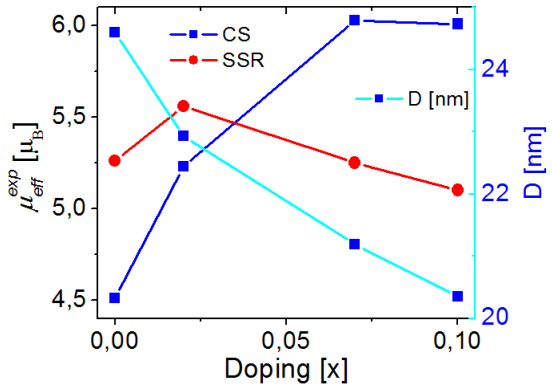

3.1.4 MCE

In order to evaluate the magnetic entropy change in the studied system, isothermal magnetization versus field, *M(H)*, curves were recorded at different temperatures around the T_C in H = 0 – 1.5 T field range for each sample. Fig. 3-8 y Fig. 3-9 left panels shows the dependence of the magnetization on the applied magnetic field recorded at different temperatures, from 0 to 1.5 T, for $La_{0.7}Ca_{0.3}Mn_{1-x}Ni_xO_3$ (x = 0, 0.02, 0.07, 0.1) samples obtained by means of combustion solution and conventional solid state processes, respectively. The *M(H)* curves indicate that the samples magnetization increases rapidly at low fields and then tends to saturate at higher fields, which reflects the magnetic behavior of LCMO material. This decrease is mainly due to the thermal agitation, which disrupts the arrangement of the magnetic moments. The nonlinear *M(H)* curves in the FM region become linear in the PM region. The nature of the magnetic phase transition in $La_{0.7}Ca_{0.3}Mn_{1-x}Ni_xO_3$ samples can be determined from the Arrot plots (M^2 *vs* *H/M*) curves (converted from the isothermal *M–H* data) using the Banerjee Criterion [44]. The plots resulting of this analysis are presented in Fig. 3-8 and Fig. 3-9 right panels for LCMO samples synthesized by means of CS and SSR, respectively.

Figure 3-8: Left panels: Magnetization versus magnetic field *M(H)* recorded around T_C, and right panels: Arrot plots isotherms of M^2 *vs* *H/M* at different temperatures for $La_{0.7}Ca_{0.3}Mn_{1-x}Ni_xO_3$ (x = 0, 0.02, 0.07, 0.1) samples obtained by means of CS method.

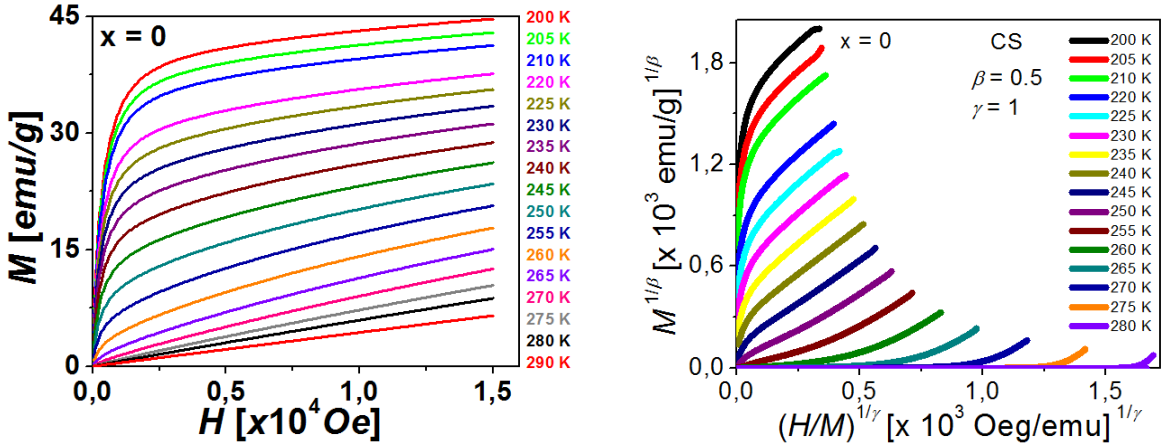

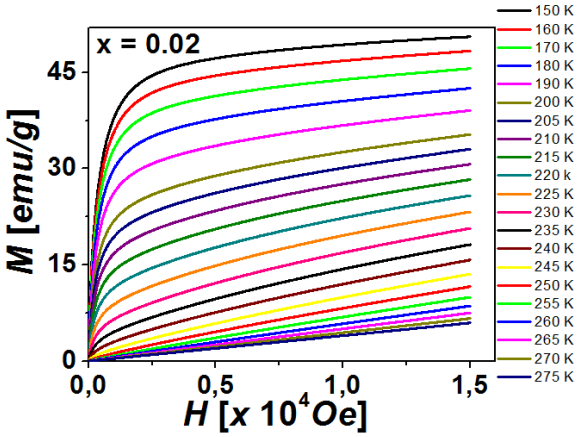
x = 0.02
M [emu/g]
H [x 10^4 Oe]
150 K
160 K
170 K
180 K
190 K
200 K
205 K
210 K
215 K
220 k
225 K
230 K
235 K
240 K
245 K
250 K
255 K
260 K
265 K
270 K
275 K

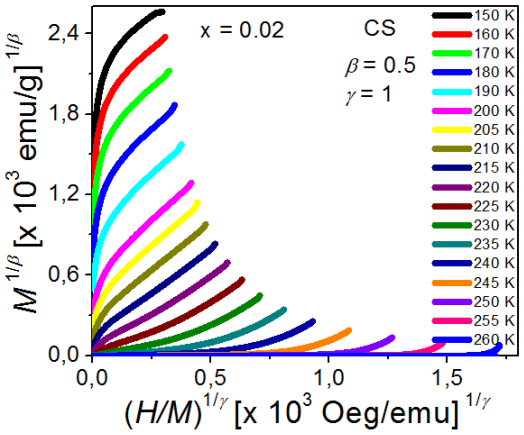
x = 0.02
CS
β = 0.5
γ = 1
M^1/β [x 10^3 emu/g]^1/β
(H/M)^1/γ [x 10^3 Oeg/emu]^1/γ
150 K
160 K
170 K
180 K
190 K
200 K
205 K
210 K
215 K
220 K
225 K
230 K
235 K
240 K
245 K
250 K
255 K
260 K

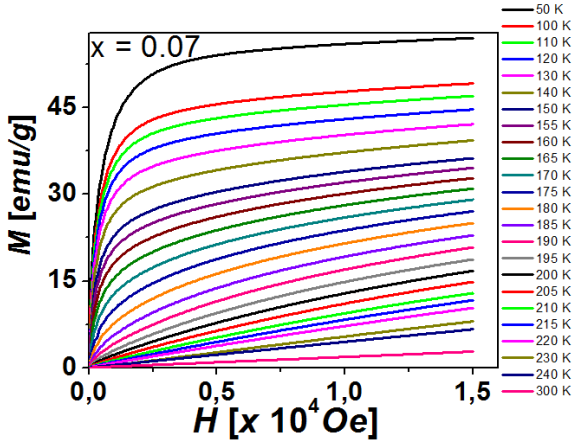
x = 0.07
M [emu/g]
H [x 10^4 Oe]
50 K
100 K
110 K
120 K
130 K
140 K
150 K
155 K
160 K
165 K
170 K
175 K
180 K
185 K
190 K
195 K
200 K
205 K
210 K
215 K
220 K
230 K
240 K
300 K

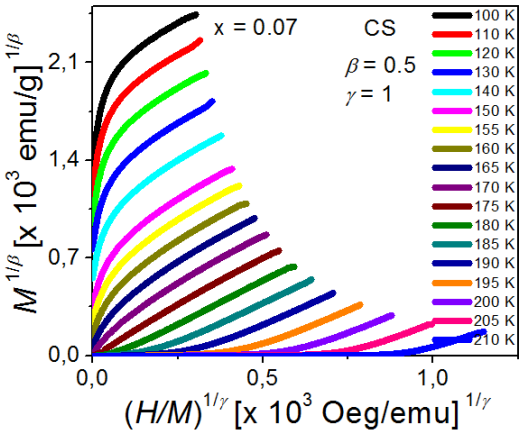
x = 0.07
CS
β = 0.5
γ = 1
M^1/β [x 10^3 emu/g]^1/β
(H/M)^1/γ [x 10^3 Oeg/emu]^1/γ
100 K
110 K
120 K
130 K
140 K
150 K
155 K
160 K
165 K
170 K
175 K
180 K
185 K
190 K
195 K
200 K
205 K
210 K

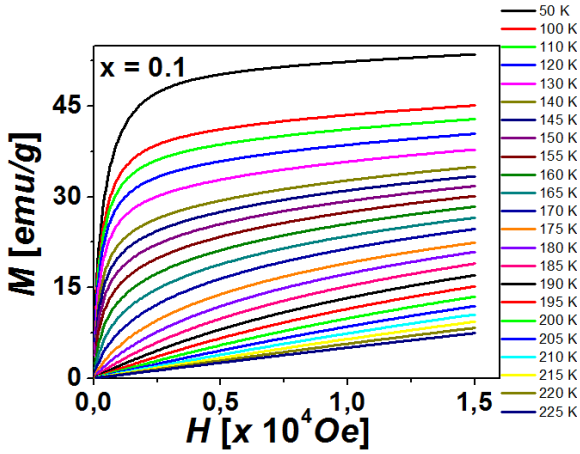
x = 0.1
M [emu/g]
H [x 10^4 Oe]
50 K
100 K
110 K
120 K
130 K
140 K
145 K
150 K
155 K
160 K
165 K
170 K
175 K
180 K
185 K
190 K
195 K
200 K
205 K
210 K
215 K
220 K
225 K

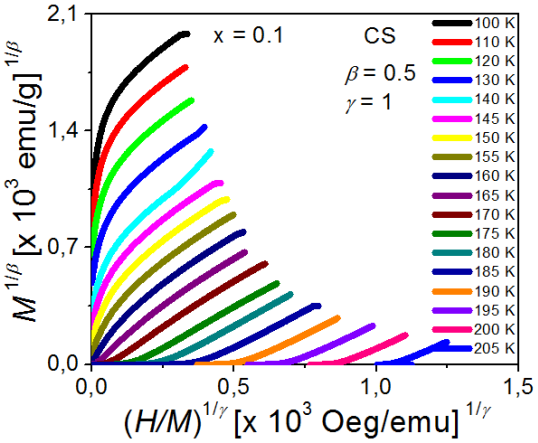
x = 0.1
CS
β = 0.5
γ = 1
M^1/β [x 10^3 emu/g]^1/β
(H/M)^1/γ [x 10^3 Oeg/emu]^1/γ
100 K
110 K
120 K
130 K
140 K
145 K
150 K
155 K
160 K
165 K
170 K
175 K
180 K
185 K
190 K
195 K
200 K
205 K

Figure 3-9: Left panels: Magnetization versus magnetic field *M(H)* recorded around T_C, and right panels: Arrot plots isotherms of M^2 *vs* *H/M* at different temperatures for $La_{0.7}Ca_{0.3}Mn_{1-x}Ni_xO_3$ (x = 0, 0.02, 0.07, 0.1) samples obtained by means of SSR process.

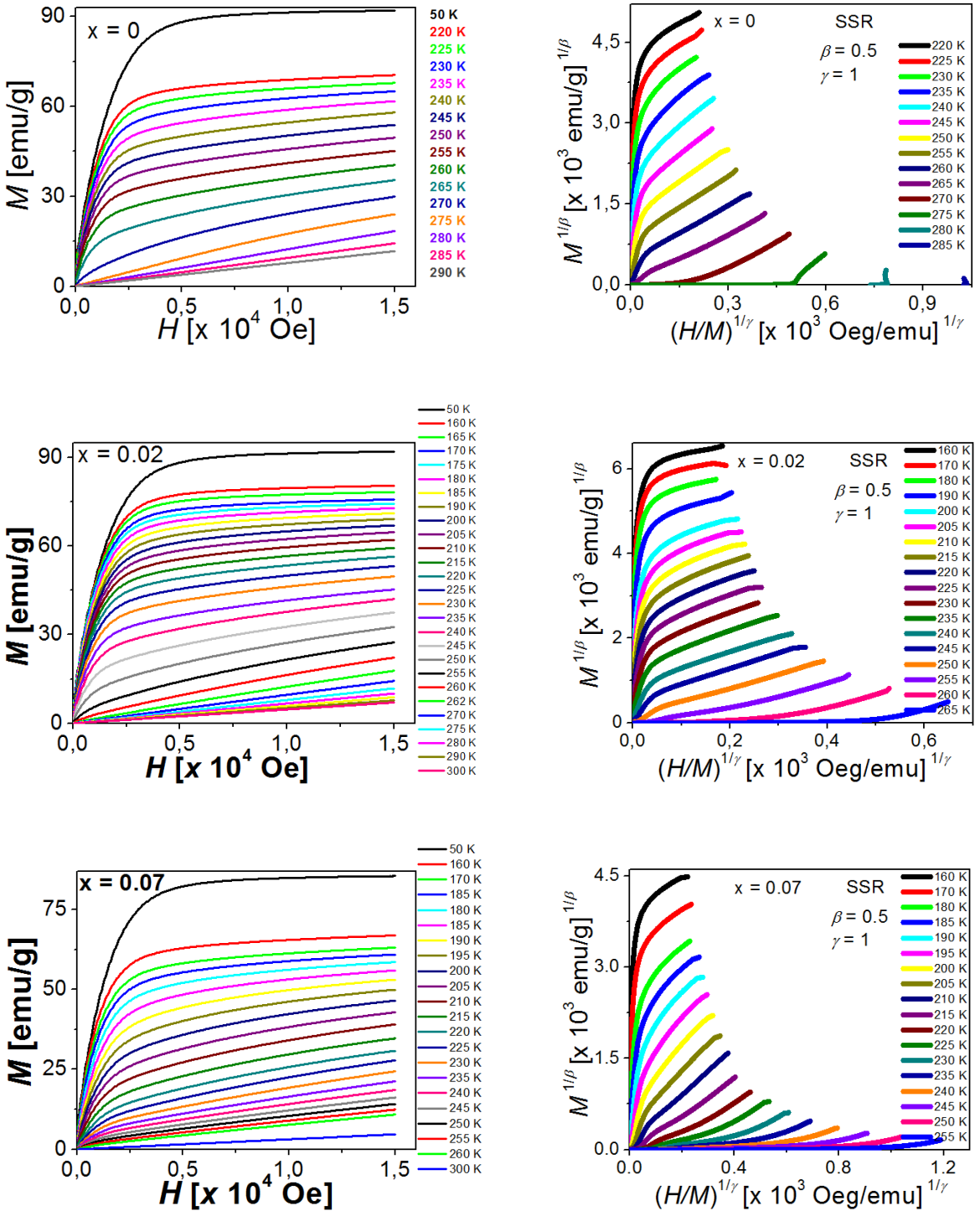

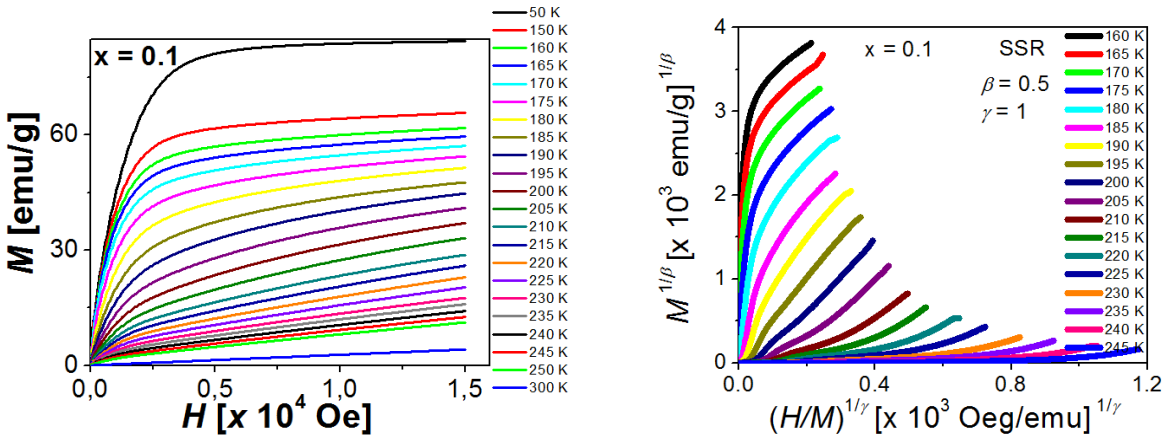

According to the Banerjee criterion, the magnetic transition is second-order if all the M^2 *vs* H/M curves have a positive slope [45]. On the other hand, if some of the M^2 *vs* H/M curves show a negative slope at some point, the transition is first-order [46]. In Fig. 3-9 right panel for $La_{0.7}Ca_{0.3}Mn_{1-x}Ni_xO_3$ sample with x = 0, apparently a negative slope is presented for this sample, but an enlarged scale (zoom) in this area confirms that the magnetic transition order it still is of second-order (inset of Fig. 3-9 right panel for LCMO x = 0 sample). The entire curves exhibit, near the T_C, a positive slope indicating that the PM–FM phase transition is second-order according to Banerjee criteria [40]. Although most mixed-valence manganites such as $La_{0.7}Ca_{0.3}MnO_3$ are associated with the first-order character of the magnetic transition [41], changes of the magnetic phase transition order can be induced when the particle size is brought down from bulk to a few tens of nanometer range [42]. In this case there will be a large number of spins on the surface of nanoparticles that are generally expected to be disordered and will lead to destruction of any spin order [43]. This so called core/shell morphology model predicts that the disordered outer layer is more likely to undergo a second-order transition, from the disordered state into the paramagnetic one [44]. In this way, it is very probably that the observed second-order phase transition in the parent LCMO sample is linked to the effects of the downsizing of the particle.

The temperature dependence of the magnetic entropy change ($-\Delta S_M$) for $La_{0.7}Ca_{0.3}Mn_{1-x}Ni_xO_3$ (x = 0, 0.02, 0.07, 0.1) samples synthesized by means of combustion solution and solid state reaction processes, recorded at magnetic field strengths varying between 0.25 and 1.5 T are plotted in Fig. 3-10 and Fig. 3-11, respectively. The calculated

magnetocaloric properties for the samples in Fig. 3-10 and Fig. 3-11 under 0.5, 1.0 and 1.5 applied magnetic fields are listed in Table 3-4.

Figure 3-10: Temperature dependence of the magnetic entropy change for $La_{0.7}Ca_{0.3}Mn_{1-x}Ni_xO_3$ (x = 0, 0.02, 0.07, 0.1) samples synthesized by means of combustion solution process recorded at magnetic field strengths varying between 0.25 and 1.5 T.

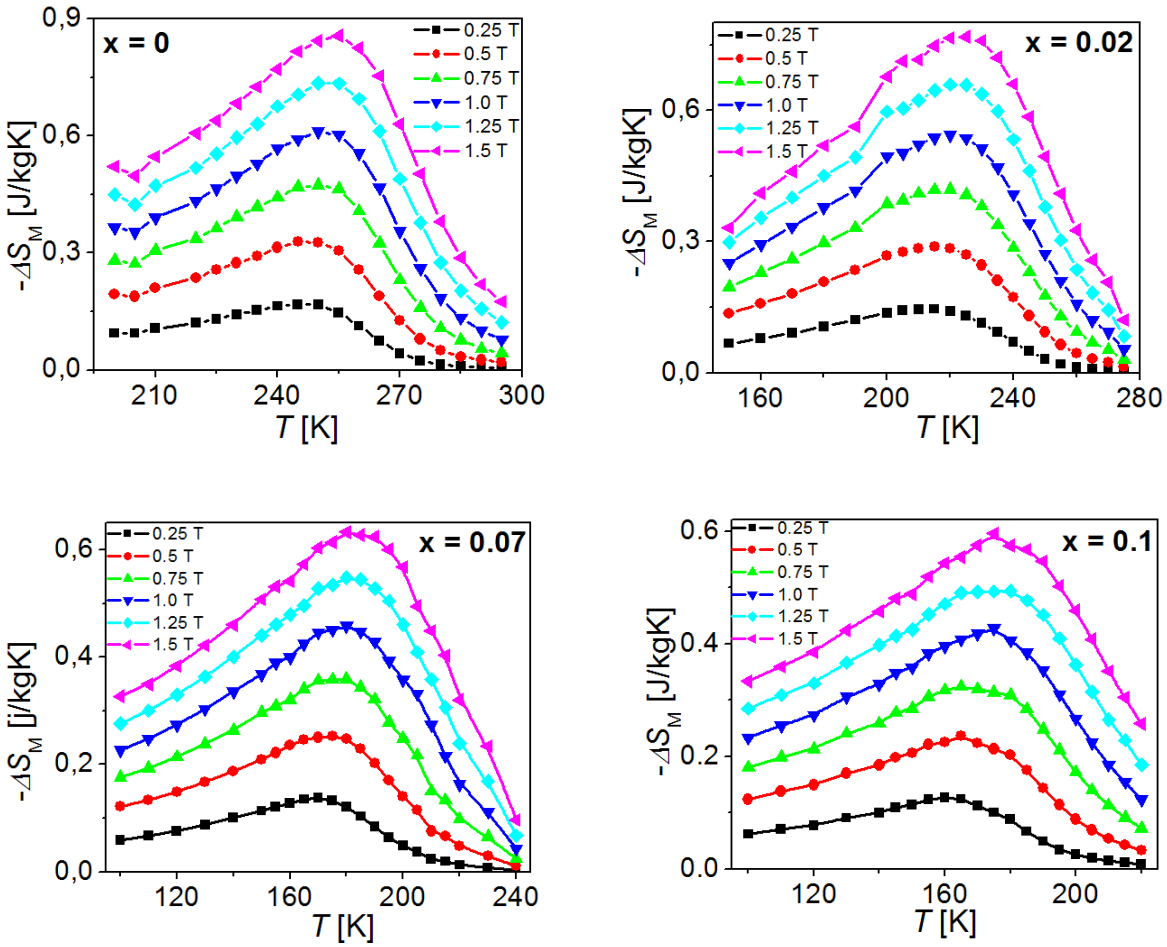

Figure 3-11: Temperature dependence of the magnetic entropy change for $La_{0.7}Ca_{0.3}Mn_{1-x}Ni_xO_3$ (x = 0, 0.02, 0.07, 0.1) samples synthesized by means of conventional solid state reaction process recorded at magnetic field strengths varying between 0.25 and 1.5 T.

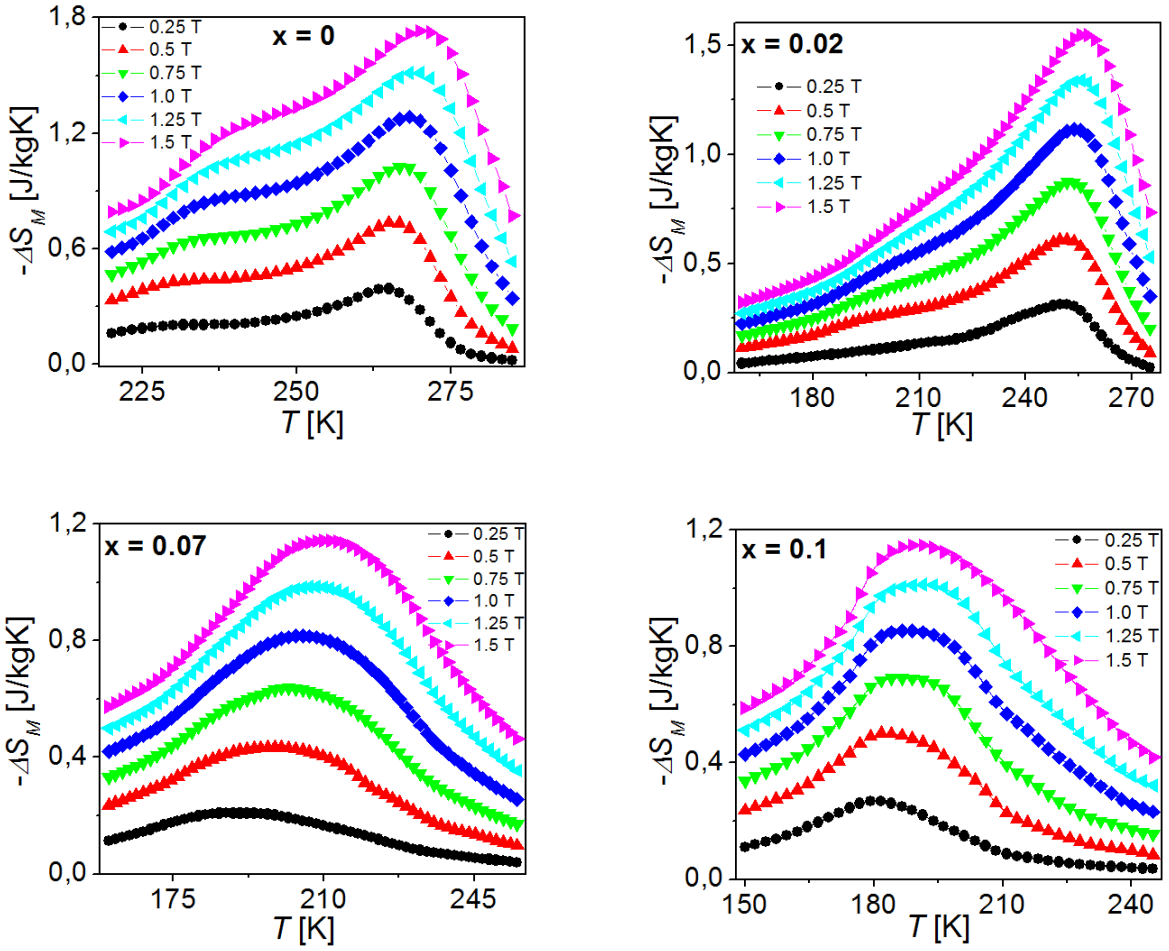

The magnetocaloric properties of $La_{0.7}Ca_{0.3}Mn_{1-x}Ni_xO_3$ samples with x = 0, 0.02, 0.07 and 0.1 synthesized by means of auto-combustion and conventional route under 0.5, 1.0 and 1.5 applied magnetic fields are listed in Table 3-4. It is evident that $-\Delta S_M$ increase with an increasing magnetic fields and the $-\Delta S_{M,máx}$ is shifted towards higher temperature for all the composition and for the two processes. It is also clear that the largest $-\Delta S_M$ occurs near the T_C, which is a property of simple ferromagnets, due to the efficient ordering of magnetic moments induced by the magnetic field at the ordering temperature [4-43]. The maximum magnetic entropy change value observed for the x = 0, 0.02, 0.07 and 0.1 compositions are 0.86 (1.73), 0.77 (1.55), 0.63 (1.14) and 0.60 (1.15) J/kgK, for samples synthesized by combustion solution and solid state reaction (in brackets) process respectively, under 1.5 T magnetic field. The $-\Delta S_M$ value for the un-doped sample obtained by means of combustion solution is in a good agreement with that reported in Ref. [4-26], in which LCMO particles with ≈ 15 nm mean diameter were obtained by the

authors using the sol-gel method. Nevertheless, it should be mentioned that in nanocrystalline samples, the sensitive dependence of the MCE on synthesis details becomes even more evident. Thus the difference in the $-\Delta S_M$ values of more than an order of magnitude can be found in the literature for similarly-sized particles subject to a comparable field change [4-26, 4-38].

Table 3-4: Summary of magnetocaloric properties of $La_{0.7}Ca_{0.3}Mn_{1-x}Ni_xO_3$ (x = 0, 0.02, 0.07, 0.1) samples at three different magnetic field strengths synthesized by means of the combustion solution and standard solid state reaction processes.

Ni-doping level (x)	H [T]	$-\Delta S_M$ [J/kgK]		δT_{FWHM} [K]		RCP [J/kg]	
Process		**CS**	**SSR**	**CS**	**SSR**	**CS**	**SSR**
0.00	**0.5**	0.329	0.7347	37.51	15.05	12.34	11.06
	1.0	0.612	1.2847	37.82	16.78	23.15	21.56
	1.5	0.858	1.7308	37.70	17.21	32.34	29.79
0.02	**0.5**	0.289	0.6095	77.28	26.92	22.34	16.41
	1.0	0.544	1.1143	77.27	28.30	42.04	31.53
	1.5	0.771	1.5457	77.31	28.36	**59.60**	43.84
0.07	**0.5**	0.253	0.4349	83.28	41.37	21.07	17.99
	1.0	0.458	0.8170	83.27	43.40	38.14	35.46
	1.5	0.633	1.1443	83.27	41.86	52.71	**47.90**
0.10	**0.5**	0.236	0.5014	84.51	37.22	19.94	18.66
	1.0	0.428	0.8550	84.51	38.70	36.17	33.09
	1.5	0.596	1.1488	84.51	39.50	50.37	45.38

It can be seen that the $-\Delta S_M$ values for LCMO samples obtained by means of conventional route are the double of those for LCMO samples synthesized by means of combustion solution process, but are in good agreement with their T_C value (listed in Table 3-3) and RCP values, for which the maximum variation were ≈ 9.1 and 19.6 %, respectively. On the other hand the $-\Delta S_M$ and RCP values, for samples processed by means of solid state reaction with x = 0, and x = 0.1 are in good agreement with those reported by S. Hua et al. [27] and C. Krishnamoorthi et al. [25], except to the T_C values, considering that in the

Ref. [25] the solid state reaction process was carried out in several stages, including intermediates ball milling process, to try obtain a grain size reduction, it which cause that the process being more expensive.

Fig. 3-12 and Fig. 3-13 left panels shows the calculated $-\Delta S_M$ values for $La_{0.7}Ca_{0.3}Mn_{1-x}Ni_xO_3$ (x = 0, 0.02, 0.07, 0.1) samples under 1.5 applied magnetic field and processed by means of combustion solution and solid state reaction, in which can be seen the T_C shift toward lower values just as the $-\Delta S_M$ values decrease with increases the Ni^{2+}-doping level. The upper insets of Fig. 3-12 and Fig. 3-13 show the variation of the T_C values as a function of the Ni-doping. In Fig. 3-12 and Fig. 3-13 right panels is observed the dependence of the relative cooling power (RCP) values on the magnetic field for $La_{0.7}Ca_{0.3}Mn_{1-x}Ni_xO_3$ (x = 0, 0.02, 0.07, 0.1) samples obtained by means of combustion and solid state, respectively. In the insets of these respective figures it can be seen the variation of the maximum magnetic entropy change ($\Delta S_{M,max}$) values with the Ni^{+2}-concentration at different magnetic fields for the synthesized samples.

Figure 3-12: Left panel: Temperature dependence of the magnetic entropy change for $La_{0.7}Ca_{0.3}Mn_{1-x}Ni_xO_3$ (x = 0, 0.02, 0.07, 0.1) samples processed by means of combustion solution method under 1.5 T magnetic field. Inset: variation of T_C as a function of Ni^{2+}-doping level for $La_{0.7}Ca_{0.3}Mn_{1-x}Ni_xO_3$ (x = 0, 0.02, 0.07, 0.1) samples in the main panel. Right panel: Dependence of the RCP values on the magnetic field for $La_{0.7}Ca_{0.3}Mn_{1-x}Ni_xO_3$ (x = 0, 0.02, 0.07, 0.1) samples obtained by means of auto-combustion process. Inset: variation of the maximum magnetic entropy change ($\Delta S_{M,max}$) values as a function of the Ni^{+2}-doping at different magnetic fields for the obtained samples in the main panel.

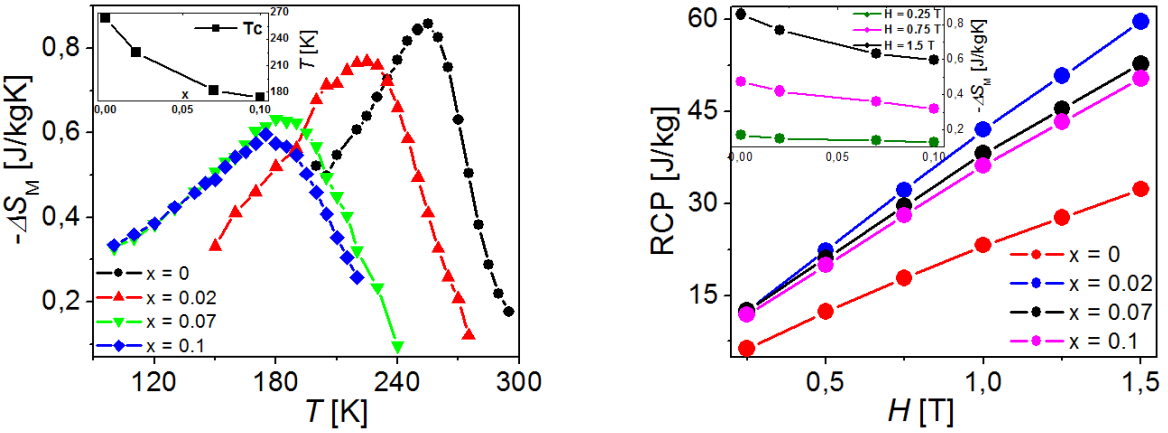

Figure 3-13: Left panel: Temperature dependence of the magnetic entropy change for $La_{0.7}Ca_{0.3}Mn_{1-x}Ni_xO_3$ (x = 0, 0.02, 0.07, 0.1) samples processed by means of standard solid state reaction process under 1.5 T magnetic field. Inset: variation of T_C as a function of Ni^{2+}-doping level for $La_{0.7}Ca_{0.3}Mn_{1-x}Ni_xO_3$ (x = 0, 0.02, 0.07, 0.1) samples in the main panel. Right panel: Dependence of the RCP values on the magnetic field for $La_{0.7}Ca_{0.3}Mn_{1-x}Ni_xO_3$ (x = 0, 0.02, 0.07, 0.1) samples obtained by means of solid state route. Inset: variation of the maximum magnetic entropy change ($\Delta S_{M,max}$) values as a function of the Ni^{+2}-doping at different magnetic fields for the obtained samples in the main panel.

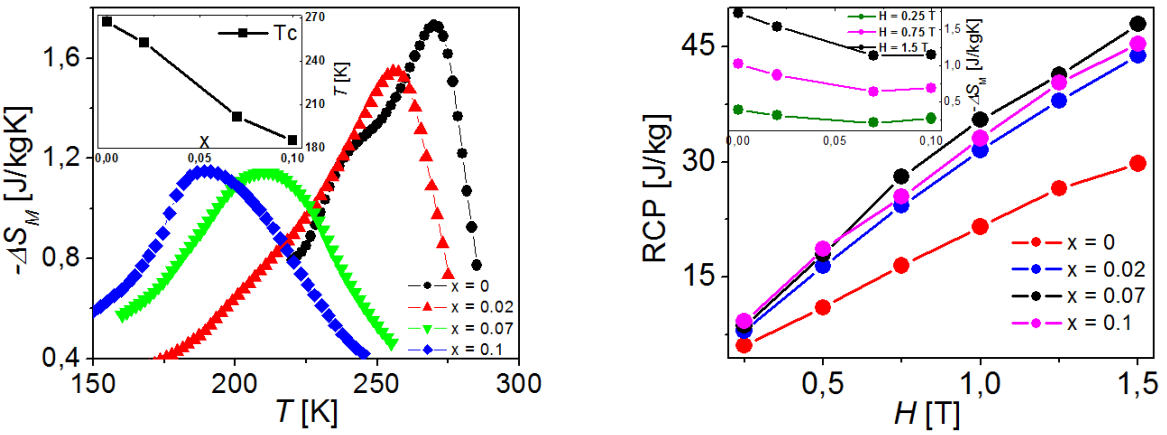

From the RCP calculations, summarized in Table 3-4, it can be seen that the addition of Ni^{2+} increases the RCP value compared to that of the parent LCMO. This is certainly desirable for potential applications of these materials in magnetic refrigeration. In this regard, the LCMO sample with a Ni-doping level as 2 and 7 % synthesized by means of

combustion solution and solid state, respectively, features the highest RCP values (~ 60 and ~ 48 J/kg) around 225 and 202 K at 1.5 T applied magnetic field, respectively. It has been observed of a number of occasions that the reduced maximum value of $-\Delta S_M$, which often accompanies broad magnetic entropy change peaks, can be compensated by the increased width, resulting in an enhanced RCP over sharper transitions [55]. Table 3-4 shows that this scenario holds true for all the $La_{0.7}Ca_{0.3}Mn_{1-x}Ni_xO_3$ (x = 0, 0.02, 0.07, 0.1) samples obtained by means of the two processes used in this investigation. From the results obtained in the present study and by considering those reported in several publications [56], it is possible to assert that the MCE in perovskite manganites is certainly large. In particular, it is demonstrated in the present study that the RCP of the samples with x = 0.02 and x = 0.07 obtained by means of combustion solution and solid state are increased about 84 and 61 % of that of the parent LCMO, respectively. This is certainly a promising result for practical application of manganites in magnetic refrigeration technology over a wide range of temperatures operation. Probably the strong spin-lattice coupling, related to the magnetic ordering process, is the cause of the large MCE found in these challenging oxides [46, 57].

It can also be noted from Fig. 3-12 and Fig. 3-13 that Ni^{2+} doping not only shifts the T_C values towards lower temperatures but also reduce the $\Delta S_{M,máx}$ by a value as low as ~ 30 and ~ 34 % for x = 0.1 in samples processed by means of combustion solution and solid state, respectively. Probably the change in the $-\Delta S_{M,máx}$ values upon Ni^{2+} doping is due to the relatively low strength of the magnetic fields, which is insufficient to achieve a complete saturation of the magnetization in the studied samples. Similar changes in $-\Delta S_{M,máx}$ have been reported for Y-doped manganites and were attributed to the low strength of the magnetic field used to measure the MCE [4-44]. On the other hand, $-\Delta S_{M,máx}$ in manganites remained constant when the samples were measured in magnetic fields $\geq$ 3 T [4-14, 4-45]. Thus the results presented in Fig. 3-12 and Fig. 3-13 concerning the $-\Delta S_{M,máx}$ variation upon Ni^{2+} doping agree with the results reported in Ref. [4-44]. A small variation of the $-\Delta S_{M,máx}$ upon doping can be considered as a plus for magnetic refrigeration applications, because the same material can be used within a wide range of temperatures. In general, the magnetic entropy changes achieved for Ni^{2+}-doped LCMO samples synthesized via combustion solution and solid state reaction processes in this

thesis are higher than those reported for other manganites, *e.g.* $La_{0.7}Sr_{0.3}Mn_{1-x}Ni_xO_3$, with comparable Ni^{2+}-doping levels but synthesized via standard solid-state reaction [4-14].

The ΔS_M can be calculated from the specific heat capacity using the thermodynamic relation $\Delta S_M = \int_0^T \frac{C_P(T,H)-C_P(T,0)}{T} dT$ [4-50]. Hence, the relation $\Delta C_P = C_P(T,H) - C_P(T,0) = T\left(\frac{\partial \Delta S_M}{\partial T}\right)$ allows one to estimate the change of the specific heat ΔC_P induced by the magnetic field variation. Fig. 3-14 (left) and (right) shows the variation of the C_P with the temperature for $La_{0.7}Ca_{0.3}Mn_{1-x}Ni_xO_3$ (x = 0, 0.02, 0.07, 0.1) samples obtained by means of CS and SSR, respectively, recorded at 0.5 T. It can be noted in Fig. 3-14 that the ΔC_P values change from the negative to the positive in the vicinity of T_C for each Ni^{2+}-doping level. Moreover, the minimum value of ΔC_P increases with the applied field and the position shifts to higher temperatures [inset of Fig. 3-14 (left) and (right)]. The behavior of ΔC_P is related with the relative broad PM–FM transition shown by the nanometric $La_{0.7}Ca_{0.3}Mn_{1-x}Ni_xO_3$ samples. The sum of the two parts is the magnetic contribution to the total specific heat, which affects the cooling or heating power of the magnetic refrigerator [4-51]. The appearance of negative C_P values should be carefully interpreted, because negative values for this property do not have physical sense. The issue of having negative C_P values can be tackled by considering that the use of magnetocaloric materials in magnetic solid-state refrigeration requires a high C_P to reduce the oscillations in temperature during the alterations in the transfer of heat flow. Nevertheless, this value should not be too high since this will tend to reduce the adiabatic temperature change (ΔT_{ad}) of a magnetic system when the magnetic field is varied from 0 to H_{max}. Mathematically ΔC_P should differ from zero only in the vicinity of T_C. In this regard, the C_P values are positive before the transition ($T>T_C$) and negative after the transition ($T<T_C$). Since the first derivative $\partial M/\partial T < 0$ around T_C, the basic equation relating S_M and M gives values of $S_M < 0$ and, accordingly, the total entropy decreases upon magnetization. Hence a sharp variation in ΔC_P values is expected at $T = T_C$.

Figure 3-14: (a) Variation of ΔC_P values as a function of temperature at H = 0.5 T for $La_{0.7}Ca_{0.3}Mn_{1-x}Ni_xO_3$ (x = 0, 0.02, 0.07, 0.1) samples. Inset: Temperature dependence of ΔC_P values of the pristine LCMO sample recorded at H = 0.5, 1.0 and 1.5 T. (b) Variation of ΔC_P values as a function of three different magnetic field strengths for $La_{0.7}Ca_{0.3}Mn_{1-}$

$_xNi_xO_3$ (x = 0, 0.02, 0.07, 0.1) samples. Inset: Variation of the T_p values at maximum ΔC_P as a function of Ni^{2+}-concentration.

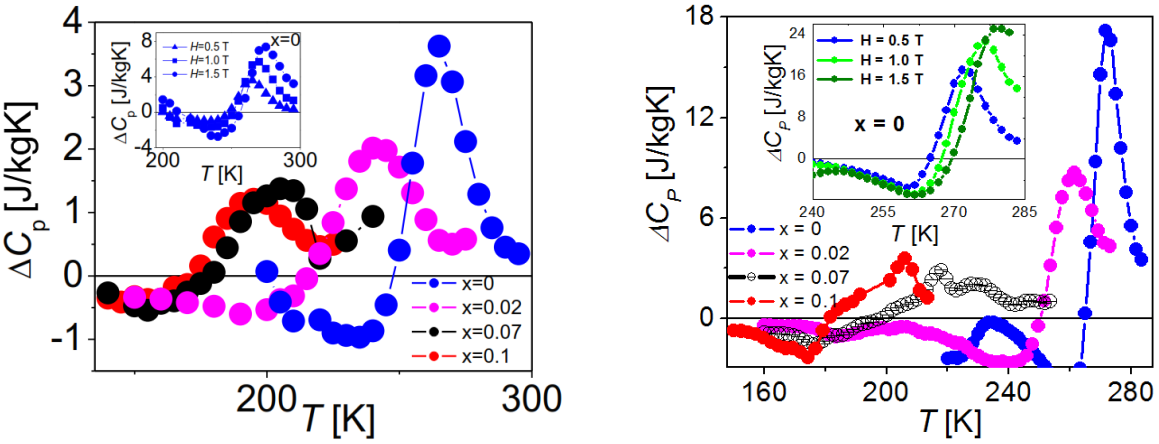

As seen in Fig. 3-8 and Fig. 3-9 right panels, the LCMO samples synthesized by means of the CS and SSR methods show a second-order PM–FM phase transition. In order to understand the field dependence of ΔS_M the magnetocaloric response of a system should be modeled. This can be approached by development first principles models for particular materials. A variety of predictions can be carried out for a particular alloy by means of these models (*e.g.* mean field models). Nevertheless, discrepancies between the predictions of the models and the experimental $\Delta S_M(H)$ data in materials with a second order phase transition has demonstrated that additional model are necessary to explain the $\Delta S_M(H)$ dependence. Fortunately, the existence of a universal curve for the $\Delta S_M(H)$ dependence in materials with a second order phase transition has recently been demonstrated [4-52]. Such curve can be constructed phenomenologically without knowing the critical exponents of the material or its equation of state [4-52]. The universal curve is not restricted to the mean field case. Here, the different $\Delta S_M(T, \Delta H)$ curves recorded at several magnetic fields should collapse into a single master curve with the scaling of the temperature. In order to plot such universal curve, the different $\Delta S_M(T, \Delta H)$ curves should be normalized with respect to their respective $\Delta S_{M,max}$ values. In addition, the temperature axis should be rescaled in a different way below and above T_C as follows: $\theta = \begin{Bmatrix} \frac{-(T-T_C)}{T_{r1}-T_C}, T \leq T_C \\ \frac{(T-T_C)}{T_{r2}-T_C}, T \geq T_C \end{Bmatrix}$ [4-52]. Here, T_{r1} y T_{r2} are reference temperatures corresponding to a

certain fraction $f = \Delta S_{M,}(T_{r1,2}) / \Delta S_{M,max}$. The choice of f (with $0 < f < 1$) does not affect the universal-curve construction. Normalized entropy change curves as a function of the rescaled temperature theta at different applied fields for $La_{0.7}Ca_{0.3}Mn_{1-x}Ni_xO_3$ (x = 0, 0.02, 0.07, 0.1) samples obtained by means of CS and SSR routes are shown in Fig. 3-15 and Fig. 3-16, respectively.

A superposition of the data into a single curve both in the PM region with $\theta > 0$ and FM region with $\theta < 0$ is clearly observed for all the studied samples. The collapse of $\Delta S_M(T, \Delta H)$ into a unique curve, in a wide temperature range, is a confirmation of the general validity of the treatment in the second-order phase transition compounds. Thus, the order of the phase transition of materials can be determined by means of the universal curve. This is especially useful when the purely magnetic Banerjee criterion gives erroneous results.

Furthermore, the universal curve can be used for special purposes, such as making extrapolations of the results up to fields or temperatures not available in the laboratory, enhancing the resolution of the data and de-convoluting the response of overlapping magnetic transitions [4-53].

Figure 3-15: Normalized magnetic entropy change as a function of the rescaled temperature θ for $La_{0.7}Ca_{0.3}Mn_{1-x}Ni_xO_3$ (x = 0, 0.02, 0.07, 0.1) samples synthesized by means of CS process.

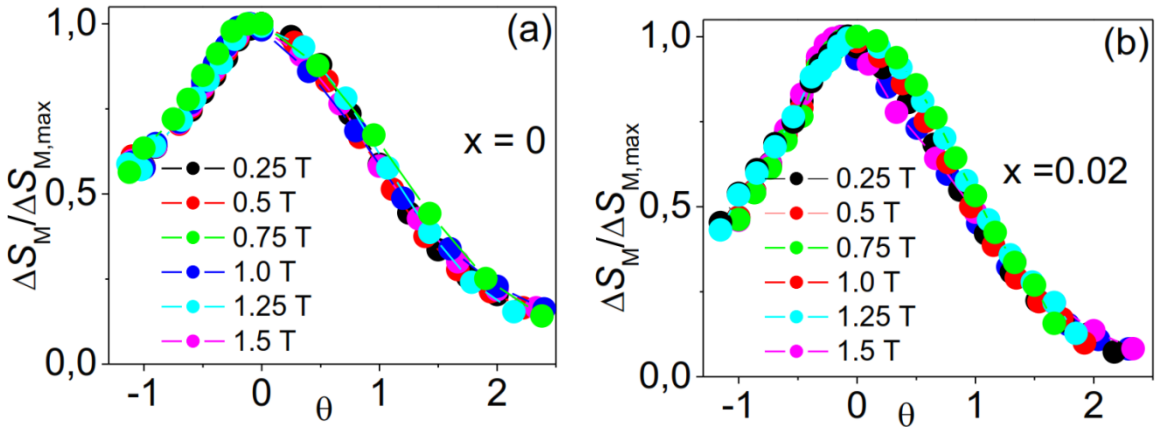

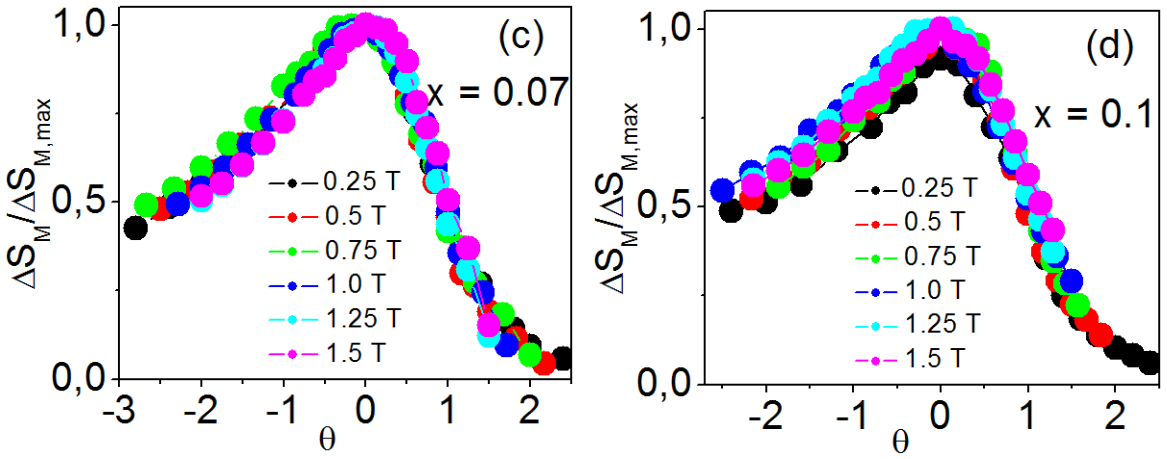

Figure 3-16: Normalized magnetic entropy change as a function of the rescaled temperature θ for $La_{0.7}Ca_{0.3}Mn_{1-x}Ni_xO_3$ (x = 0, 0.02, 0.07, 0.1) samples synthesized by means of SSR process.

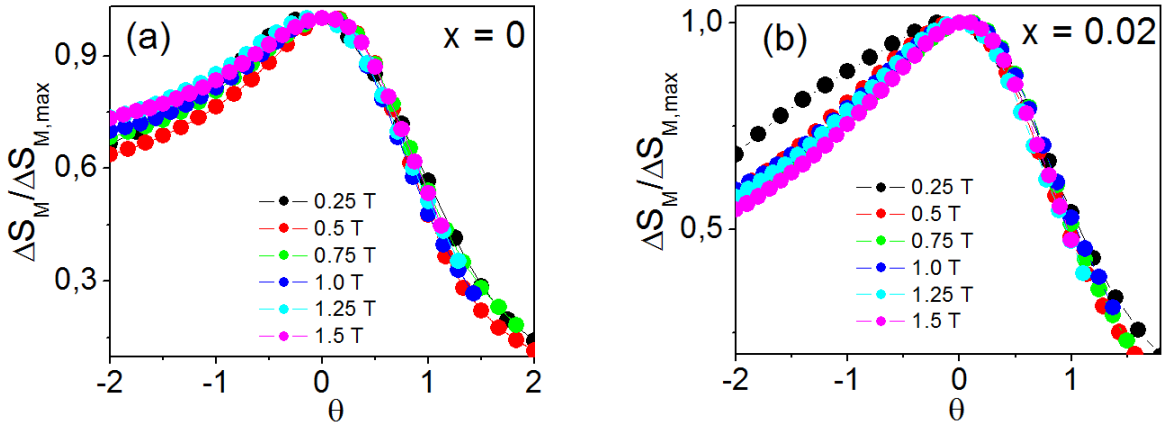

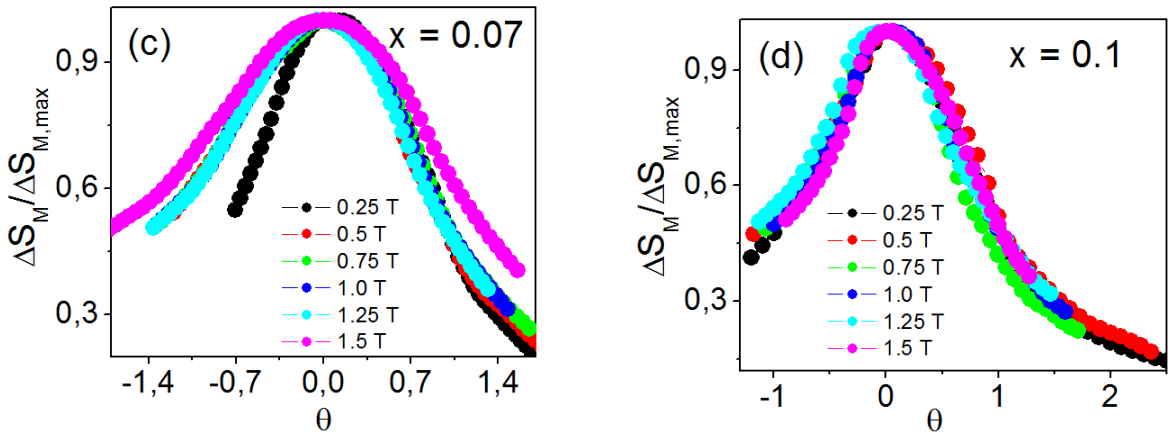

As the second order transition has been proved for all the $La_{0.7}Ca_{0.3}Mn_{1-x}Ni_xO_3$ (x = 0, 0.02, 0.07, 0.1) samples, it is expected that the magnetic field dependence of ΔS_M varies according to the relation $\Delta S_M = a\ H^n$, where *a* is a constant and *n* a magnetic-state-dependent exponent [4-54]. The exponent *n*, which depends on the temperature and the field, can be locally calculated as: $n = \frac{dln|\Delta S_M|}{dlnH}$. The variation of ΔS_M as a function of *H* around the T_C is well described by a power relation and 0.88 (0.79), 0.90 (0.86), 0.84 (0.89) and 0.85 (0.77) *n* values were obtained for $La_{0.7}Ca_{0.3}Mn_{1-x}Ni_xO_3$ samples with x = 0, 0.02, 0.07, and 0.1, synthesized by means of CS and SSR (in brackets), respectively [4-55]. The field dependence of ΔS_M around T_C with the respective fitting according with the power law for magnetic field strengths from 0 to 1.5 T in 0.25 T steps for $La_{0.7}Ca_{0.3}Mn_{1-x}Ni_xO_3$ (x = 0, 0.02, 0.07, 0.1) samples is displayed in Fig. 3-17 (a) for CS and (b) for SSR process.

Figure 3-17: Field dependence of $|\Delta S_{max}|$ at T_C for $La_{0.7}Ca_{0.3}Mn_{1-x}Ni_xO_3$ (x = 0, 0.02, 0.07, 0.1) samples fitted to a power law $|\Delta S_{max}|$ α H^n synthesized by (a) CS and (b) SSR processes. Temperature dependence of the field exponent *n* for LCMO samples with x = 0 and x = 0.02 obtained at *H* = 1 T synthesized by (c) CS and (d) SSR. Insets: enlarged scale for the region in which the *n* values were lower.

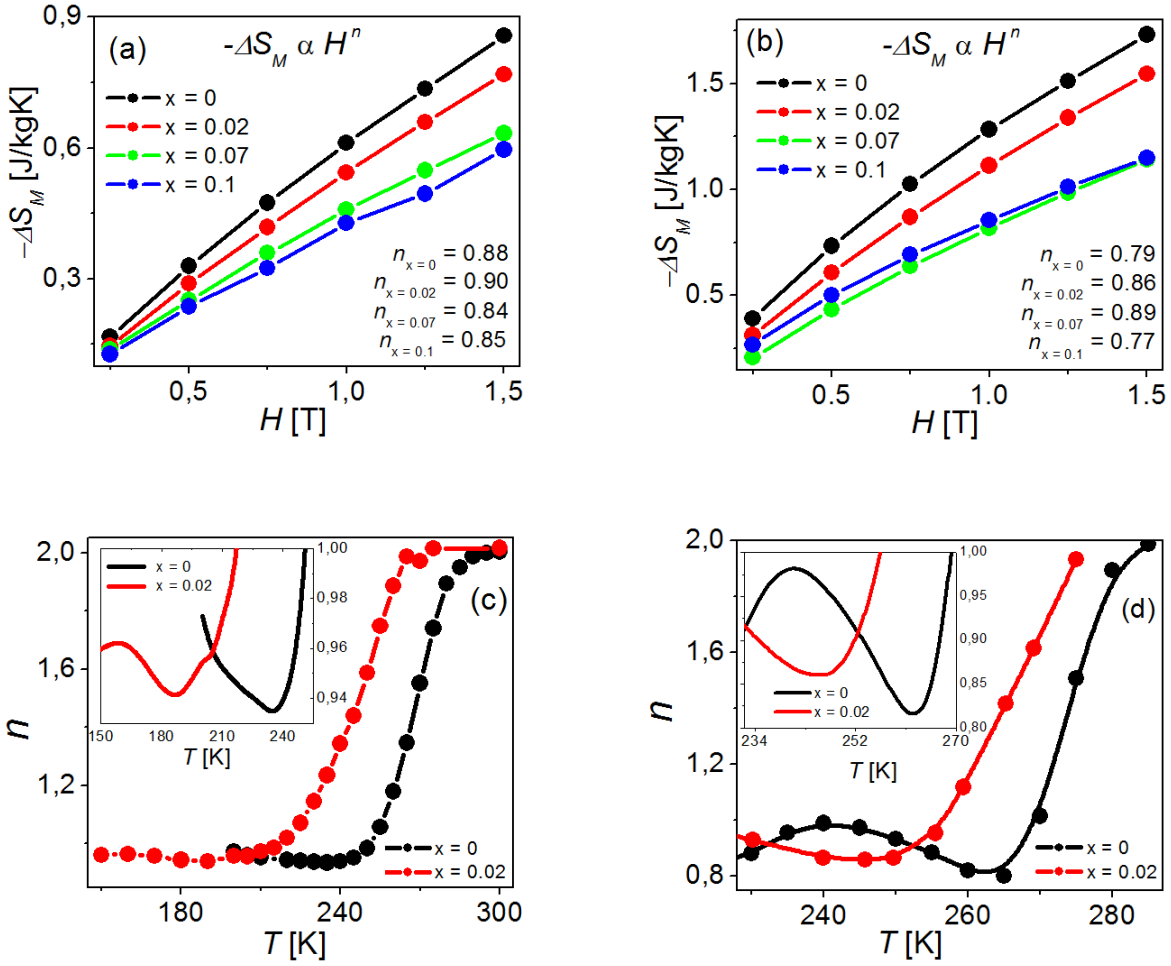

The evolution of the *n(T)* curves resembles that predicted by the mean field model [4-56]. At temperatures below T_C (FM state of the material), *n* has values approaching to 1. This indicates that although the magnetization curves depend on temperature at these temperatures, the *n(T)* dependence is essentially field independent. At temperatures above T_C (PM state of the material), *n* approaches to 2 as a consequence of the Curie-Weiss law [4-57]. At $T = T_C$, values of $n \approx 0.9$ are found for the $La_{0.7}Ca_{0.3}Mn_{1-x}Ni_xO_3$ (x = 0, 0.02, 0.07, 0.1) samples.

Within the framework of the mean field theory, $n = 0.67$ value is predicted at T_C [4-58]. The deviation of *n* from the mean field theory value suggests the existence of magnetic inhomogeneities and/or superparamagnetic clusters in the vicinity of T_C in the compounds. Mean field theory applied to SOPM inhomogeneous ferromagnets has produced *n* values different from 0.67 [4-49, 4-57].

3.2 Critical exponents

The study of the critical behavior in the temperature range near T_C allows one to determine the nature (first or second order) of the phase transitions as well as to estimate the critical exponents of the magnetization (β) and magnetic susceptibility (γ). Thus, the analysis of the critical exponents in the vicinity of the magnetic phase transition is a powerful tool to investigate in details the mechanisms of the magnetic interactions responsible for the transition [6]. Experimental studies of the critical behavior of manganites near the PM-FM phase transition show that the values of the critical exponent β vary from ~0.3 to ~0.5 [7]. Such wide variation range of β implies that different theoretical models should be used to study the critical properties of manganites. In this regard, results of the analysis of the critical properties using the mean-field (β= 0.5), three dimensional (3D)-Heisenberg (β= 0.365), 3D-Ising (β= 0.325), and tricritical mean-field model (β= 0.25) have been reported in a variety of papers [8-10]. The critical exponents γ and δ for the initial susceptibility $\chi(T)$ and critical isotherm $M(T,H)$ can also be determined from static *dc*-magnetization measurements [11].

In this work, the critical phenomena in $La_{0.7}Ca_{0.3}Mn_{1-x}Ni_xO_3$ (x=0.0, 0.02, 0.07, 0.10), manganites are studied by analyzing the critical exponents through various techniques, such as the modified Arrott plot [12] and the Kouvel-Fisher method [13]. As a result, the critical exponents β, γ and δ are determined for the samples with the different Ni-concentrations.

In a standard procedure, the critical exponents should be determined from the modified Arrott plots (MAP) or Arrott-Noakes plots. To do this, the isothermal $M^{1/\beta}$ versus $(H/M)^{1/\gamma}$ curves should be constructed from the isothermal $M=f(H)$ data [20]. The MAP isotherms were constructed for the $La_{0.7}Ca_{0.3}Mn_{1-x}Ni_x$ (x=0, 0.02, 0.07, and 0.1) samples using fourth models of critical exponents: 3D-Heisenberg (β=0.365, γ=1.336) in Fig. 3-18 and Fig. 3-19, for CS and SSR samples, respectively; tri-critical mean-field model (β=0.25, γ=1) in Fig 3-20 and Fig. 3-21, for CS and SSR samples, respectively; 3D-Ising model (β=0.325, γ=1.241) in Fig. 3-22 and Fig. 3-23, for CS and SSR samples, respectively; and mean-field model (β=0.5, γ=1) in Fig. 3-8 and Fig. 3-9, for CS and SSR samples, respectively.

Figure 3-18: MAP isotherms for 3D-Heisenberg model (β=0.365, γ=1.336) at different temperatures for $La_{0.7}Ca_{0.3}Mn_{1-x}Ni_xO_3$ (x = 0, 0.02, 0.07, 0.1) samples obtained by means of CS synthesis.

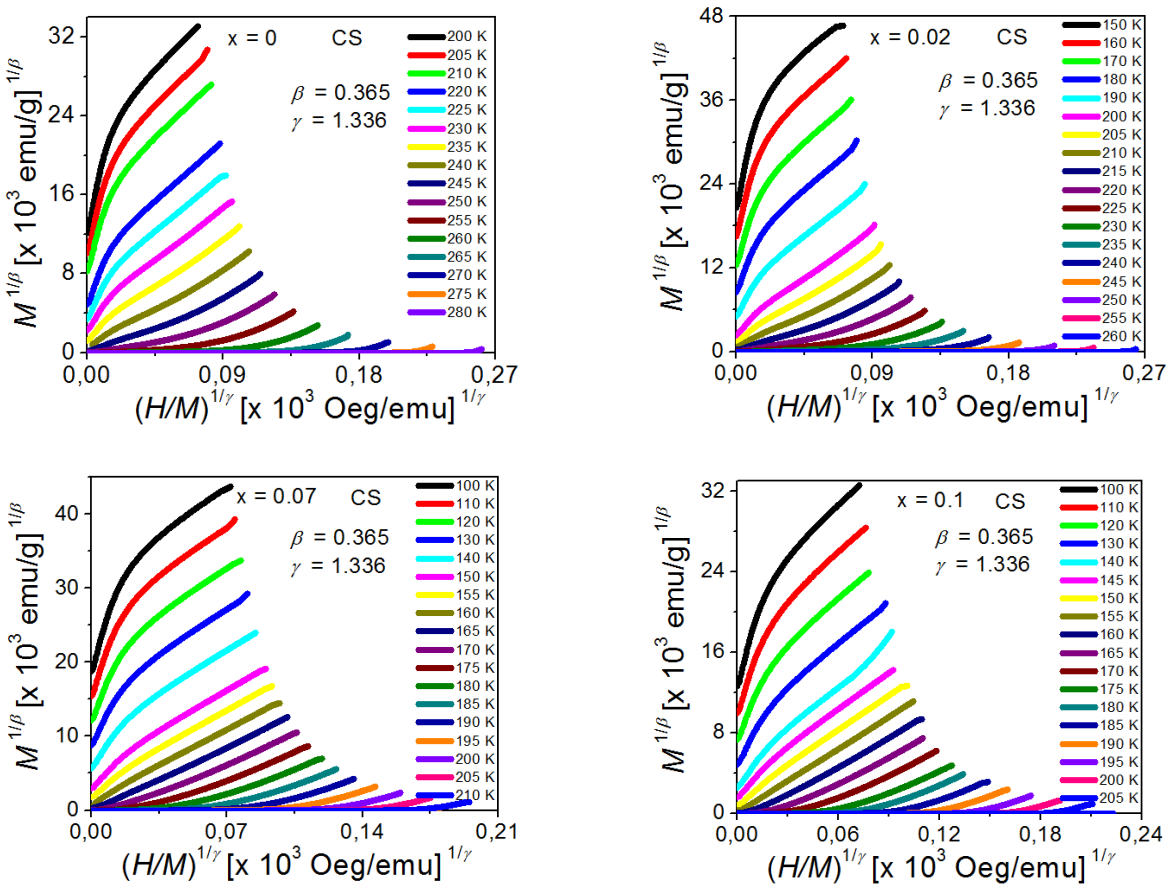

Figure 3-19: MAP isotherms for 3D-Heisenberg model (β=0.365, γ=1.336) at different temperatures for $La_{0.7}Ca_{0.3}Mn_{1-x}Ni_xO_3$ (x = 0, 0.02, 0.07, 0.1) samples obtained by means of SSR synthesis.

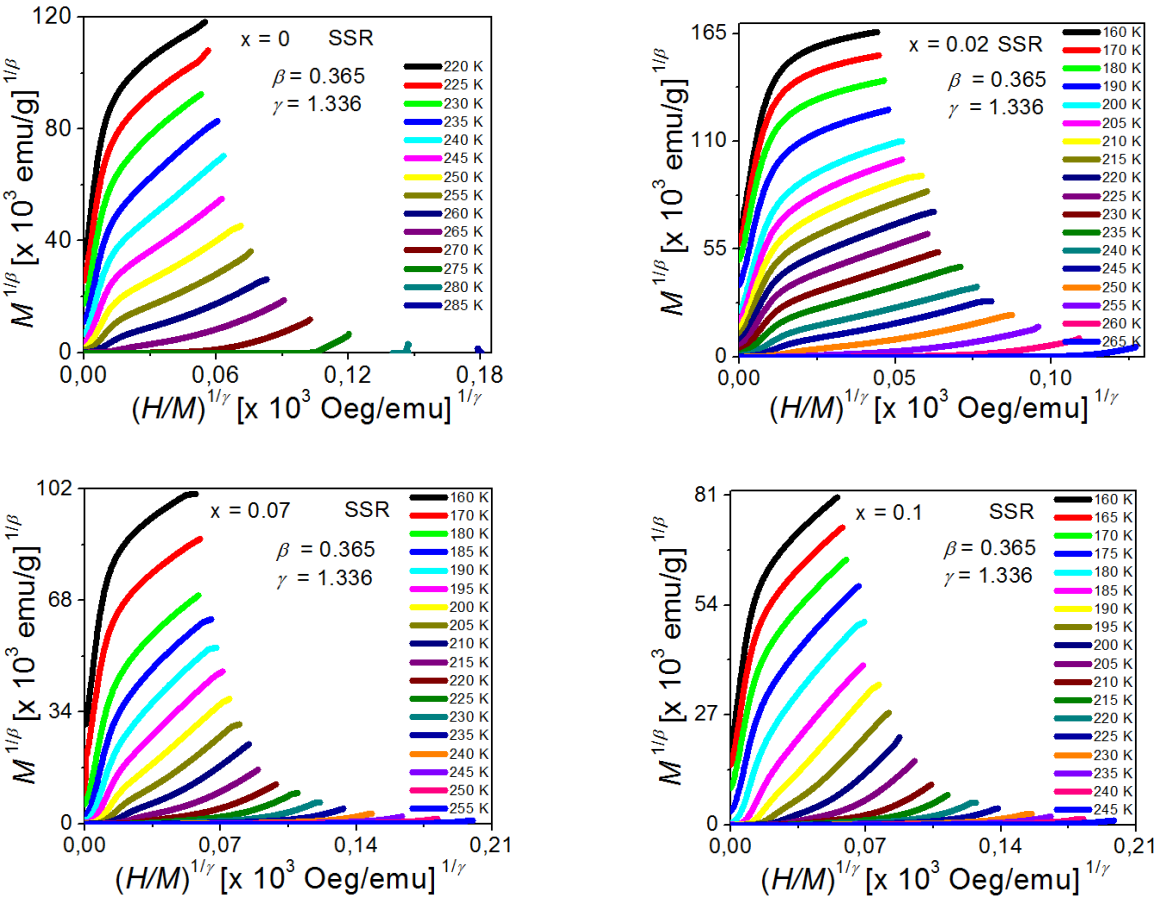

Figure 3-20: MAP isotherms for tri-critical mean-field model (β=0.25, γ=1) at different temperatures for $La_{0.7}Ca_{0.3}Mn_{1-x}Ni_xO_3$ (x = 0, 0.02, 0.07, 0.1) samples obtained by means of CS synthesis.

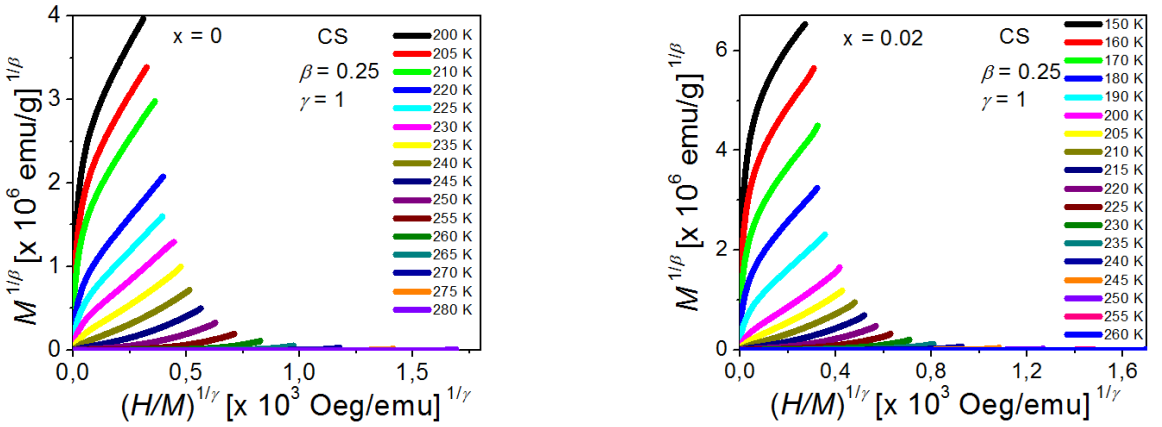

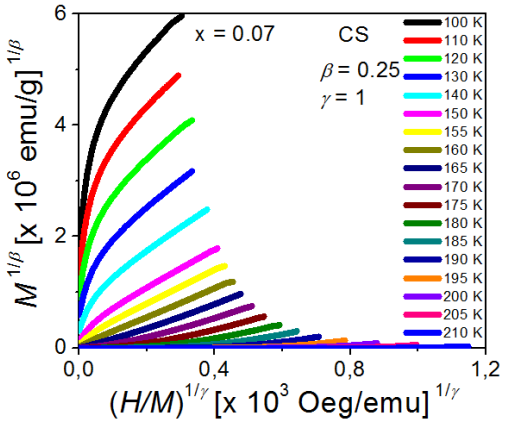

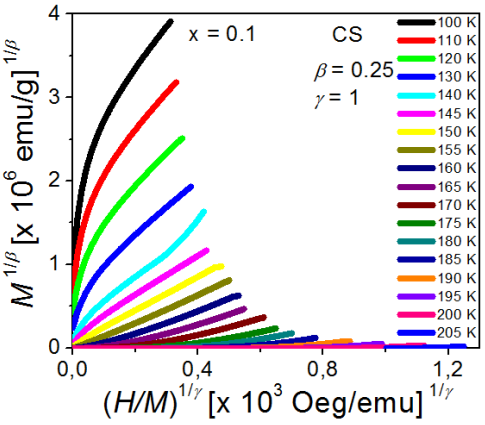

Figure 3-21: MAP isotherms for tri-critical mean-field model (β=0.25, γ=1) at different temperatures for $La_{0.7}Ca_{0.3}Mn_{1-x}Ni_xO_3$ (x = 0, 0.02, 0.07, 0.1) samples obtained by means of SSR synthesis.

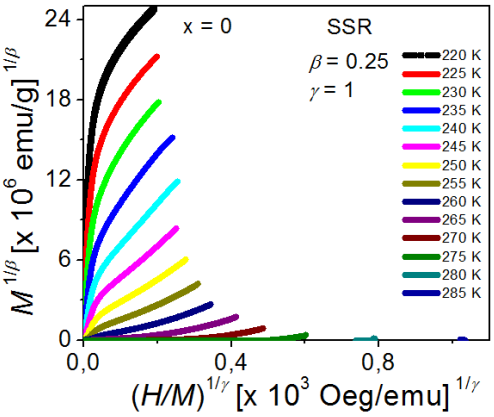

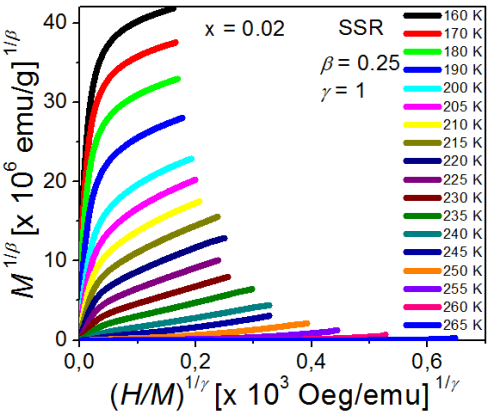

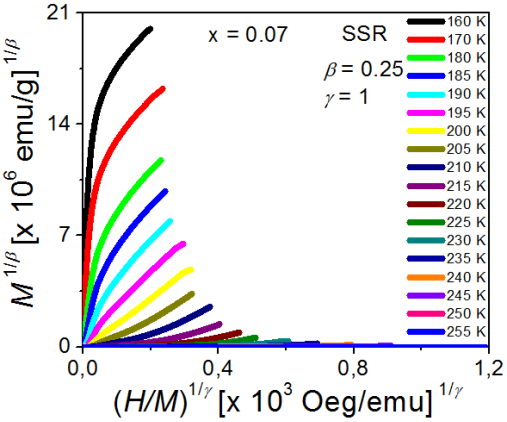

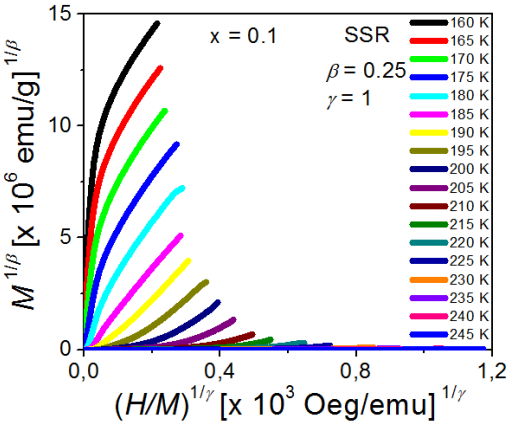

Figure 3-22: MAP isotherms for 3D-Ising model (β=0.325, γ=1.241) at different temperatures for $La_{0.7}Ca_{0.3}Mn_{1-x}Ni_xO_3$ (x = 0, 0.02, 0.07, 0.1) samples obtained by means of CS synthesis.

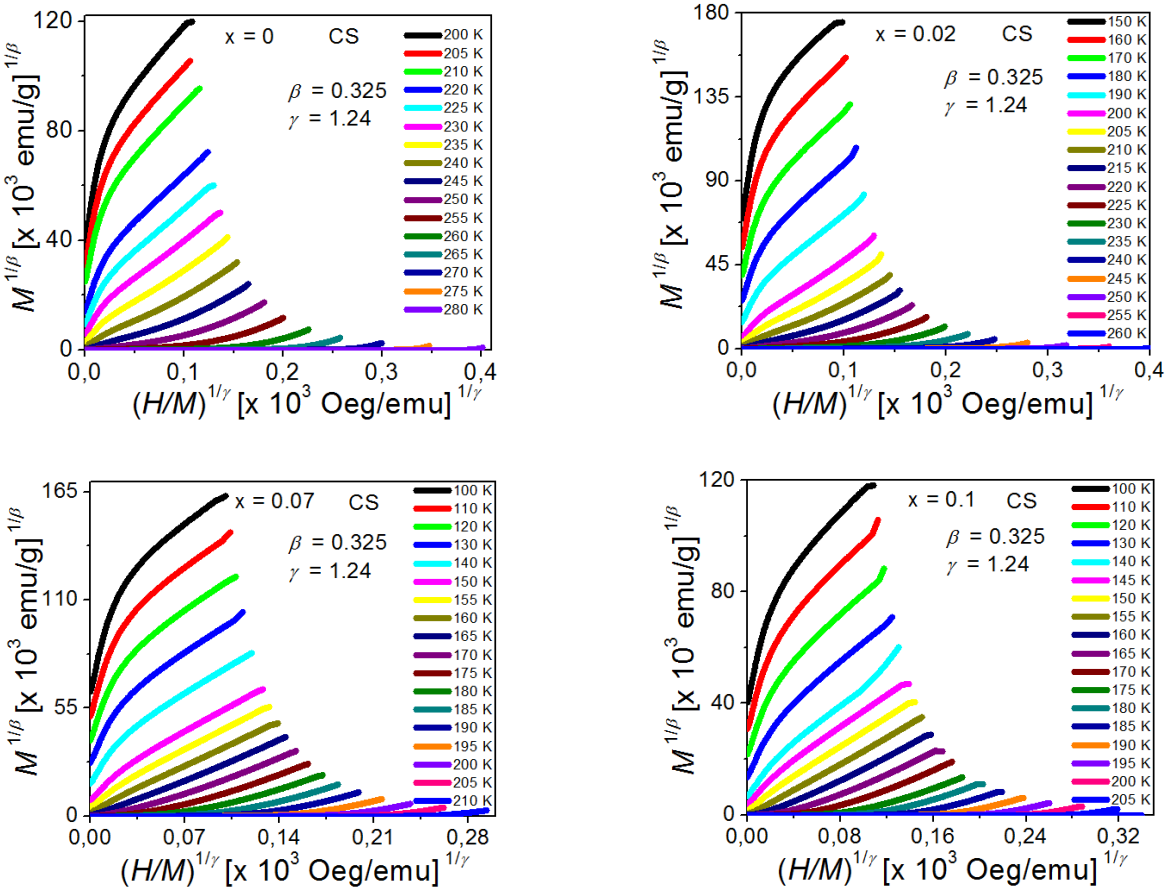

Figure 3-23: MAP isotherms for 3D-Ising model (β=0.325, γ=1.241) at different temperatures for $La_{0.7}Ca_{0.3}Mn_{1-x}Ni_xO_3$ (x = 0, 0.02, 0.07, 0.1) samples obtained by means of SSR synthesis.

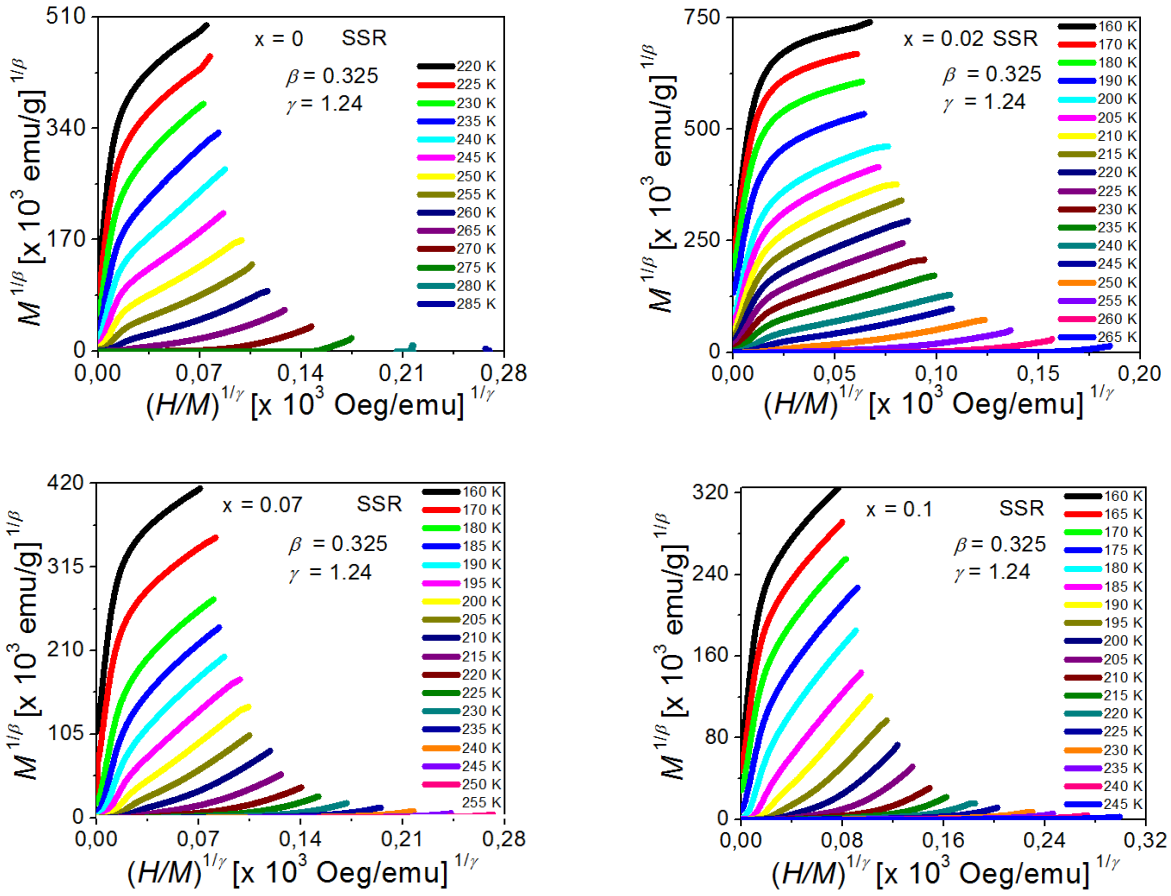

In the high field region, the models generated quasi-straight and nearly parallel lines. This result made the choice of the suitable model to determine the critical exponents difficult. In such context, it is common to resort to the concept of the relative slope (RS) to ascertain the model, which would describe the behavior of the system in the best way possible. RS is defined at the critical point as RS=S(T)/S(T_C). Then, the most suitable model describing the systems is that with values of RS close to the unity regardless of the temperature. The RS data for the samples (x=0, 0.02, 0.07, 0.1) synthesized by CS and SSR are plotted in Fig. 3-24 and Fig. 3-25, respectively. It is evident that the mean-field model is the more suitable to assess the critical exponents of the investigated samples.

Figure 3-24: Relative slope RS=S(T)/S(T_C) as a function of temperature for the samples with x = 0, 0.02, 0.07, 0.1, obtained by CS process.

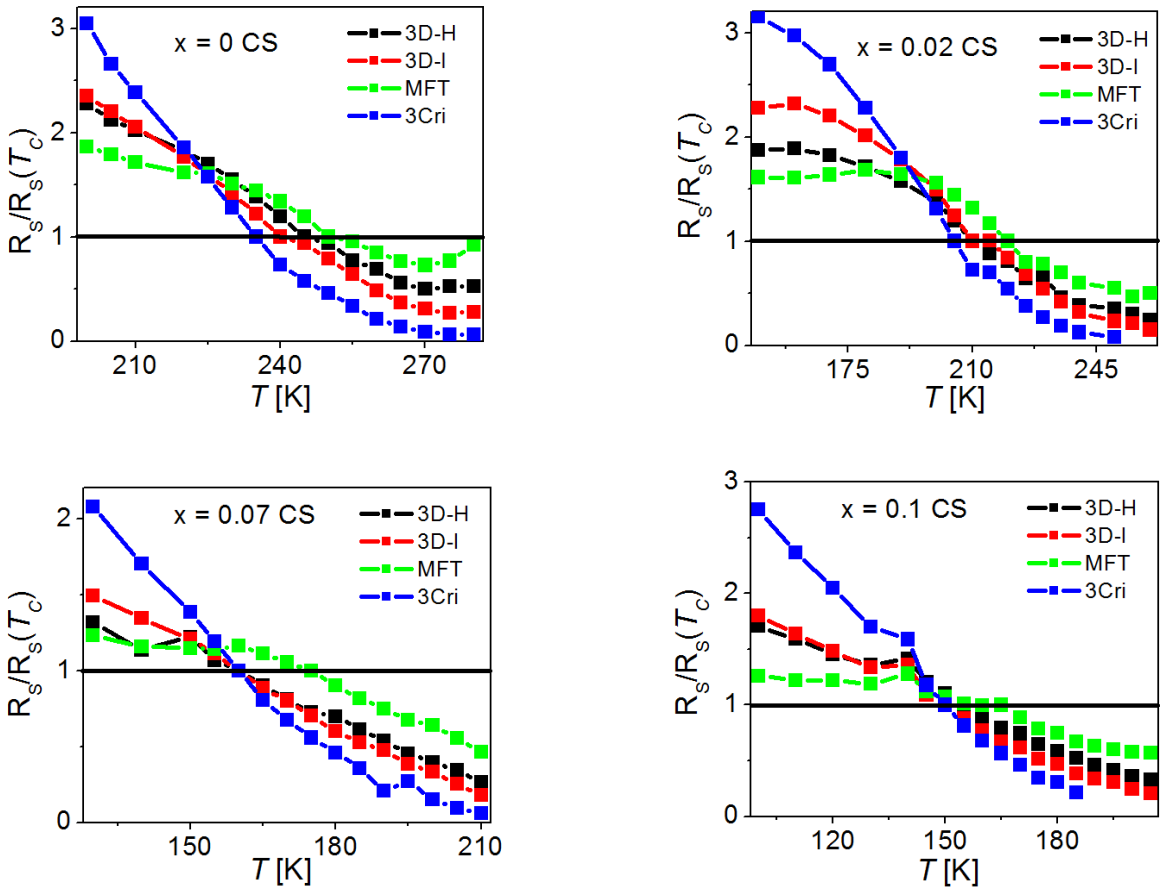

Figure 3-25: Relative slope RS=S(T)/S(T_C) as a function of temperature for the samples with x = 0, 0.02, 0.07, 0.1, obtained by SSR process.

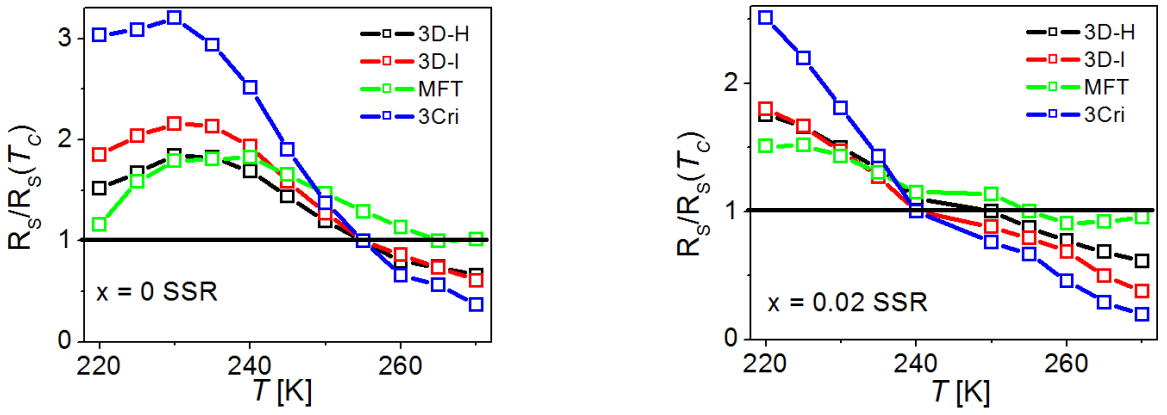

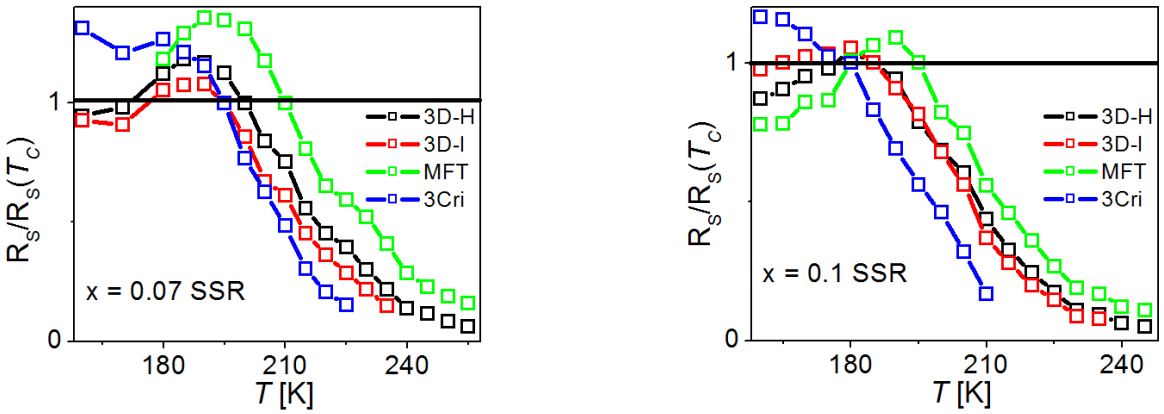

The Arrott plots can be used to estimate the critical exponents in a region around the phase transition temperature. This, in turn, allows one to understand the nature of the second-order magnetic phase transition near the Curie point. The critical exponents β and γ can be evaluated from spontaneous magnetization (M_s) and initial susceptibility (χ_0), below and above T_C, respectively. The critical isothermal exponent, δ, is evaluated by plotting the critical isotherm at $T=T_C$ and fitting the relation $M=D(H)^{1/\delta}$ to the experimental data. In short, the mentioned critical exponents are given by the relations: $M_s(T)=M_0(-\varepsilon)^{\beta}$, $\varepsilon<0$, $T<T_C$, $\chi_0^{-1}(T)= \lim_{H\to 0} (H/M)=(h_0/M_0)\varepsilon^{\gamma}$, $\varepsilon>0$, $T>T_C$, and $M=D(H)^{1/\delta}$, $\varepsilon=0$, $T=T_C$ [21]. In the latter equations ε represents the reduced temperature [$\varepsilon=(T-T_C)/T_C$], and the constants M_0, h_0, and D correspond to critical amplitudes. The extrapolation of the Arrott plots to $H/M= 0$ for $T<T_C$ and $M^2=0$ for $T>T_C$ allows one to obtain the spontaneous magnetization $M_s(T,0)$ and the inverse initial susceptibility $\chi_0^{-1}(T,0)$ values, respectively. The functions $M_s(T,0)=M_0(\varepsilon)^{\beta}$ and $\chi_0^{-1}(T,0)=(h_0/M_0)\varepsilon^{\gamma}$ are then fitted to the experimental data (Fig. 3-26 and Fig. 3-27 to CS and SSR samples, respectively) in order to determine the values of the exponents β and γ. The results for the samples with x=0, 0.02, 0.07, and 0.1 are indicated in the respective plots. It can be readily seen in Fig. 3-26 and Fig. 3-27 that the values of the critical exponents β and γ are close to those predicted by the mean-field theory. This result strongly suggests that the interactions among spins in the investigated manganites are long-ranged [22].

As for the critical exponent δ, its value can be determined by plotting the critical isotherm at $T=T_C$ and fitting the relation $M=D(H)^{1/\delta}$ to the experimental data. For x=0, 0.02, 0.07, 0.1 samples, the linear fitting of the $M(H)$ curves recorded at 250, 220, 175 and 165 K (Fig. 3-

28) gave the δ values of 3.01, 3.18, 3.04 and 3.2, respectively, for samples synthesized by means of CS process.

For x=0, 0.02, 0.07, 0.1 samples, the linear fitting of the *M*(*H*) curves recorded at 255, 235, 200 and 180 K (Fig. 3-29) gave the δ values of 2.89, 3.05, 3.0 and 2.89, respectively, for samples synthesized by means of SSR process.

Figure 3-26: Spontaneous magnetization $M_S(T,0)$ and inverse initial susceptibility $\chi_0^{-1}(T)$ for samples with x = 0, 0.02, 0.07, 0.1 synthesized by CS process.

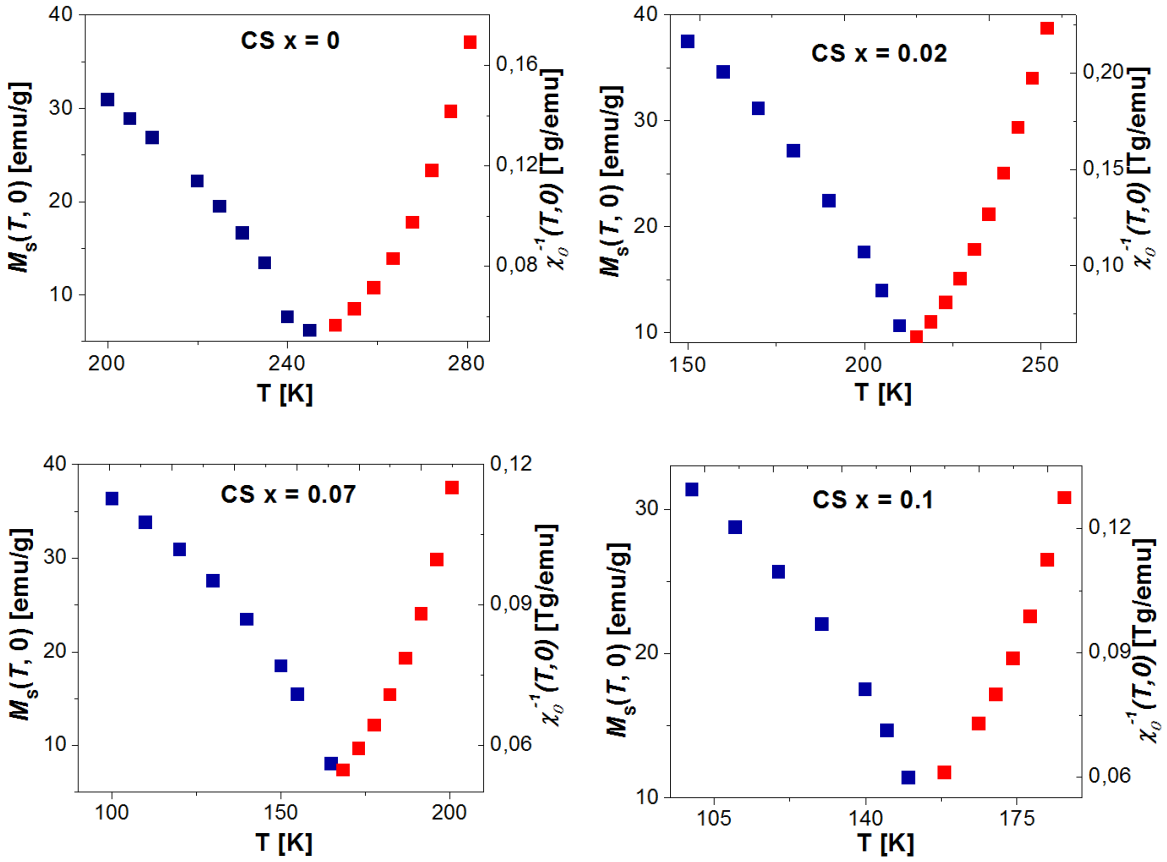

Figure 3-27: Spontaneous magnetization $M_S(T,0)$ and inverse initial susceptibility $\chi_0^{-1}(T)$ for samples with x = 0, 0.02, 0.07, 0.1 synthesized by SSR process.

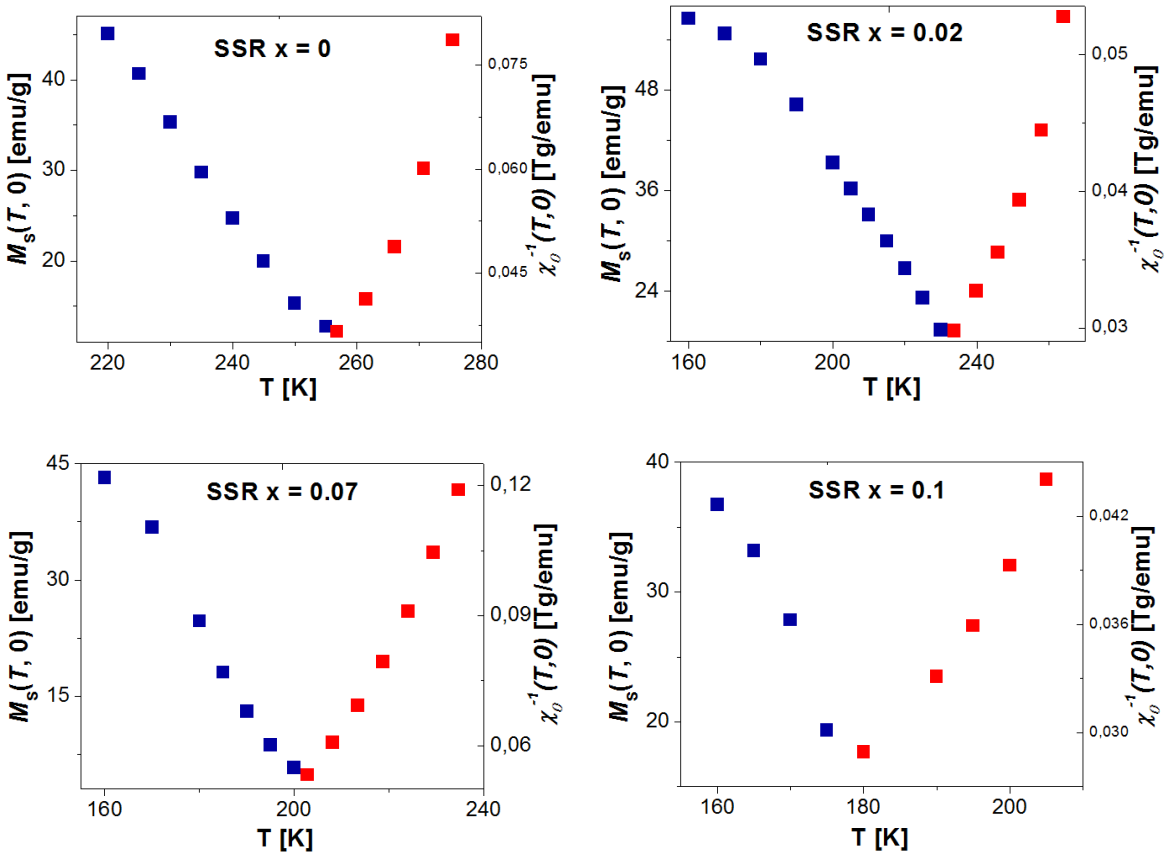

Figure 3-28. Critical isotherm on a log-log scale (inset) for samples with x= 0, 0.02, 0.07, 0.1 at 250, 220, 175 and 165 K, respectively, synthesized by CS process.

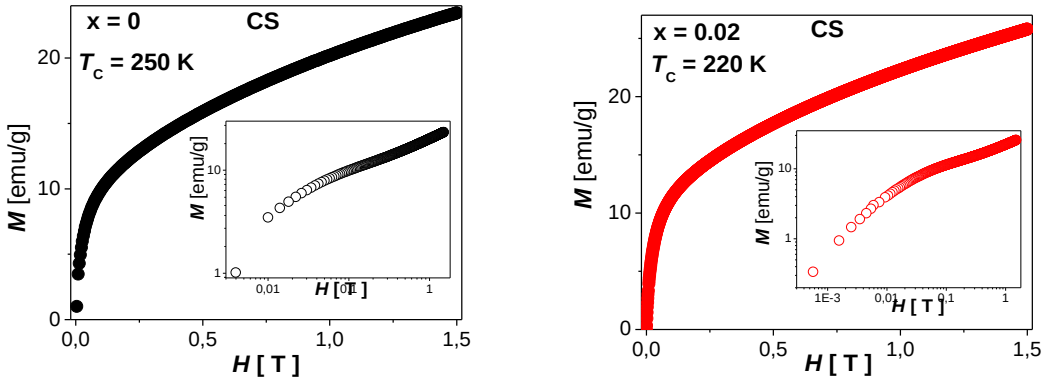

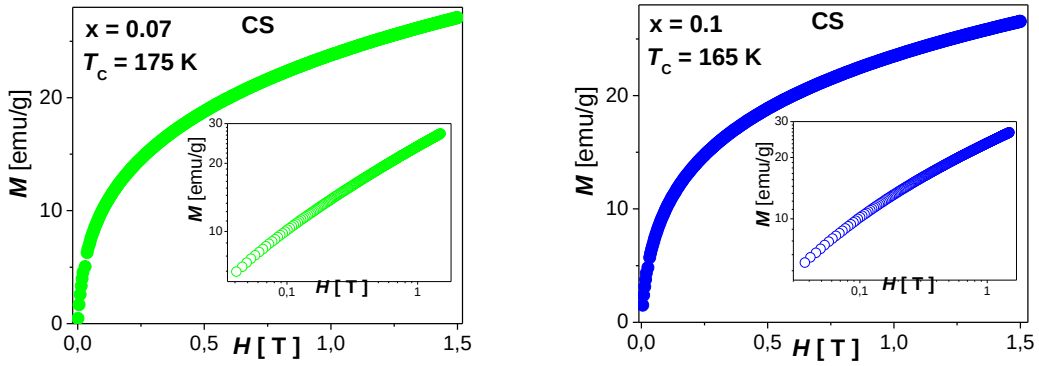

Figure 3-29. Critical isotherm on a log-log scale (inset) for samples with x= 0, 0.02, 0.07, 0.1 at 255, 235, 200 and 180 K, respectively, synthesized by SSR process.

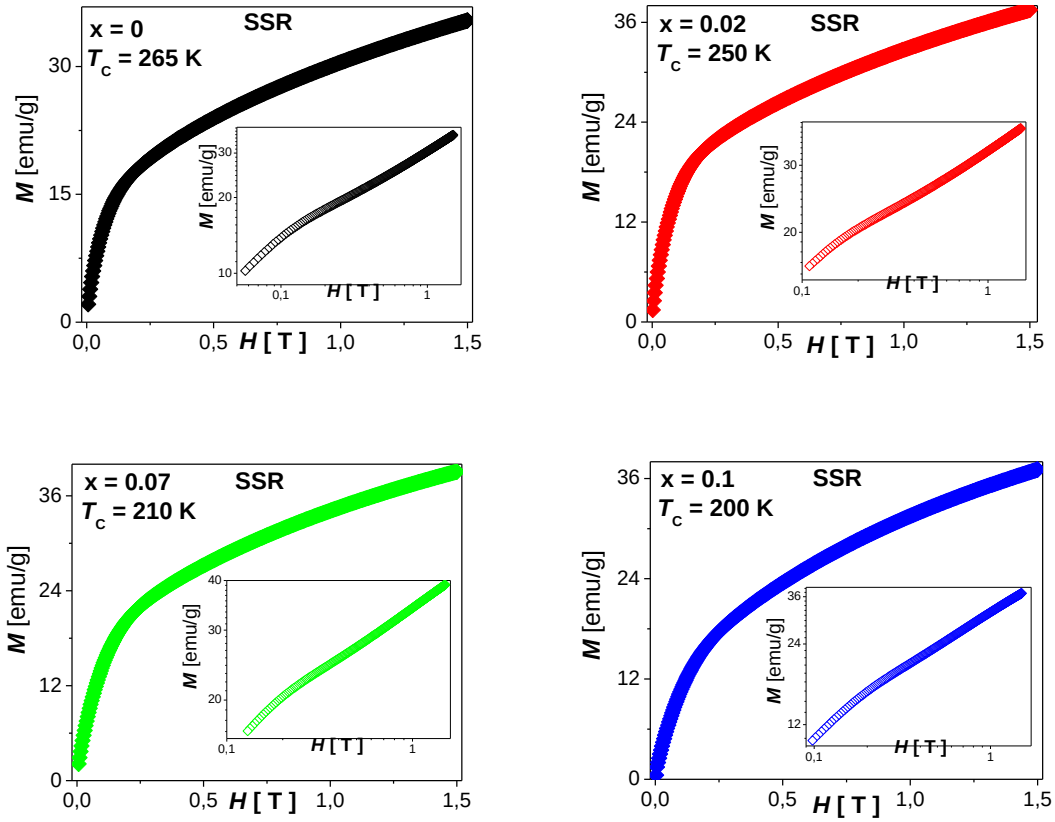

An additional method to obtain the critical exponents with higher accuracy is the Kouvel Fisher method (KFM) [23]. In the framework of this model, the critical exponents β and γ are determined through the equations $M_s(T)/[dM_s(T)/dT]=(T-T_C)/\beta$, and $\chi_0^{-1}(T)/[d\chi_0^{-1}(T)/dT]=(T-T_C)/\gamma$, respectively. The evaluation of the critical exponents requires the

plotting of the $M_s(T)/[dM_s(T)/dT]$ and $\chi_0^{-1}(T)/[\,d\chi_0^{-1}(T)/dT]$ curves, from whose slopes ($1/\beta$ and $1/\gamma$) the values of the critical exponents are obtained. The linear fit to the plots following the KF method (Fig. 3-30 and Fig. 3-31 for samples obtained by CS and SSR process, respectively) yielded values of the critical exponents β and γ, which are consistent with those obtained using the modified Arott plots. Hence, it is possible to assert that the method used to study of critical behavior in the nanometric-sized manganites is effective and feasible.

Figure 3-30. Kouvel-Fisher plots for the spontaneous magnetization and the inverse susceptibility for $La_{0.7}Ca_{0.3}Mn_{1-x}Ni_xO_3$ (x = 0, 0.02, 0.07, 0.1) samples obtained by means of CS synthesis.

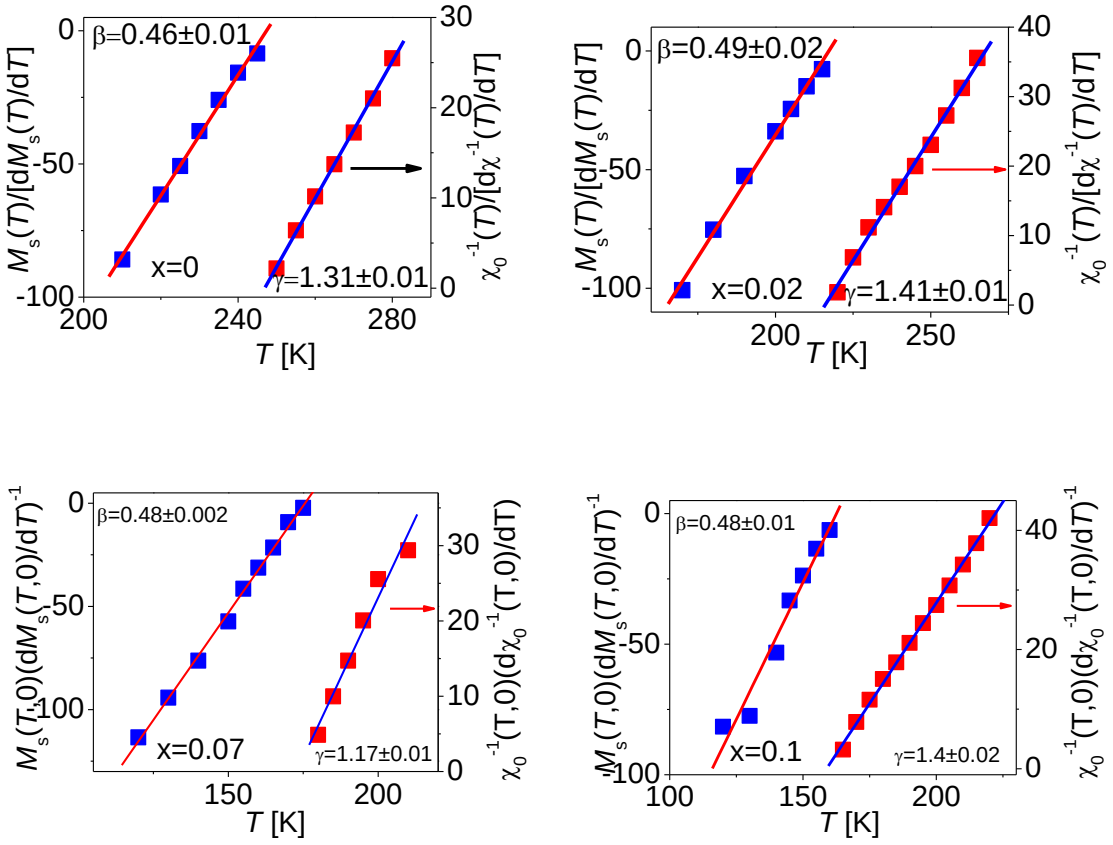

Figure 3-31. Kouvel-Fisher plots for the spontaneous magnetization and the inverse susceptibility for $La_{0.7}Ca_{0.3}Mn_{1-x}Ni_xO_3$ (x = 0, 0.02, 0.07, 0.1) samples obtained by means of SSR synthesis.

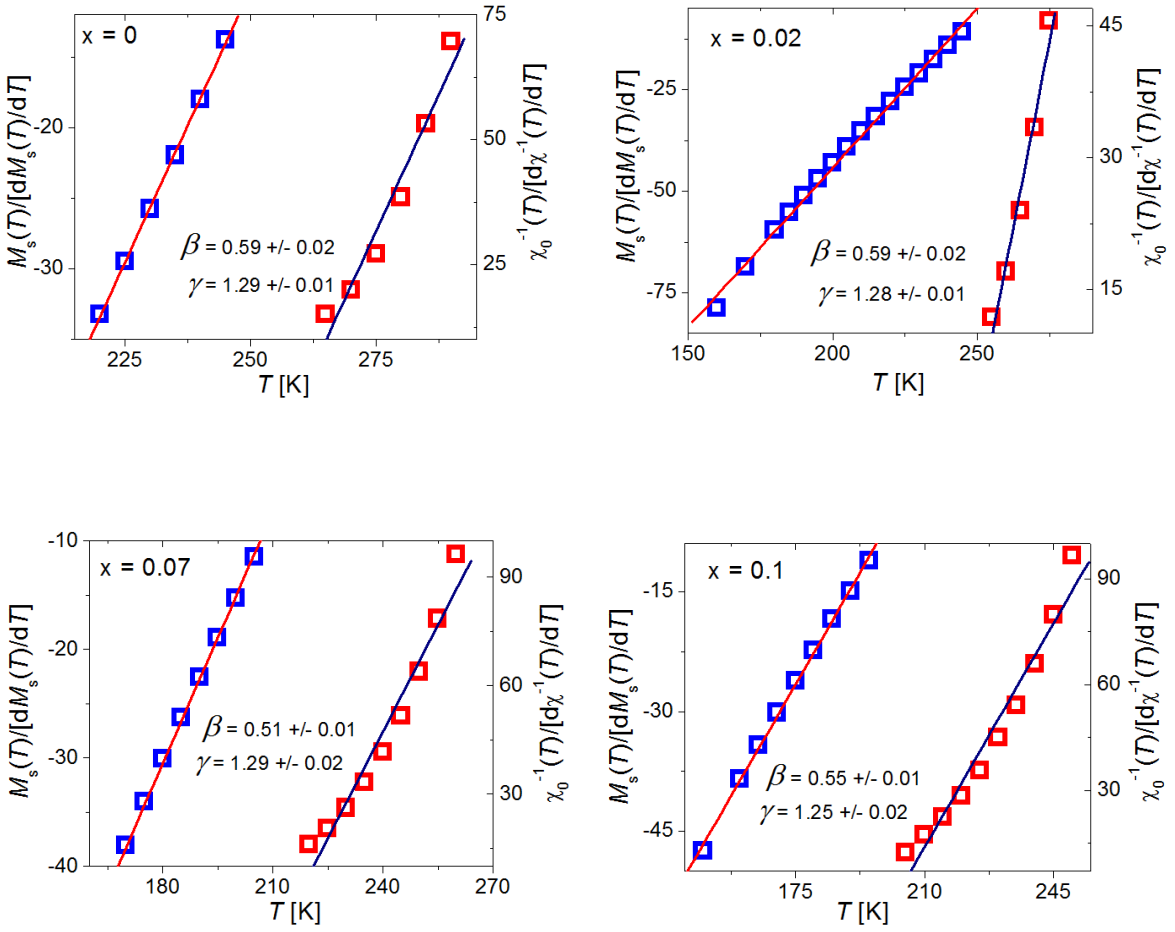

The scaling theory suggests that the magnetization and internal field should obey the universal law $M(H,\varepsilon)=\varepsilon^{\beta}f\pm(H/\varepsilon^{\gamma+\beta})$. As previously stated, the plot of $M/|\varepsilon|^{\beta}$ versus $H/|\varepsilon|^{\gamma+\beta}$ near T_C should lead to a falling of the magnetic isotherms into two individual branches (one for $T>T_C$ and other for $T<T_C$). The isothermal magnetizations around T_C are plotted as $M/|\varepsilon|^{\beta}$ versus $H/|\varepsilon|^{\gamma+\beta}$ (log-log plot) in Fig. 3-32 and Fig 3-33 using β and γ values deduced from the KF method for the x=0, 0.02, 0.07, 0.1 samples processed by CS and SSR, respectively. It is evidenced that all the magnetization data fall into two sides, one for $T > T_C$ and the other for $T < T_C$, in agreement with the scaling theory. This finding suggests that the values of the exponents are accurate enough so as to be considered as intrinsic.

Figure 3-32. Scaling plots on a log-log scale of $M/|\varepsilon|^{\beta}$ versus $H/|\varepsilon|^{\beta+\gamma}$ for the x=0, 0.02, 0.07, 0.1 samples obtained by CS process.

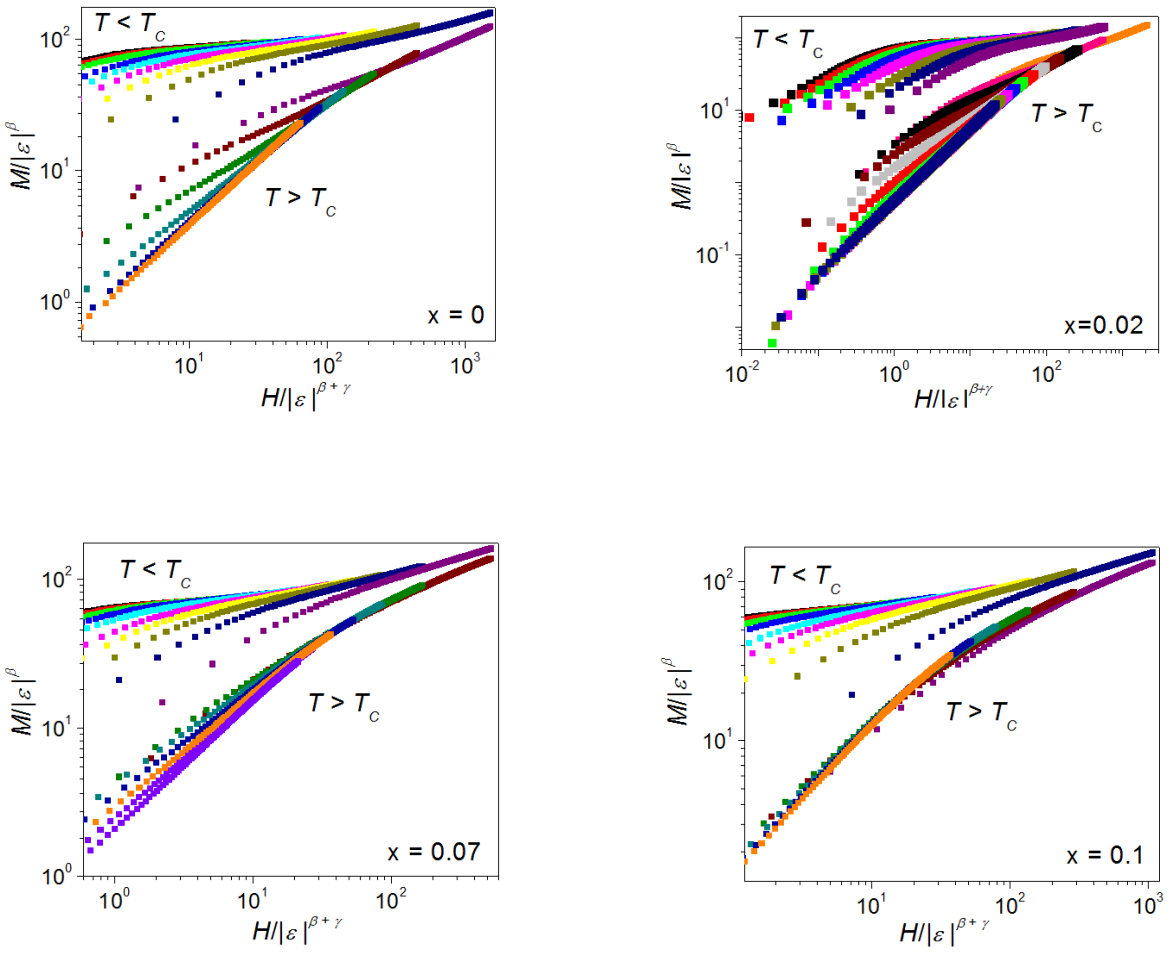

Figure 3-33. Scaling plots on a log-log scale of $M/|\varepsilon|^{\beta}$ versus $H/|\varepsilon|^{\beta+\gamma}$ for the x=0, 0.02, 0.07, 0.1 samples obtained by SSR process.

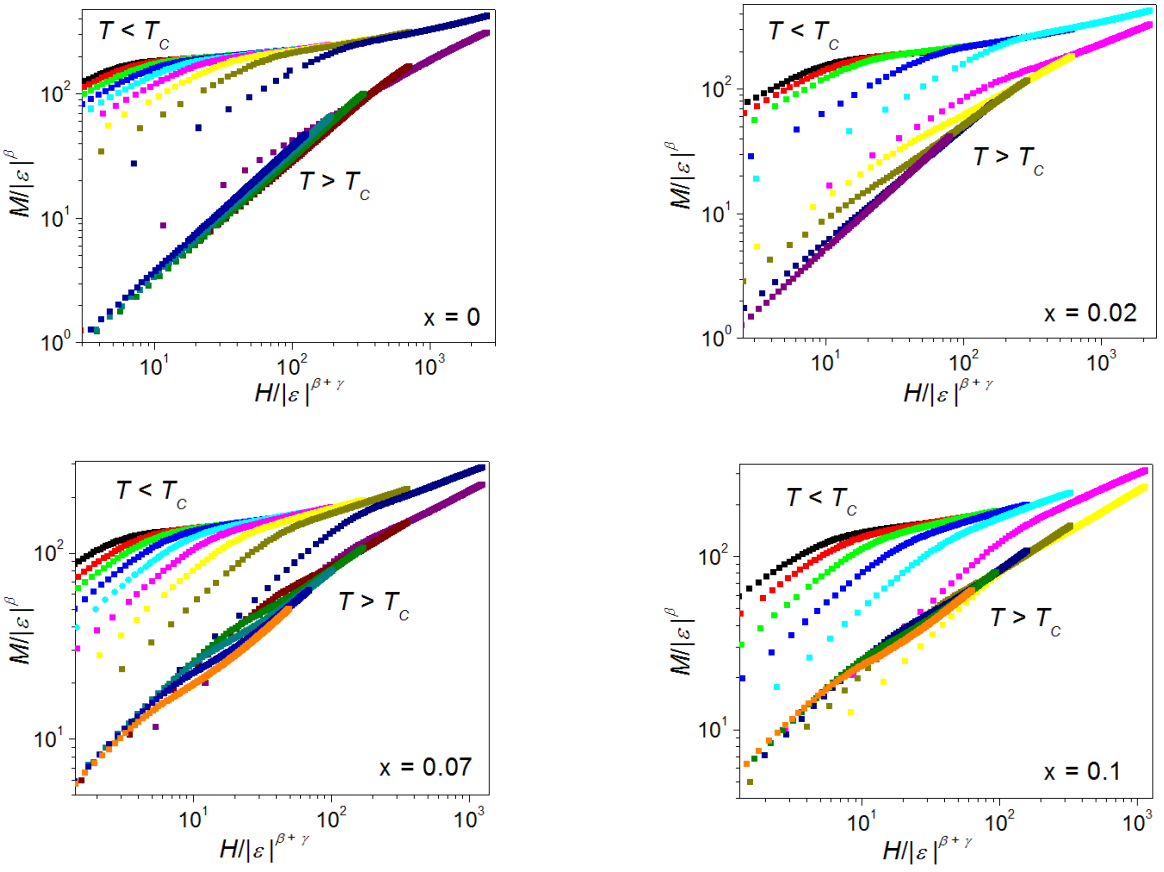

3.3 Electrical transport properties and relationship with the MCE

Perovskite LCMO manganites are not only important because their elastic [4-59], structural, electronic and magnetic transition properties [4-60], but also because its extraordinary colossal magnetoresistance (CMR) property. Interestingly, the magnetoresistance (MR) and the magnetocaloric (MC) effect in manganites are usually observed around the FM–PM phase transition [4-61]. Hence, the existence of a close relationship between the electrical and magnetic properties in LCMO, namely the change

in resistivity and magnetic entropy, is anticipated. Certainly, in the frame work of the double exchange theory the electrons tend to hop between Mn ions of different valences while keeping their spin unchanged. Therefore, when the arrangement of the spin of the Mn ions is modified by external field, resistivity should change simultaneously [4-62]. In this scenario, the CMR effect in the manganites has been qualitatively understood [4-63, 4-64]. The interplay between the magnetic and resistive behavior in manganites as well as the effect of Ni^{2+} doping on their magneto-transport properties have been explored in the nano-sized $La_{0.7}Ca_{0.3}Mn_{1-x}Ni_xO_3$ samples synthesized by CS and standard SSR methods. Fig. 3-34 and Fig. 3-35 shows the dependence of the resistivity on the temperature, *ρ(T)*, at *H* = 0, 1.25, 2.5 and 5.0 T for $La_{0.7}Ca_{0.3}Mn_{1-x}Ni_xO_3$ (x = 0, 0.02, 0.07, 0.1) samples obtained by means of CS and SSR method, respectively. In these two figures is possible to note a decrease in the resistivity values of the $La_{0.7}Ca_{0.3}Mn_{1-x}Ni_xO_3$ samples with the applied magnetic field. In general terms, the main mechanism responsible of the decrease in the resistivity value upon the application of a magnetic field is the influence of this on the magnetic domains of the material [4-79].

Figure 3-34: Temperature variation of the resistivity at *H* = 0, 1.25, 2.5 and 5.0 T for $La_{0.7}Ca_{0.3}Mn_{1-x}Ni_xO_3$ (x = 0, 0.02, 0.07, 0.1) samples obtained by means of CS.

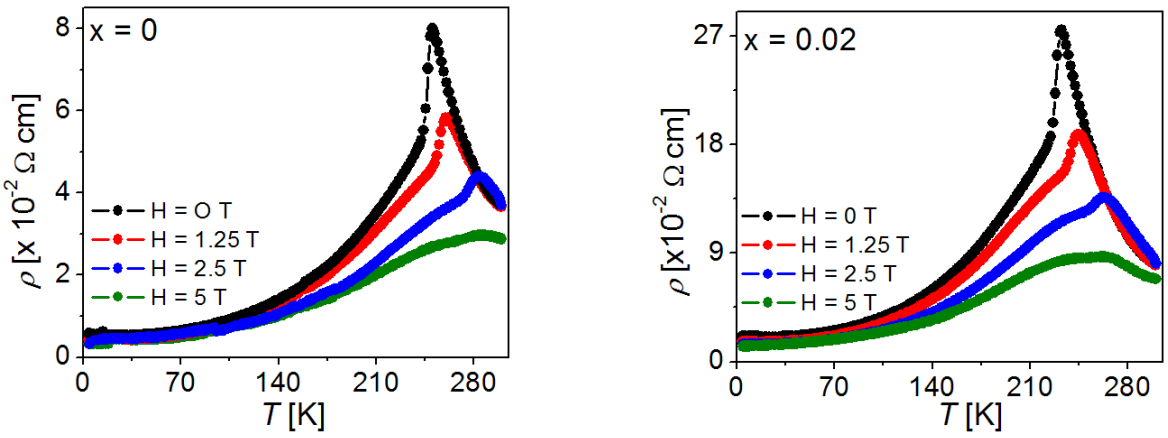

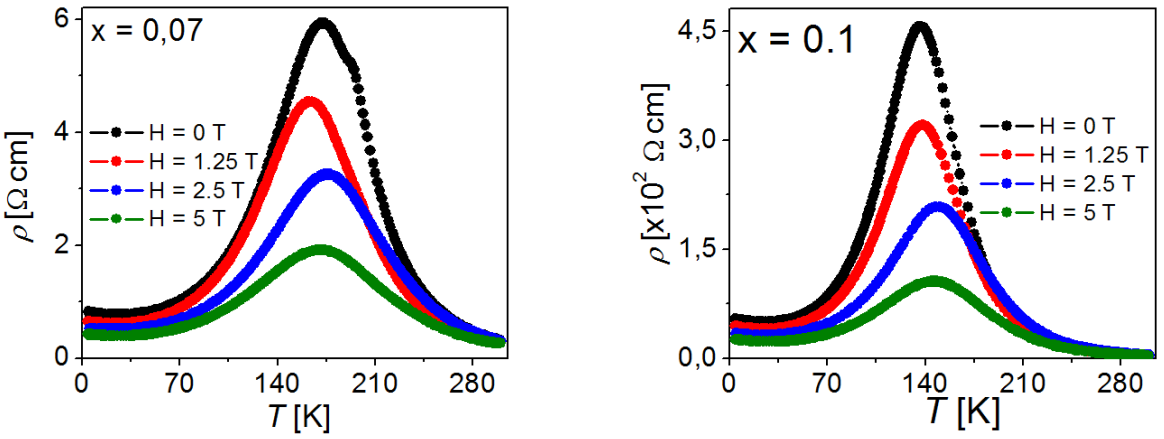

Figure 3-35: Temperature variation of the resistivity at *H* = 0, 1.25, 2.5 and 5.0 T for $La_{0.7}Ca_{0.3}Mn_{1-x}Ni_xO_3$ (x = 0, 0.02, 0.07, 0.1) samples obtained by means of SSR.

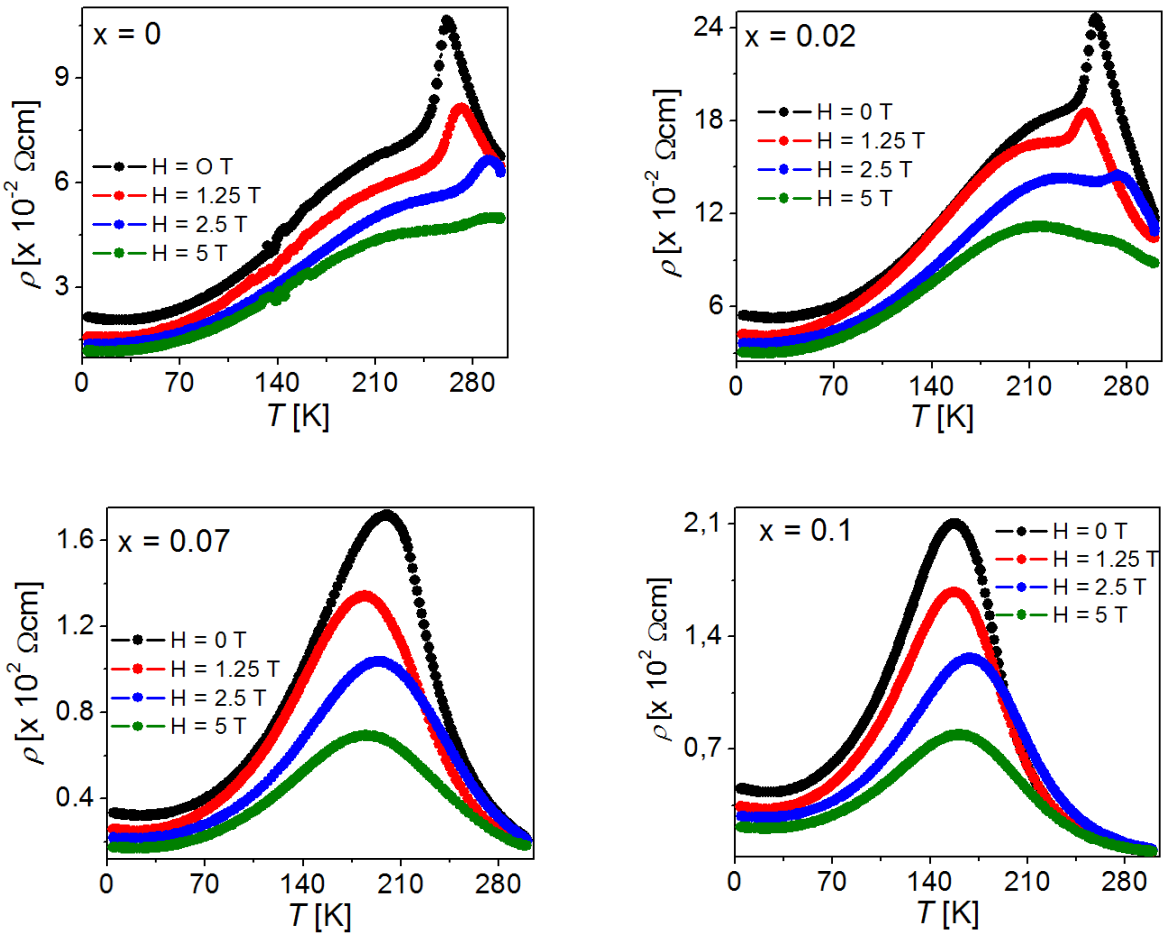

Figure 3-36 shows the dependence of the resistivity on the temperature, $\rho(T)$, at H = 0 T for $La_{0.7}Ca_{0.3}Mn_{1-x}Ni_xO_3$ (x = 0, 0.02) (left) and (x = 0.07, 0.1) (right) samples synthesized by means of CS and SSR methods. It is readily verified that the resistivity first increases with decreasing temperature, and then exhibits a peak around the metal-semiconductor transition temperature T_P [250 (255), 233 (257), 172 (199), 138 (157) for x = 0, x = 0.02, x = 0.07 and x = 0.1, and synthesized by CS and SSR (in brackets), respectively]. The maximum resistivity and transition temperature (T_P) values are listed in Table 3-5.

Figure 3-36: Dependence of the resistivity on the temperature for $La_{0.7}Ca_{0.3}Mn_{1-x}Ni_xO_3$ (x = 0, 0.02) (left) and (x = 0.07, 0.1) (right) samples measured at H = 0 T obtained by means of CS and SSR processes.

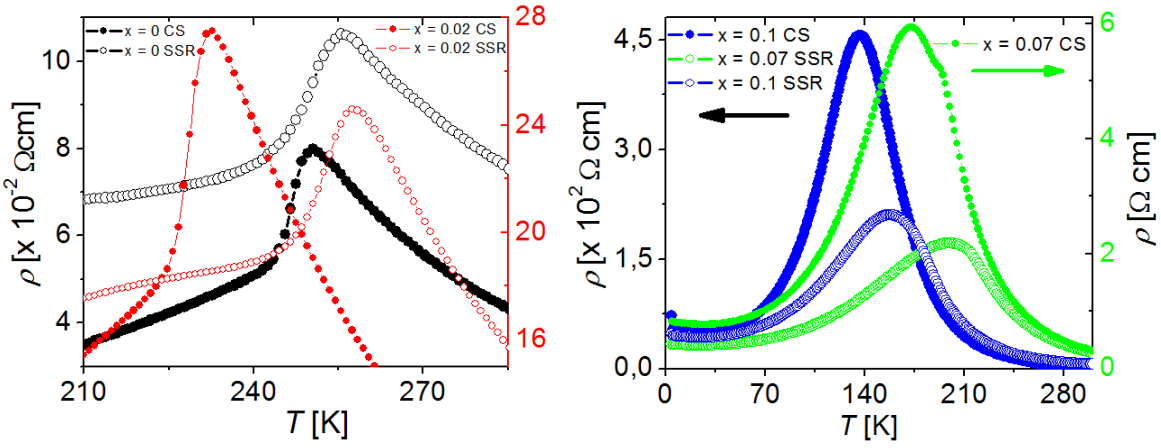

Fig. 3-37 shows the variation of the maximum resistivity values as a function of the Ni^{2+}-content at different magnetic fields (top left panel) and as a function of the magnetic field strength for the different compositions (top right panel). Plot of T_C and T_P versus Ni^{2+}-content (bottom panels) for $La_{0.7}Ca_{0.3}Mn_{1-x}Ni_xO_3$ (x = 0, 0.02, 0.07, 0.1) samples synthesized by mean of CS and SSR process.

Table 3-5: Values for the maximum resistivity and peak temperatures for $La_{0.7}Ca_{0.3}Mn_{1-x}Ni_xO_3$ (x = 0, 0.02, 0.07, 0.1) samples synthesized by mean of CS and SSR methods.

H [T]	X	ρ_{max} [Ω cm]		$T_{p\rho}$ [K]	
		CS	SSR	CS	SSR
0	0	0,08	0,11	250	255
	0,02	0,28	0,25	233	257
	0,07	5,93	171,61	172	199
	0,1	455,97	210,27	136	157
1.25	0	0,06	0,08	260	271
	0,02	0,19	0,18	245	251
	0,07	4,54	134,10	163	184
	0,1	320,26	167,71	138	157
2.5	0	0,04	0,07	284	292
	0,02	0,14	0,14	263	273
	0,07	3,25	103,61	175	194
	0,1	208,09	126,34	150	169
5	0	0,03	0,05	286	294
	0,02	0,09	0,11	262	218
	0,07	1,91	69,22	170	185
	0,1	105,52	78,73	147	160

Figure 3-37: Variation of the maximum resistivity values as a function of the Ni^{2+}-content (top left panel) and as a function of the magnetic field strengths (top right panel) at different compositions for $La_{0.7}Ca_{0.3}Mn_{1-x}Ni_xO_3$ (x = 0, 0.02, 0.07, 0.1) samples synthesized by means of the processes CS and SSR. Plot of T_C and T_P versus Ni^{2+}-content (bottom panels) for $La_{0.7}Ca_{0.3}Mn_{1-x}Ni_xO_3$ (x = 0, 0.02, 0.07, 0.1) samples synthesized by mean of CS and SSR process.

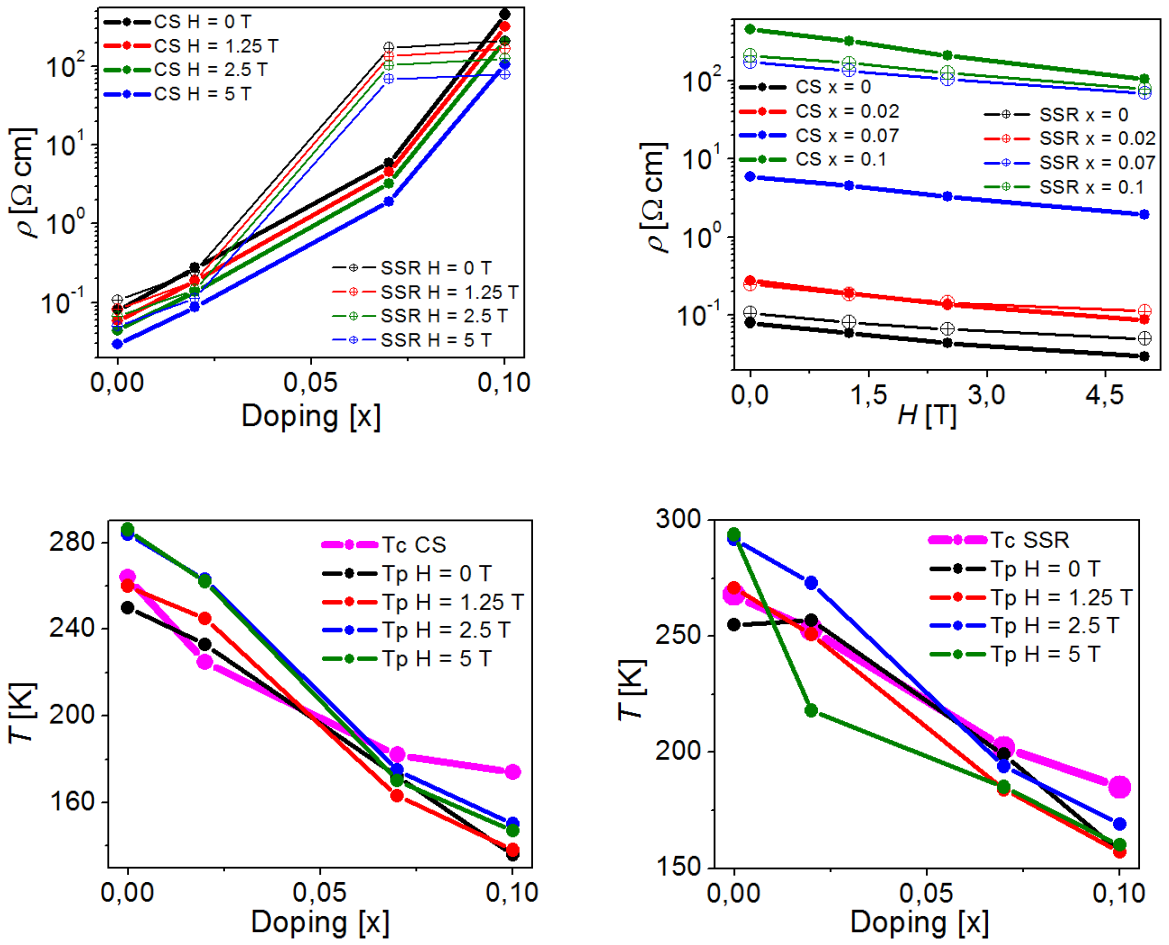

In addition, the resistivity increases and T_P decrease upon Ni^{2+} doping as observed in the Fig. 3-36 top left and bottom panels. These effects can be explained on the basis of the DE mechanism (Mn^{3+}–O–Mn^{4+}) [4-65]. Similar to the magnetic case, the partial substitution of Mn ions by Ni^{2+} leads to change in the Mn^{3+}/Mn^{4+} ratio [4-66]. This change, in turn, produces a decrease in DE evidenced by the decrease in T_P. In short, Ni^{2+}-doping suppresses DE because the Mn^{3+}–O–Ni^{2+} bond does not participate in this mechanism [4-67]. Formation of AFM Ni^{2+}–O–Ni^{2+}, Mn^{4+}–O–Mn^{4+} bonds are also possible, which, weaken the DE interaction [4-68, 4-69]. By increasing the Ni^{2+} doping level, the number of the AFM bonds may increase and this would allow one explain the resistivity increase and the T_P decrease. The increase in the resistivity value of LCMO with Ni^{2+} content can be also explained in terms of the change in the Mn–O–Mn angle (θ). Indeed, it is know that θ plays a relevant role in the e_g electron mobility [4-70]. A deviation of θ from 180° increase the distortion, which decrease the transfer integral $t = t_0 cos(\theta/2)$ (here t_0 represent the

maximum value of *t*). The decrease in the *t* value decreases the DE interaction between Mn ions [4-18] and consequently the resistivity increases. Thus, an orthorhombic structure with increasing bond distortion results in localized carrier and therefore in higher resistivities. Here, it is worth to note that the T_P values of the samples synthesized by CS method are lower than those of the samples obtained by conventional SSR. This is clearly evidenced in the Fig. 3-35 and in the bottom panels of Fig. 3-36 for LCMO samples synthesized by means of CS and SSR processing methods.

The reduction of T_P can be attributed to the downsizing of the particle [4-70] that can decrease the bond angle and increase its length [4-71]. This leads to a decrease in the transfer integral, which in turns decrease T_P. By taking into account the fact that the particle size of the studied samples and synthesized by means of the two used processes are in the nanometer order, it is possible to conclude that the substantial increase in the resistivity value is a consequence of the downsizing of the particle. Similar results were reported by Mahesh et al., [4-70]. The value of the resistivity decrease when the magnetic field is applied, suggesting an existence of the MR effect. The resistivity peak at T_P shifts to higher temperatures with increasing magnetic field.

The nature of the conduction in the metallic regime ($T<T_P$) of the $La_{0.7}Ca_{0.3}Mn_{1-x}Ni_xO_3$ samples, both in H = 0 T and $H \neq 0$ T, can be examined by means of the equation $\rho(T) = \rho_0 + \rho_2 T^2 + \rho_{4.5} T^{4.5}$ [4-71]. In this equation ρ_0 corresponds to the temperature-independent residual resistivity due to domain and grain boundaries, $\rho_2 T^2$ describes the resistivity associated to electron-electron scattering, and $\rho_{4.5} T^{4.5}$ is a term associated with electron-magnon scattering processes due to spin waves. Fig. 3-38 shows the experimental $\rho(T)$ data and the fitting curves for $La_{0.7}Ca_{0.3}Mn_{1-x}Ni_xO_3$ (x = 0, 0.02, 0.07, 0.1) samples processed by means of CS and SSR below T_P at H = 0 and 1.25 T. The good correspondence between the experimental data and the fitting function suggests that the transport mechanism in the metallic regime of the concerned samples is governed by the electron-electron and electron-magnon scattering [4-72]. From the fitting curves the ρ_0, ρ_2 and $\rho_{4.5}$ values for $La_{0.7}Ca_{0.3}Mn_{1-x}Ni_xO_3$ (x = 0, 0.02, 0.07, 0.1) samples processed by means of CS and SSR are obtained and the results are listed in Table 3-6.

Figure 3-38: Representative *ρ(T)* data measured on $La_{0.7}Ca_{0.3}Mn_{1-x}Ni_xO_3$ samples with x = 0, x = 0.02, x = 0.07 and x = 0.1 processed by means of CS and SSR below T_P at H = 0 and 1.25 T. The solid lines represent fitting of the equation $\rho(T) = \rho_0 + \rho_2 T^2 + \rho_{4.5} T^{4.5}$ to the experimental data.

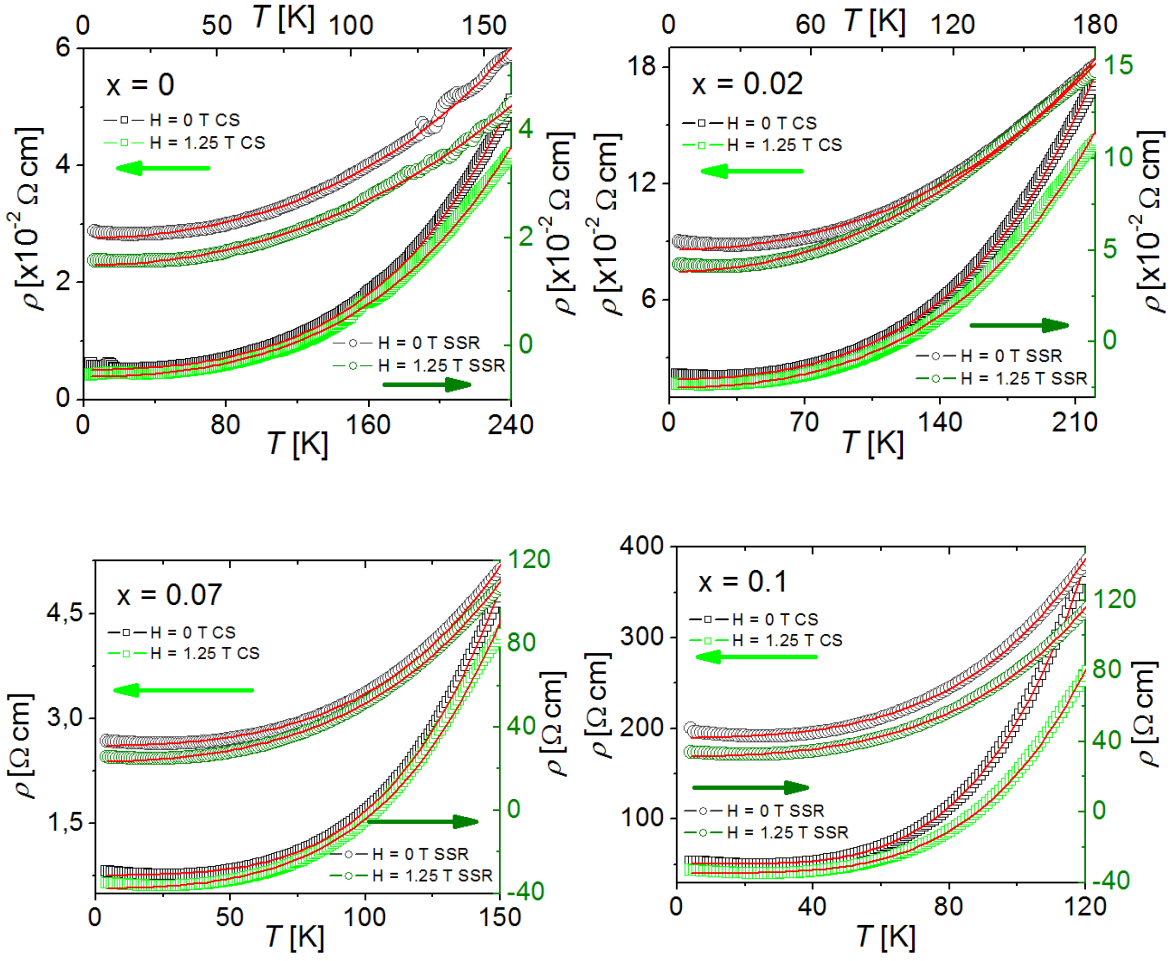

Table 3-6: ρ_0, ρ_2 and $\rho_{4.5}$ values for $La_{0.7}Ca_{0.3}Mn_{1-x}Ni_xO_3$ (x = 0, 0.02, 0.07, 0.1) samples obtained by means of CS and SSR resulting from the fitting function $\rho(T) = \rho_0 + \rho_2 T^2 + \rho_{4.5} T^{4.5}$ below T_P at H = 0 and 1.25 T plotted in Fig. 3-38.

			$\rho(T) = \rho_0 + (\rho_2 * T^2) + (\rho_{4.5} * T^{4.5})$					
			ρ_0	±	ρ_2	±	$\rho_{4.5}$	±
CS	x = 0	H = 0 T	0,0051	0,00003	2,79E-07	2,79E-09	8,98E-12	5,34E-14
	x = 0.02		0,0190	0,00014	1,27E-06	1,79E-08	4,10E-11	4,06E-13
	x = 0.07		0,7561	0,00335	2,00E-05	9,04E-07	7,24E-09	4,40E-11
	x = 0.1		50,2934	0,25846	5,00E-04	1,10E-04	1,63E-06	8,08E-09
	x = 0	H = 1.25 T	0,0039	0,00005	3,35E-07	5,18E-09	6,04E-12	9,90E-14
	x = 0.02		0,0047	0,00018	1,36E-06	2,25E-08	2,85E-11	5,11E-13
	x = 0.07		0,5683	0,0076	4,00E-05	2,05E-06	5,57E-09	9,96E-11
	x = 0.1		39,7958	0,27204	7,60E-04	1,10E-04	1,03E-06	8,50E-09
SSR	x = 0	H = 0 T	0,0200	0,00008	9,99E-07	2,02E-08	1,48E-11	8,65E-13
	x = 0.02		0,0502	0,00025	2,35E-06	4,73E-08	2,67E-11	1,61E-12
	x = 0.07		30,9845	0,1333	1,46E-03	4,00E-05	1,06E-07	1,75E-09
	x = 0.1		41,9109	0,23609	2,18E-03	1,00E-04	3,36E-07	7,38E-09
	x = 0	H = 1.25 T	0,0149	0,00007	9,99E-07	1,60E-08	6,17E-12	6,87E-13
	x = 0.02		0,0381	0,00024	3,32E-06	4,55E-08	5,58E-12	1,55E-12
	x = 0.07		23,4145	0,1475	1,98E-03	4,00E-05	8,27E-08	1,93E-09
	x = 0.1		31,2487	0,17568	2,33E-03	7,00E-05	2,45E-07	5,49E-09

In the high temperature region ($T > T_P$), the conduction process of the studied samples is well described by the small polaron hopping transport mechanism [4-73]. In this model the dependence of the resistivity on the temperature is mathematically represented by the relation $\rho(T) = \rho_0 T exp\left(E_a/k_B T\right)$, being ρ_0 a temperature independent coefficient, k_B the Boltzmann´s constant and E_a the activation energy of the polarons [4-74]. This function was fitted to the experimental resistivity data above T_P $La_{0.7}Ca_{0.3}Mn_{1-x}Ni_xO_3$ (x = 0, 0.02, 0.07, 0.1) samples obtained by means of CS and SSR methods. The resulting fitting curves are indicated by the solid lines in Fig. 3-38. A good concordance between the experimental data and the fitting function is clearly observed in these plots. Based on the best fit parameters, the E_a values were determined. The results are plotted in the Fig. 3-

39, in which is show that the E_a values increase upon an increase in the Ni^{2+}-content. Carrier´s localization resulting from the electron-phonon interaction has been proposed as possible mechanism behind the increase of E_a [4-75]. Consequently, higher energies will be required to create free carriers. In this context, results of measurements on $La_{0.7}Sr_{0.3}Mn_{1-x}Ni_xO_3$ (x = 0, 0.025, 0.050, 0.075) ceramics have shown that the small-polaron coupling interaction (γ_{ph}), which is a measurement of electron-phonon interaction, increases with Ni^{2+} content [4-75]. Moreover, it has been established that strong electron-phonon interaction can occurs for $\gamma_{ph} > 4$ [4-76]. This requirement was verified for the $La_{0.7}Sr_{0.3}Mn_{1-x}Ni_xO_3$ samples reported in Ref. [4-75]. The increase of E_a upon an increase in the Ni^{2+}-content can also be explained by considering the downsizing of the particle with an increase in the Ni^{2+}-content as verified by XRD analysis [Fig. 3-1]. Although the downsizing of the particle may increase the interconnectivity between grains during the sintering process, the number of grain boundaries increases considerably in nano-sized systems. This, in turn, will hamper the possibility of conduction electron to hop the neighboring sites [4-77]. Thus, the conduction bandwidth will decrease and as a result, the value of E_a will increase. The results reported in this thesis suggests that the conduction bandwidth of the materials may be modified by tuning their particle size. Similar conclusions have been drawn from studies on other manganites prepared by means of chemical methods such as a citrate gel technique [4-78].

Figure 3-39: Temperature dependence of the resistivity of $La_{0.7}Ca_{0.3}Mn_{1-x}Ni_xO_3$ (x = 0, 0.02, 0.07, 0.1) samples above T_P at H = 0 and H = 1.25 T magnetic fields synthesized by means of CS and SSR fitted with the polaron transport model.

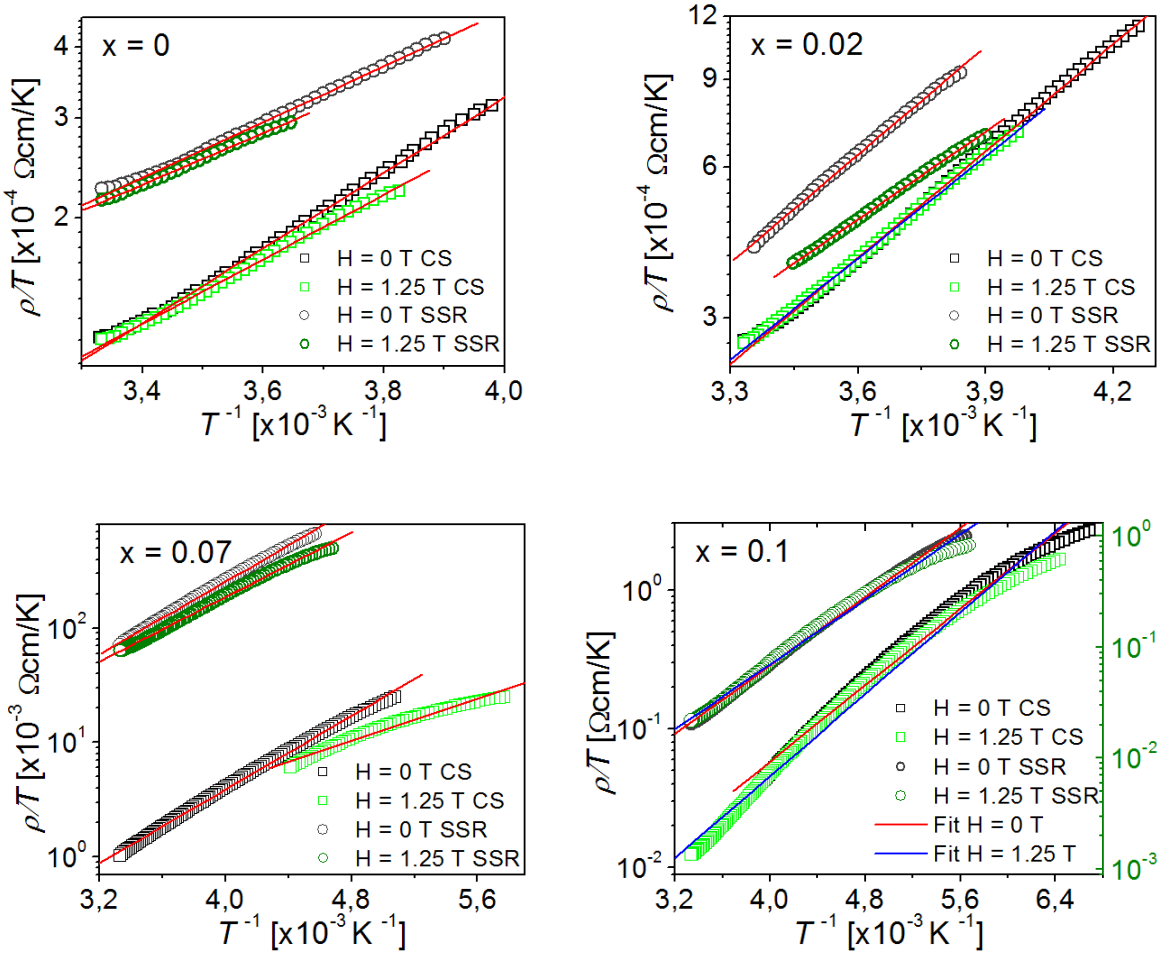

Figure 3-40: Activation energy of the polarons as a function of the Ni^{2+}-content for the samples plotted in the Fig. 3-39.

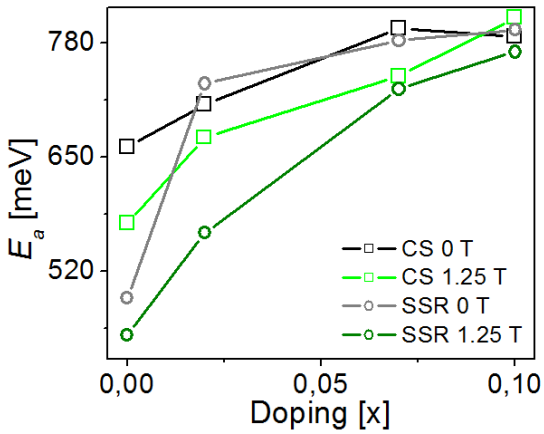

It is noted in the Fig. 3-40 that the maximum activation energy values tends to a close values whenever the Ni^{2+}-doping level increase, independently that the process used to synthesize the samples.

Certainty, the MR effect can be ascribed to the orientation of the spins in the different domain due to the presence of the magnetic field. When the spins system is oriented, the carrier scattering during hopping processes is eliminated [4-75]. Fig. 3-41 shows the dependence of the MR on the temperature, recorded at H = 1.25 T, for $La_{0.7}Ca_{0.3}Mn_{1-x}Ni_xO_3$ (x 0, 0.02) samples synthesized by means of CS process. Two MR effects are observed in the MR(T) curves of the studied samples. The first one occurs near T_P, with 45 % maximum *MR* values for H = 1.25 T. This *MR* is due to the DE interaction of Mn^{3+}–Mn^{4+} pairs [4-79]. The other notable variation occurs at low temperatures below ~ 100 K. In this region, the *MR* values increases with decreasing temperature resembling the *MR* spin-polarized tunneling effect in a granular ferromagnetic systems [4-80]. This behavior can be described by a Curie-Weiss law-like, $a+b/(c+T)$ [4-81]. The inset of Fig. 3-41 shows the fitting of the law $a+b/(c+T)$ to the experimental data for the samples in the main panel. The corresponding *a, b* and *c* parameters are listed in Table 3-7. It is also noteworthy to note that the *MR* value near the peak of the pristine and the 2 % Ni^{2+}-doped LCMO samples does not show a significant change at H = 1.25 T. Both samples show sharp and equally intense peak around T_C. The insensitivity of the *MR* to the 2 % Ni^{2+}-doped is observed even at higher field [Fig. 3-41 (upper and bottom right panels)].

Figure 3-41: Variation of the *MR* with the temperature at H = 1.25 T for $La_{0.7}Ca_{0.3}Mn_{1-x}Ni_xO_3$ samples with x = 0 and x = 0.02 obtained by means of CS. Inset: *MR*(T) data for T < 120 K fitted to a Curie-Weiss law-like $a+b/(c+T)$. The solid lines in the inset correspond to the fitting curves.

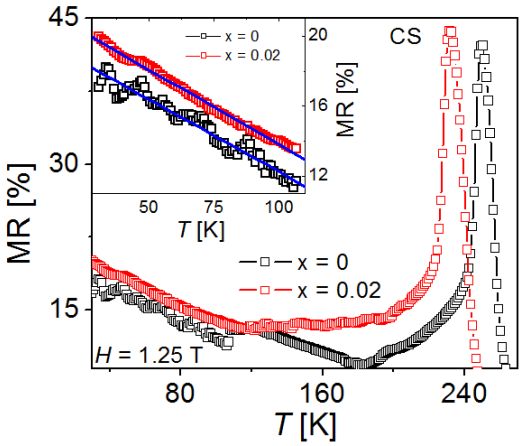

Figure 3-42 shows the dependence of the *MR* on the temperature, recorded at *H* = 1.25, *H* = 2.5 and *H* = 5 T, for $La_{0.7}Ca_{0.3}Mn_{1-x}Ni_xO_3$ (x = 0, 0.02) samples synthesized by means of CS (upper panels) and SSR processes (bottom panels). In these plots it is possible to observe that the peak temperatures (T_P) are the same or independent of the applied magnetic field strength in every composition does not occurring the same with the broadening of the peak, it which increase with increasing the magnetic field. The T_P values for the maximum *MR* obtained in $La_{0.7}Ca_{0.3}Mn_{1-x}Ni_xO_3$ (x = 0, 0.02) samples processed by means of CS and SSR (in brackets) at *H* = 1.25, *H* = 2.5 and *H* = 5 T are 251 (256), 232 (257) K, respectively.

Figure 3-42: Variation of the *MR* with the temperature under fields *H* = 1.25, *H* = 2.5 and *H* = 5 T, for $La_{0.7}Ca_{0.3}Mn_{1-x}Ni_xO_3$ (x = 0, 0.02) samples synthesized by means of CS (upper panels) and SSR processes (bottom panels).

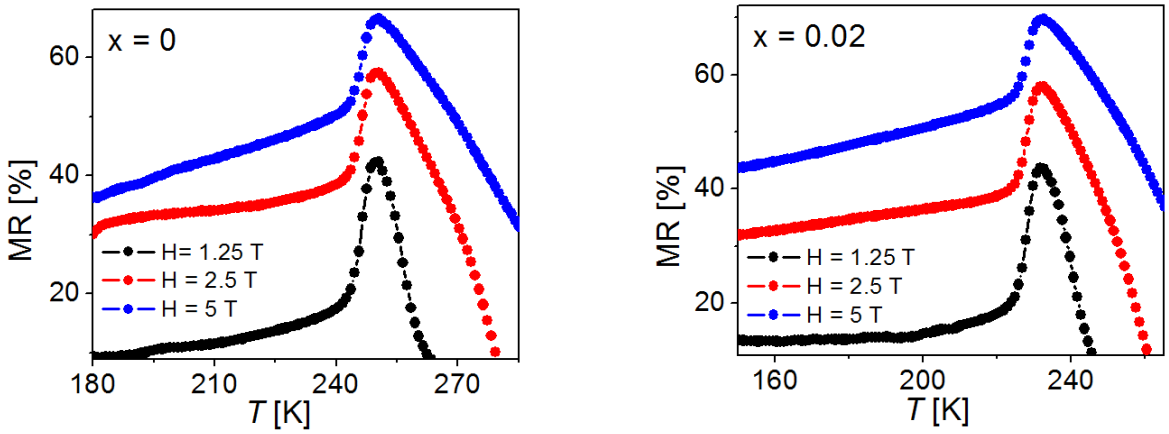

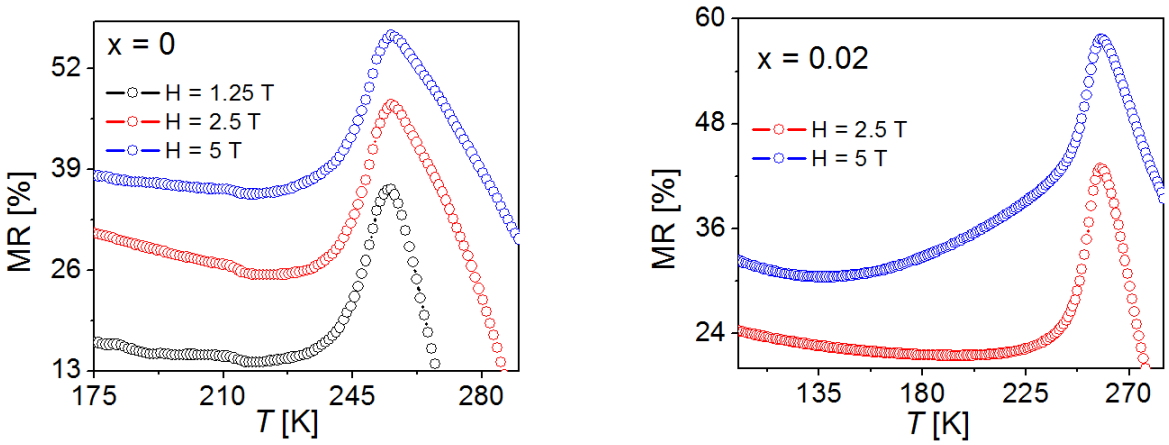

It is evident that the *MR* of the samples synthesized by CS is higher than that of the samples obtained by SSR. Generally speaking, it is expected that a substantial contribution by the grain boundaries is present in these nanometric-sized systems [14].

The results shown in Fig. 3-40, Fig. 3-41 and Fig. 3-42 demonstrate that *MR* of LCMO is not affected much by Ni^{2+}-doped levels as high as 2 %. Nevertheless, a significant increase in the *MR* value is verified for higher Ni^{2+}-doped levels. The increase of the *MR* value with an increase in the Ni^{2+}-content may be explained considering the concomitant reduction of the particle size of the doped samples. Thus, the later results suggests that manganites having nanometer-sized particles can exhibit large *MR* around T_C that the ones with higher particles size. This is directly verified by comparing the samples prepared for two different routes, namely combustion solution and standard solid state reaction. As it is widely known, the grain size of LCMO samples synthesized by the physical method is at least double than the auto combustion process.

Figure 3-43: Variation of maximum *MR* values as a function of the magnetic field for $La_{0.7}Ca_{0.3}Mn_{1-x}Ni_xO_3$ (x = 0, 0.02, 0.07, 0.1) samples obtained by means of CS and SSR. Inset: *MR* versus Ni^{2+}-content recorded at *H* = 1, 1.5 and 3 T for the samples in the main panel.

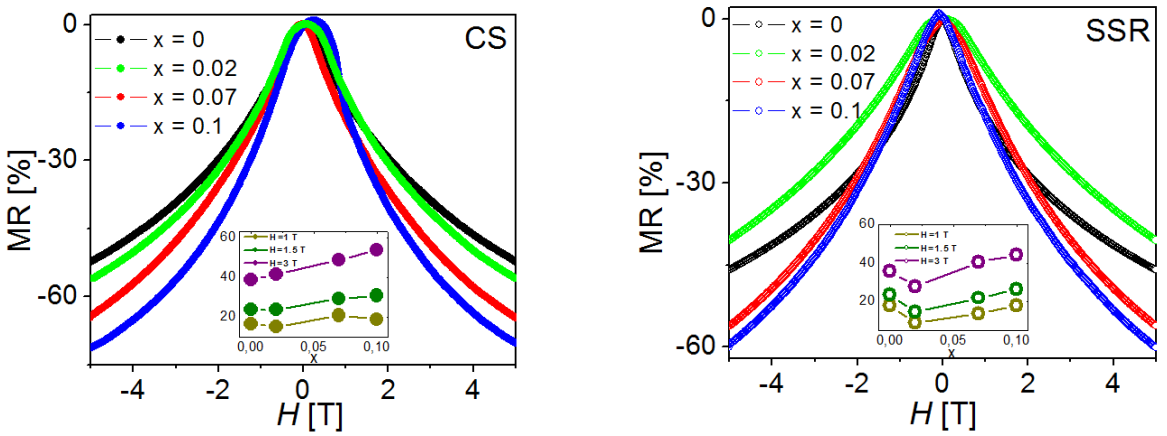

The dependence of the MR on the external magnetic field at different temperatures for the $La_{0.7}Ca_{0.3}Mn_{1-x}Ni_xO_3$ (x = 0, 0.02, 0.07, 0.1) samples is displayed in Fig. 3-44. It is observed in this plot that the highest value of MR occurs around the T_C of each sample as already seen in Fig. 3-41. It is also verified that the MR decreases after the transition pass by T_P and starts to increase at T < 100 K. Interestingly, a sharp increasing nature of the magnitude of the MR is observed at low temperatures within a narrow range of magnetic field strengths (H ± 1 T). At higher field (H > 1 T) the variation of the MR is slower and almost linear with increasing magnetic field. As previously mentioned, the behavior of the MR at low temperatures resembles that of typical ferromagnetic granular material at low temperature. Indeed, the sharp drop of the MR can be explained by taken the intergranular spin polarized tunneling of electrons near the grain boundaries into account. This kind of MR is known as extrinsic MR and, in general, the extrinsic nature of MR is frequently found at low magnetic fields [4-m]. However, it has been argued that the high-field response is also due to the existence of the grain boundary [4-n]. The nature of the grain boundary is the key ingredient in this electrical transport mechanism as it constitutes the barrier through which carrier tunnel. The application of an external magnetic field brings about the movement of magnetic domain walls through the grain boundaries. This movement is associated with the progressive alignment of magnetic domains and as a result, a sharp drop of MR at low fields is commonly observed [4-n].

Figure 3-44: *MR*(*H*) curves at different temperatures for $La_{0.7}Ca_{0.3}Mn_{1-x}Ni_xO_3$ (x = 0, 0.02, 0.07, 0.1) samples obtained by means of CS (left panels) and SSR (right panels).

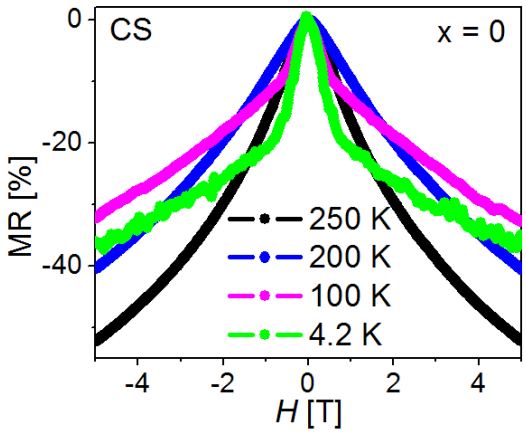
CS
x = 0
MR [%]
H [T]
250 K
200 K
100 K
4.2 K

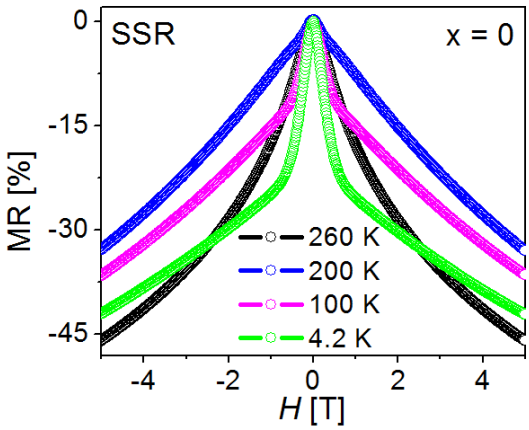
SSR
x = 0
MR [%]
H [T]
260 K
200 K
100 K
4.2 K

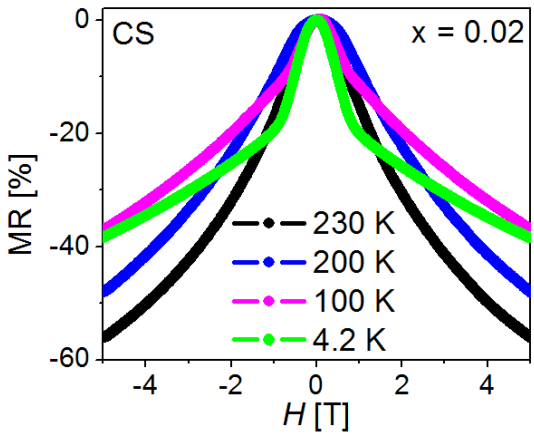
CS
x = 0.02
MR [%]
H [T]
230 K
200 K
100 K
4.2 K

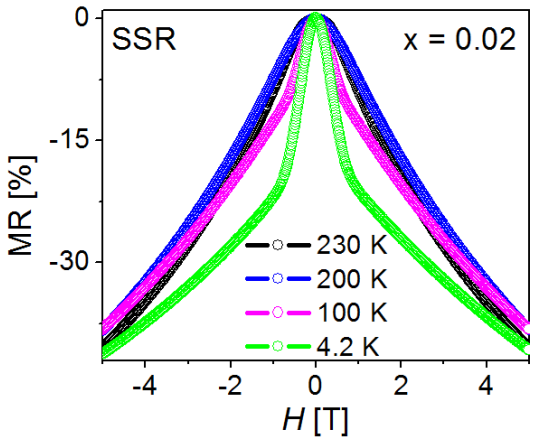
SSR
x = 0.02
MR [%]
H [T]
230 K
200 K
100 K
4.2 K

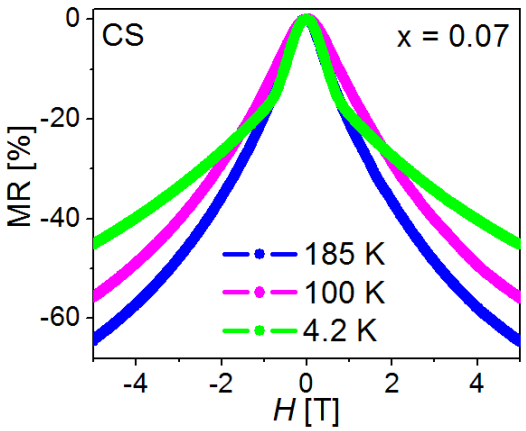
CS
x = 0.07
MR [%]
H [T]
185 K
100 K
4.2 K

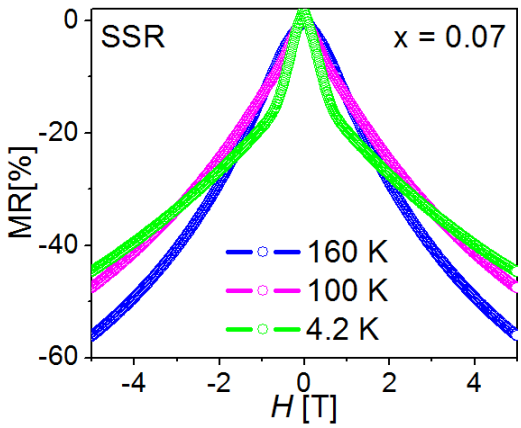
SSR
x = 0.07
MR[%]
H [T]
160 K
100 K
4.2 K

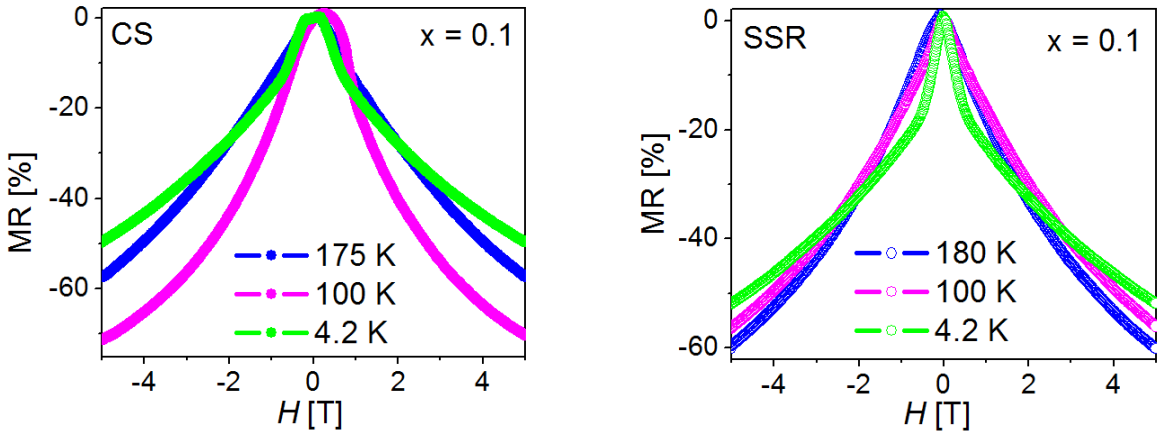

Figure 3-45 shows the variation of the MR with the external magnetic field for the $La_{0.7}Ca_{0.3}Mn_{1-x}Ni_xO_3$ (x = 0, 0.02, 0.07 0.1) samples processed by means of CS and SSR at different temperatures. It is observed that the MR value for Ni^{2+}-doped samples, at $H \geq$ 1 T, is higher than that of the pristine LCMO samples (the lower MR value seen for the samples with x = 0.1 and x = 0.02 at 200 K synthesized by means of CS and SSR, respectively, is due to its reduced T_C ~170 and 185 K, respectively). The improvement of the MR with the Ni^{2+}-doping at low magnetic fields (H = 1 T) and temperatures around T_C has been already corroborated [inset of Fig. 3-43]. These results indicate that the MR of LCMO can be considerable improved upon Ni^{2+}-doping. It is evident that the MR value depends on the temperature and the magnetic field strength. The increased MR value at low fields (H = 1 T) and $T \approx T_C$, as compared to the pristine LCMO, suggests a higher magnetic field sensitivity of the Ni^{2+}-doped samples due to enhanced tunneling of electrons between two grains through the grain boundary. In the pristine LCMO samples, the electrons are spin polarized in the LCMO grains and charge transport occurs between Mn ions. In the case of Ni^{2+}-doped samples the downsizing of particle leads to an increased number of grain boundaries. Consequently, the higher spin dependent scattering takes place at the grain boundaries resulting in higher resistivity as previously observed in the Fig. 3-37 (upper left panel). When an external magnetic field is applied, the domains are aligned and therefore the spin disorder near the grain boundary region reduced. Hence, the spin polarized tunneling is enhanced, which results both in higher MR values and higher magnetic field sensitivity of the Ni^{2+}-doped LCMO samples.

Figure 3-45: Variation of the *MR* with the external magnetic field for $La_{0.7}Ca_{0.3}Mn_{1-x}Ni_xO_3$ (x = 0, 0.02, 0.07, 0.1) samples synthesized by means of CS and SSR at different temperatures.

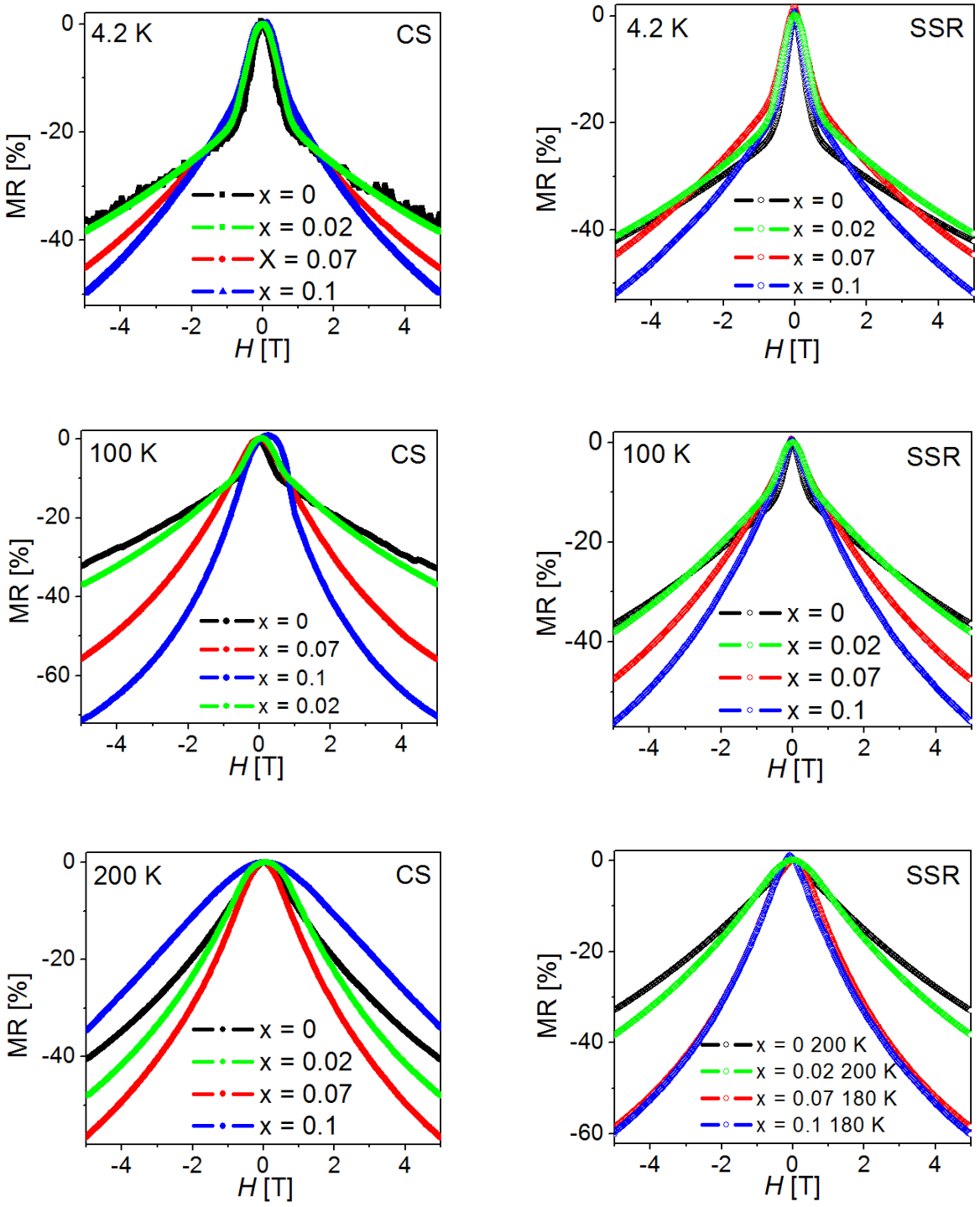

It is a known fact that magnetic entropy is also a parameter usually used to characterize magnetic order [4-o]. By taking into account that the magnetic disorder has a strong effect on the resistivity behavior of the manganites, a clear relation between ΔS_M and resistivity is expected [4-p]. This is certainly verified for the LCMO samples synthesized by the CS and SSR processes. The qualitative relation between these two quantities is seen in Fig. 3-46 for the pristine LCMO sample.

Figure 3-46: Qualitative relation between ΔS_M and resistivity (red) as a function of temperature for $La_{0.7}Ca_{0.3}Mn_{1-x}Ni_xO_3$ (x = 0, 0.02, 0.07, 0.1) samples synthesized by means of CS and SSR.

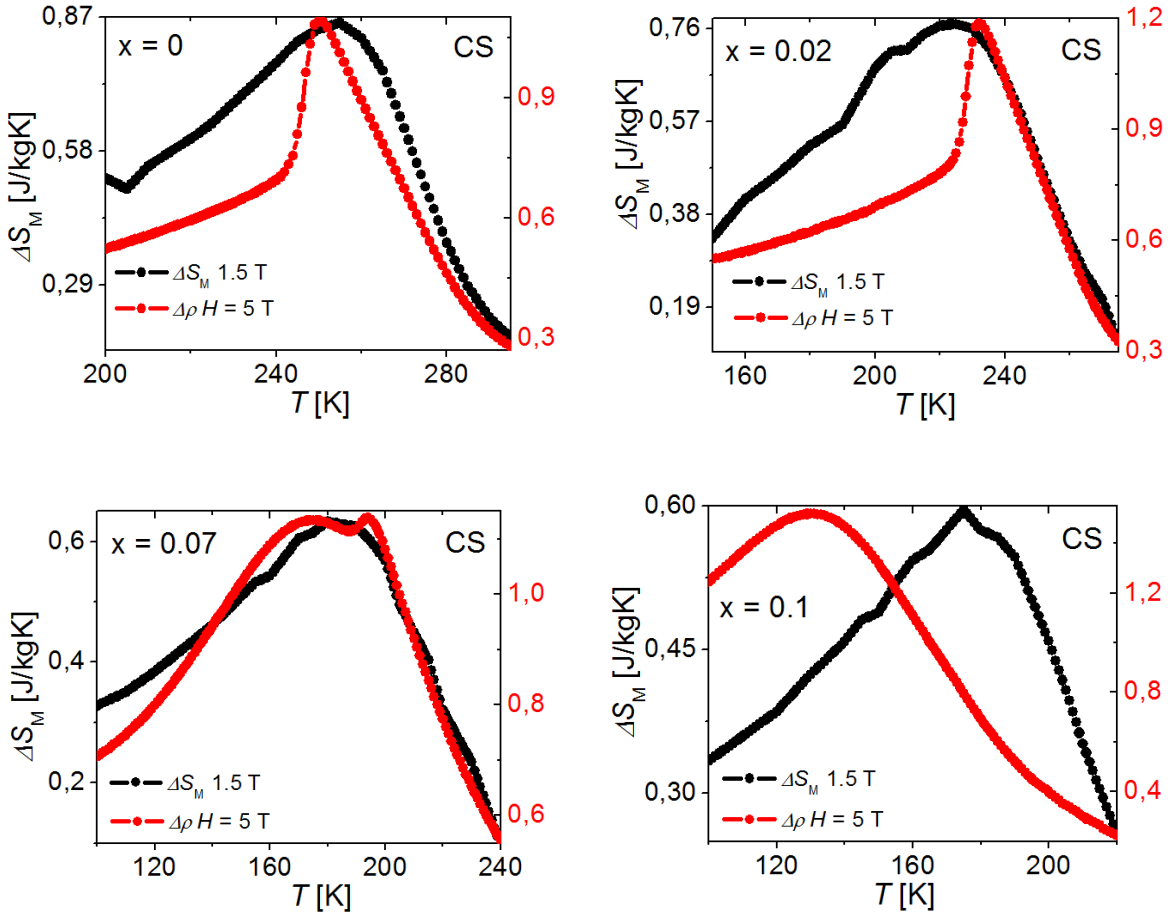

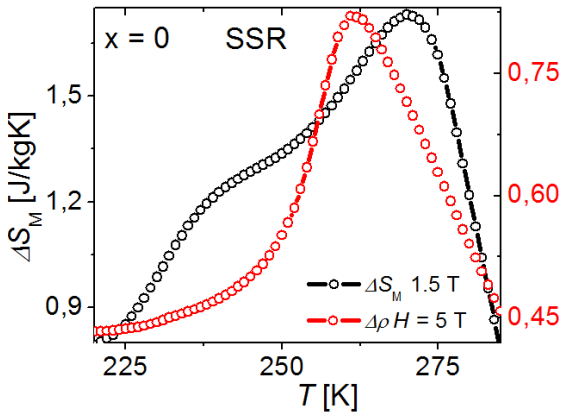
x = 0
SSR
ΔS_M [J/kgK]
T [K]
ΔS_M 1.5 T
Δρ H = 5 T

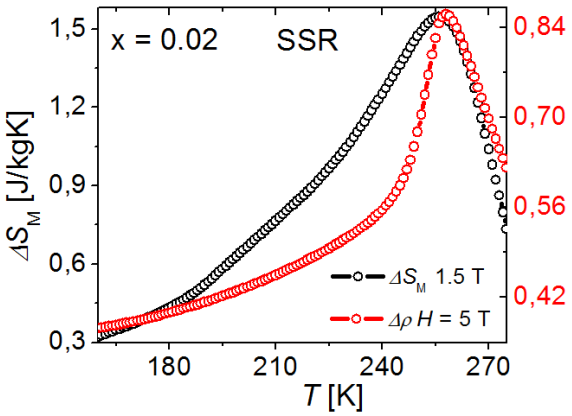
x = 0.02
SSR
ΔS_M [J/kgK]
T [K]
ΔS_M 1.5 T
Δρ H = 5 T

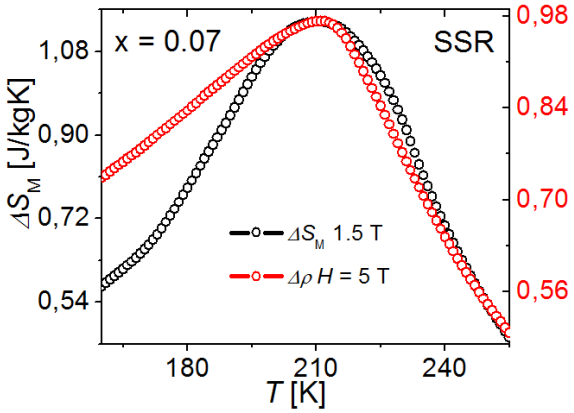
x = 0.07
SSR
ΔS_M [J/kgK]
T [K]
ΔS_M 1.5 T
Δρ H = 5 T

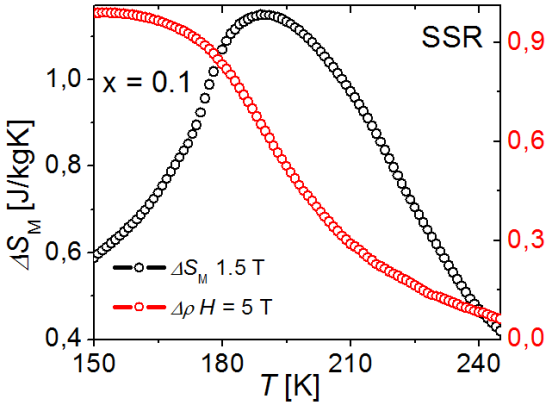
x = 0.1
SSR
ΔS_M [J/kgK]
T [K]
ΔS_M 1.5 T
Δρ H = 5 T

4. Conclusions and perspectives

$La_{0.7}Ca_{0.3}Mn_{1-x}Ni_xO_3$ (x = 0, 0.02, 0.07, 0.1) manganites were synthesized *via* the auto-combustion and standard solid state reaction processes, and their structural, magnetic, and magnetocaloric properties were carefully studied. It was demonstrated that auto-combustion is a fast, effective, and low-cost synthesis route for obtaining high-quality powders of novel oxide materials. All the cell parameters and the unit cell volumes of the $La_{0.7}Ca_{0.3}Mn_{1-x}Ni_xO_3$ samples increased with an increase in the Ni^{2+} content, due to the large ionic size of these ions compared with those of Mn^{3+} and Mn^{4+}. It was verified that both the magnetic and magnetocaloric properties of the parent LCMO can be controlled through substitution of Mn^{3+} with Ni^{2+} ions. The T_C of LCMO shifted to lower temperatures, probably due to the decrease in the ferromagnetic DE interactions. The observed SOPT in the parent LCMO sample could be attributed to the effects of the particle size reduction. The inverse DC magnetic susceptibility data fit well to the Curie–Weiss law, indicating typical paramagnetic behavior above the T_C. The effective paramagnetic moments were evaluated both experimentally and theoretically. The experimental moment increased upon Ni^{2+} addition, which is not in a manner consistent with the behavior of the T_C. The ΔS_{max} shifted towards lower temperatures with a small change in the amplitude upon Ni^{2+} addition. Interestingly, it was verified that the RCP values of the Ni^{2+}-doped samples increased compared with that of the parent LCMO. The highest RCP value (~60 J/kg) was observed for the sample with a Ni^{2+}-doping level of 2 % around 230 K at 1.5 T applied magnetic field. The achieved results suggest that the studied Ni^{2+}-doped LCMO manganites are materials with potential to be used in magnetic refrigeration applications over a wide range of operation temperatures.

The observed increase in the value of the resistivity with the Ni^{2+} doping can be attributed to the DE decrease, which hampers the movement of the eg band electron of Mn. The resistivity in the ferromagnetic metallic region seemed to be determined by grain

boundary effects, electron-electron scattering, and electron-magnon scattering processes. In the high temperature region ($T > T_C$), the conduction process was explained by the small polaron hopping transport mechanism. Here, the polaron activation energy increased with an increase in the Ni^{2+} content, which could be related to the downsizing of the particles upon Ni^{2+} doping. In general, the application of an external magnetic field drove the metal-insulator transition to higher temperatures and largely depressed the resistivity values. The MR values exhibited maximum values around *Tp*. MR measurements showed an enhanced field sensitivity for the Ni^{2+}-doped samples as compared to the pristine LCMO ones. In general, the electrical and MR properties of the $La_{0.7}Ca_{0.3}Mn_{1-x}Ni_xO_3$ samples can be explained by the increase in the scattering of the conduction electrons near the grain boundaries. The results suggest that $La_{0.7}Ca_{0.3}Mn_{1-x}Ni_xO_3$ may be regarded as a potential candidate for application in low-field MR devices due to its enhanced magnetic field sensitivity. The MR and ΔS_M peaks appeared simultaneously, suggesting a close relationship between the change in resistivity and magnetic entropy. Nevertheless, the detailed temperature dependence of MR and ΔS_M seemed to be different. Additional factors in the MR mechanism, other than spin disorder suppression, should be taken into account to explain the difference in the behavior of these quantities. The correlation between magnetocaloric and magnetotrasport properties in manganites is an interesting and ongoing theme in condensed matter and deserves additional work and closer analysis.

A detailed investigation of the magnetic properties and critical exponents of polycrystalline $La_{0.7}Ca_{0.3}Mn_{1-x}Ni_xO_3$ (x=0, 0.02, 0.07, 0.1) compound synthesized by auto-combustion was carried out. The value of the critical exponents, corresponding to the PM to FM phase transition, was extracted using the modified Arrott plot method, Kouvel-Fisher method and critical isothermal analysis. The estimated critical exponents confirmed that the experimental data agreed well with the mean-field model. A relatively high change of the entropy was observed at low magnetic fields.

References

[1] Y. Tokura, N. Nagaosa, Science 462 (2000) 288.

[2] E. Dagotto, T. Hotta, A. Moreo, Phys. Rep. 344 (2001) 1.

[3] J. Hemberger, M. Brando, R. Wehn, V.Yu. Ivanov, A.A. Mukhin, A.M. Balbashov, A. Loidl, Phys. Rev. B 69 (2004) 064418.

[4] P. Lampen, N. S. Bingham, M.H. Phan, H. Kim, M. Osofsky, A. Piqué, T.L. Phan, S.C. Yu, H. Srikanth, Appl. Phys. Lett. 102 (2013) 062414.

[5] I. Hussain, M. S. Anwar, E. Kim, B. H. Koo, C. G. Lee, Korean J. Mater. Res. 26 (2016) 623.

[6] L. W. Zhang, G. Feng, H. Liang, B. S. Cao, Z. Meihong, Y. G. Zhao, J. Magn. Magn. Mater. 219 (2000) 236.

[7] T-Long Phan, P. Zhang, T. D. Thanh, S. C. Yu, J. Appl. Phys. 115 (2014) 17A912.

[8] B. Chen, C. Uher, D. T. Morelli, J. V. Mantese, A.M. Mance, A. L. Micheli, Phys. Rev. B 53 (1996) 5094.

[9] S. Raj, H. C. Padhi, P. Raychaudhury, A. K. Nigam, R. Pinto, M. Polasik, F. Pawlowski, D. K. Basa, Nucl. Instrum. Methods Phys. Res. B 174 (2001) 344.

[10] D. N. H. Nam, N. V. Dai, L. V. Hong, N.X. Phuc, S. C. Yu, M. Tachibana, E. Takayama-Muromachi, J. Appl. Phys. 103 (2008) 043905.

[11] N. A. de Olivira, P. J. Von Ranke, Phys. Rep. 489 (2010) 89.

[12] M. H. Phan, S. C. Yu, J. Magn. Magn. Mater. 308 (2007) 325.

[13] A. M. Tishin, Y. I. Spichkin, The Magnetocaloric Effect and Its Applications, IOP Publishing Ltd., Bristol, 2003.

[14] A. Marzouki-Ajmi, M. Mansouri, W. Cheikhrouhou-Koubaa, M. Koubaa, A. Cheikhrouhou, J. Magn. Magn. Mater. 433 (2017) 209.

[15] X. K. Hu, M. H. Xu, Z. S. Wang, S. Y. Zhang, Q. Wu, P. Z. Si, Solid State Commun. 149 (2009) 246.

[16] A. Maignan, F. Damay, C. Martin, B. Raveau, Mater. Res. Bull. 32 (1997) 965.

[17] S. Liu, Y. Bian, T. Wang, L. Yang, X. Song, J. Zhang, Rev. Adv. Mater. Sci. 33 (2013) 137.

[18] A. M. Ahmed, M. A. Abedellateef, H. A. Abd El-Ghanny, A. A. Mohamed, Phys. Status Solidi A 212 (2015) 623.

[19] A. El-Moez, A. Mohamed, B. Hernando, A. M. Ahmed, J. Alloys Compd. 692 (2017) 381.

[20] F. Chen, H. W. Liu, K. F. Wang, H. Yu, S. Dong, X. Y. Chen, X. P. Jiang, Z. F. Ren, J. M. Liu, J. Phys. Condens. Matter 17 (2005) L467.

[21] P. Katiyar, D. Kumar, T. K. Nath, A. V. Kvit, J. Narayan, S. Chattopadhyay, W. M. Gilmore, S. Coleman, C. B. Lee, J. Sankar, Appl. Phys. Lett. 79 (2001) 1327.

[22] R. D. Sánchez, J. Rivas, C. Vázquez-Vázquez, A. López-Quintela, M.T. Causa, M. Tovar, S. Oseroff, Appl. Phys. Lett. 68 (1996) 134.

[23] P. K. Siwach, H. K. Singh, O. N. Srivastava, J. Phys. Condens. Matter 20 (2008) 273201.

[24] V. Provenzano, A. J. Shapiro, R. D. Shull, Nature 429 (2004) 853.

[25] O. Gutfleisch, M. A. Willard, E. Bruck, C. H. Chen, S. G. Sankar, J. P. Liu, Adv. Mater. 23 (2011) 821.

[26] A. Varma, A. S. Rogachev, A. S. Mukasyan, S. Hwang, Adv. Chem. Eng. 24 (1998) 79.

[27] A. M. Segadaes, M. R. Morelli, R. G. A. Kiminami, J. Eur. Ceram. Soc. 18 (1988) 771.

[28] D. A. Fumo, J. R. Jurado, A. M. Segadaes, J. R. Frade, Mater. Res. Bull. 32 (1997) 1459.

[29] Y. H. Liu, B. X. Huang, R. Z. Zhang, X. B. Yuan, C. J. Wang, L.M. Mei, J. Magn. Magn. Mater. 269 (2004) 398.

[30] A. El-Moez, A. Mohamed, B. Hernando, A. M. Ahmed, Solid State Commun. 233 (2016) 15.

[31] K. Park, J. Am. Ceram. Soc. 88 (2005) 862.

[32] J. W. Feng, C. Ye, L.-P. Hwang, Phys. Rev. B 61 (2000) 12271.

[33] J. A. Fernandez-Beca, P. Dai, H. Kawano-Furukawa, H. Yoshizawa, E.W. Plummer, S. Katano, T. Tomioka, Y. Tokura, Phys. Rev. B 66 (2002) 054434.

[34] O. Morán, R. Hott, D. Fuchs, K. Grube, R. Schneider, E. Baca, W. Saldarriaga, P. Prieto, J. Appl. Phys. 95 (2004) 6239.

[35] A. M. Ahmed, A. El-Moez, A. Mohamed, M. A. Abdellateef, H. A. El-Ghanny, Rare Met. 35 (2016) 551.

[36] L. Damari, J. Pelleg, G. Gorodetsky, Ch. Koren, V. Markovich, A. Shames, X. Wu, D. Mogilyanski, I. Fita, A. Wisniewski, J. Appl. Phys. 106 (2009) 013913.

[37] M. C. Sánchez, J. García, J. Blasco, G. Subías, J. P. Cacho, Phys. Rev. B 65 (2002) 144409.

[38] A. Gaur, G. D. Varma, J. Phys. Condens. Matter 18 (2006) 8837.

[39] B. Arun, M. V. Suneesh, M. Vasundhara, J. Magn. Magn. Mater. 418 (2016) 265.

[40] I. A. Serrano, C. Pico, M. L. Veiga, Solid State Sci. 6 (2004) 1321.

[41] K. Wang, W. Song, T. Yu, B. Zhao, M. Pu, Y. Sun, Phys. Status Solidi (a) 171 (1999) 577.

[42] M. Sugantha, R. S. Singh, A. Guha, A. K. Raychaudhuri, C. N. R. Rao, Mater. Res. Bull. 33 (1998) 1134.

[43] P. Thamilmaran, M. Arunachalam, S. Sankarrajan, K. Sakthipandi, J. Magn. Magn. Mater. 396 (2015) 181.

[44] Y. D. Zhang, T. L. Phan, T. S. Yang, S. C. Yu, Curr. Appl. Phys. 12 (2012) 803.

[45] O. Toulemonde, F. Studer, B. Raveau, Solid State Commun. 118 (2001) 107.

[46] T. S. Zhao, W. X. Xianyu, B. H. Li, Z. N. Qian, J. Alloys Compd. 459 (2008) 29.

[47] I. O. Troyanchuk, N. V. Samsonenko, A. Nabiaiek, H. Szymczak, J. Magn. Magn. Mater. 168 (1997) 309.

[48] S. Pal, E. Bose, B. K. Chaudhuri, H. D. Yang, S. Neeleshwar, Y. Y. Chen, J. Magn. Magn. Mater. 293 (2005) 872.

[49] C. N. R. Rao, B. Raveau, Colossal Magnetoresistance, Charge Ordering and the Related Properties of Manganese Oxides, first ed., World Scientific Pub. Co. Inc., 1998.

[50] H. Y. Hwang, T. T. M. Palstra, S. W. Cheong, B. Batlogg, Phys. Rev. B 52 (1995) 15046.

[51] M. H. Phan, N. Duc Tho, N. Chau, S. C. Yu, M. Kurisu, J. Appl. Phys. 97 (2005) 10390.

[52] T. Sarkar, A. K. Raychaudhuri, A. K. Bera, S. M. Yusuf, New J. Phys. 12 (2010) 123026.

[53] L. E. Hueso, P. Sande, D. R. Miguens, J. Rivas, F. Rivadulla, M.A. Lopez-Quintela, J.Appl. Phys. 91 (2002) 9943.

[54] D. H. Manh, P. T. Phong, T. D. Thanh, D. N. H. Nam, L.V. Hong, N.X. Phuc, J. Alloys Compd. 509 (2011) 1373.

[55] B. Roy, A. Poddar, S. Das, J. Appl. Phys. 100 (2006) 104318.

[56] Y. A. Soh, G. Aeppli, N. D. Mathur, M. G. Blamire, Phys. Rev. B 63 (2000) 020402.

[57] M. Egilmez, K. H. Chow, J. Jung, Appl. Phys. Lett. 92 (2008) 162515.

[58] W. Jiang, X. Z. Zhou, G. Williams, Y. Mukovskii, K. Glazyrin, Phys. Rev. B 77 (2008) 064424.

[59] R. Skini, M. Khlifi, M. Jemmali, E. Dhahri, E. K. Hlil, Physica B 457 (2015) 314.

[60] P. T. Phong, L. V. Bau, L. C. Hoan, D. H. Manh, N. X. Phu, In-Ja Lee, J. Alloys Compd. 645 (2015) 243.

[61] P. T. Phong, L. V. Bau, L. C. Hoan, D. H. Manh, N. X. Phuc, In-Ja Lee, J. Alloys Compd. 656 (2016) 920.

[62] L. Garcia-Muñoz, N. Bellido, C. Frontera, J. Hernández-Velasco, C. Ritter, C. Yaicle, C. Martin, A. Maignan, J. Appl. Phys. 97 (2005) 10H701.

[63] A. Daoud-Aladin, J. Rodríguez-Carvajal, L. Pinsard-Gaudart, M. Fernandez-Diaz, A. Revcoleschi, Appl. Phys. A 71 (2002) 1758.

[64] J. Hejtmanek, K. Knızek, Z. Jirak, F. Damay, M. Hervieu, C. Martin, M. Nevriva, P. Beran, J. Appl. Phys. 93 (2003) 7370.

[65] S. K. Banerjee, Phys. Lett. 12 (1964) 16.

[66] J. Mira, J. Rivas, F. Rivadulla, C. Vazquez, M. A. Lopez-Quintela, Phys. Rev. B 60 (1999) 2998–3001.

[67] M. H. Phan, S. C. Yu, N. H. Hur, Y. H. Jeong, J. Appl. Phys. 96 (2004) 1154.

[68] The-Long Phan, Q. T. Tran, P. Q. Thanh, P. D. H. Yen, S. C. Yu, Solid State Commun. 184 (2014) 40.

[69] W. Tang, W. Lu, X. Luo, B. Wang, X. Zhu, W. Song, Z. Yang, Y. Sun, J. Magn. Magn. Mater. 322 (2010) 2360.

[70] T. Sarkar, A. K. Raychaudhuri, A. K. Bera, S. M. Yusuf, New J. Phys. 12 (2010) 123026.

[71] T. Sarkar, P. K. Mukhopadhyay, A. K. Raychaudhuri, S. Banerjee, J. Appl. Phys. 101 (2007) 124307.

[72] A. Bid, A. Guha, A. K. Raychaudhuri, Phys. Rev. B 67 (2003) 174415.

[73] J. H. Park, E. Vescovo, H. J. Kim, C. Kwon, R. Ramesh, T. Venkatesan, Phys. Rev. Lett. 81 (1998) 1953.

[74] E. Warburg, Ann. Phys. 13 (1881) 141.

[75] I. Hussain, M. S. Anwar, S. N. Khan, J. W. Kim, K. C. Chung, B. H. Koo, J. Alloys Compd. 694 (2017) 815.

[76] I. Hussain, M.S. Anwar, J.W. Kim, K.C. Chung, B. H. Koo, Ceram. Int. 42 (2016) 13098.

[77] I. Hussain, M. S. Anwar, S. N. Khan, A. S. Shahee, Z. Rehman, B. H. Koo, Ceram. Int. 43 (2017) 10080.

[78] V. K. Pecharsky, K. A. Gschneidner Jr., J. Appl. Phys. 86 (1999) 565.

[79] B. Arayedh, S. Kallel, N. Kallel, O. Peña, J. Magn. Magn. Mater. 361 (2014) 68.

[80] W. Tang, W. J. Lu, X. Luo, B. S. Wang, X. B. Zhu, W. H. Song, Z. R. Yang, Y. P. Sun, J. Magn. Magn. Mater. 322 (2010) 2360.

[81] X. X. Zhang, J. Tejada, Y. Xin, G. F. Sun, K. W. Wong, X. Bohigas, Appl. Phys. Lett. 69 (1996) 3596.

[82] T. K. Bose, R. Chahine, B. R. Gopal, M. Foldeaki, A. Barman, M. Gosh, S. K. De, S. Chatterjee, Cryogenics 38 (1998) 849.

[83] K. A. Gschneidner Jr., V. K. Pecharsky, A. O. Tsokal, Rep. Prog. Phys. 68 (2005) 1479.

[84] N. S. Bingham, M. H. Phan, H. Srikanth, M. A. Torija, C. Leighton, J. Appl. Phys. 106 (2009) 023909.

[85] P. G. Radaelli, D. E. Cox, M. Marezio, S. W. Cheong, P. E. Schiffer, A. P. Ramirez, Phys. Rev. Lett. 75 (1995) 4488.

[86] E. Dagotto, New J. Phys. 7 (2005) 67.

[87] Y. Tokura, Y. Tomioka, J. Magn. Magn. Mater. 200 (1999) 1.

[88] Y. Tomioka, A. Asamitsu, Y. Tokura, Phys. Rev. B 63 (2000) 024421.

[89] Y. Motome, N. Furukawa, Phys. Rev. B 71 (2005) 014446.

[90] M. Muroi, R. Street, P. G. McComick, J. Appl. Phys. 87 (2000) 3424.

[91] M. A. Oumezzine, O. Peña, T. Guizouarn, R. Lebullenger, M. Oumezzine, J. Magn. Magn. Mater. 324 (2012) 2821.

[92] D. H. Manh, P. T. Phong, T. D. Thanh, L. V. Hong, N. X. Phuc, Low-field magnetoresistance of $La_{0.7}Ca_{0.3}MnO_3$ perovskite synthesized by reactive milling method, J. Alloys Compd. 499 (2010) 131.

[93] J. Rivas, L. E. Hueso, A. Fondado, F. Rivadulla, M. A. Lopez-Quintela, Low field magnetoresistance effects in fine particles of La0. 67Ca0. 33MnO3 perovskites, J. Magn. Magn. Mater. 221 (2000) 57.

[94] K. Navin, R. Kurchania, Structural magnetic and transport properties of the $La_{0.7}Sr_{0.3}MnO_3$-ZnO nanocomposites, J. Magn. Magn. Mater. 448 (2018) 228.

[95] J. Khelifi, E. Dhahri, E. K. Hlil, Correlation between electrical, magnetocaloric properties and critical behavior in $(La_{0.75}Nd_{0.25})_{2/3}(Ca_{0.8}Sr_{0.2})_{1/3}MnO_3$, Solid State Comm. 249 (2017) 19.

[96] C. M. Xiong, J. R. Sun, Y. F. Chen, B. G. Shen, J. Du, Y. X. Li, Relation between magnetic entropy and resistivity in La0.67Ca0.33MnO3, IEEE Trans. Magn. 41 (2005) 122.

[97] A. J. Millis, P. B. Littlewood, B. I. Shraiman, Double exchange alone does not explain the resistivity of $La_{1-x}Sr_xMnO_3$, Phys. Rev. Lett. 74 (1995) 5144.